Magnetic and magnetodielectric properties of Eu2+-containing oxides(Dissertation_全文)

AUTHOR(S):

Zong, Yanhua

Magnetic and magnetodielectric properties of Eu^{2+}-containing oxides

Yanhua Zong

2010

Contents

General Introduction

Magnetic materials have been key components in various industrial applications such as information and transportation technologies, sensors, and so on. The development of magnetic materials has led to the explosive growth in the areal density (bit/in^2) of magnetic recording media almost by two orders every year. Unfortunately, however, the conventional magnetic information storage technology is approaching the perceived superparamagnetic limit which does not allow a further reduction of the size of a bit, correspondingly increasing the areal density of hard drives. To meet the desire for mass storage and miniaturization of devices, considerable attention has been paid to spintronics (or spin electronics, magnetoelectronics) which exploit both the spin and charge of an electron and/or a positive hole. The research on spintronics has been focused on ferromagnetic metals and semiconductors in the last few years [1]. One great achievement is the discovery of giant magneto resistance (GMR) in multilayers of iron and chromium in late 1980s [2,3]. The GMR spin-valve head has enabled hard-disk drives to read smaller data bits and led to an increase of more than 40 orders in areal density since it became commercially viable in 1997. One can expect that with the development of spintronics it is possible to store a bit of data on a single atom.

Magnetic insulators which combine magnetism with insulating properties are attractive candidcates in spintronic devices as well. Strong insulation is a prerequisite for electronic polarity which can not be realized in conductors. Also, magnetic insulators are desired for the high-frequency applications since magnetic conductors can not be used at high frequencies due to the eddy current losses. In the last few decades, Eu^{2+}-containing insulating compounds have attracted much attention due to their

fascinating magnetic and electronic properties since the discovery of ferromagnetic transition in EuO in 1961 [4-7]. It was reported that EuO could be used as a ferromagnetic insulator to induce ferromagnetic properties in graphene by the proximity effect [8] and to control the spin polarization of current by a gate voltage [9]. Moreover, a strong coupling between magnetic and dielectric properties has been discovered in $EuTiO_3$ although this material is not ferroelectric. This finding shed a new light to the nature of magnetoelectric coupling [10]. However, when compared to magnetic materials containing transition-metal ions, the mechanism of magnetic interactions and phase transition in Eu^{2+}-containing compounds has been less understood. Therefore, from viewpoints of both theoretical research and practical applications, it is of significance to further investigate the existing Eu^{2+}-containing compounds and develop new devices.

Compared to crystalline materials, amorphous ones have advantages such as easy fabrication at low cost, and so on. Since Gubanov predicted that ferromagnetism can exist even in amorphous materials [11], extensive studies have been carried out to search for amorphous magnets, leading to the discovery of numerous ferromagnetic amorphous alloys [12-15]. The ferromagnetic amorphous alloys, known as soft ferromagnets, have been applied to various devices such as power electrical devices, inductive components used in electrics, magnetic heads, magnetic shields, sensors, transducers, and so on. However, ferromagnetism has been rarely found in amorphous insulators. In 1975, Litterst reported a ferromagnetic transition in amorphous FeF_2 with a Weiss temperature (θ) of 21 K in contrast to the crystalline FeF_2 that is an antiferromagnet with $\theta = -117$ K [16]. The ferromagnetic ordering was explained in terms of superparamagnetism of ultra-fine ferromagnetic particles with ferromagnetic

superexchange interactions of 90° Fe^{2+}-F^--Fe^{2+} bonds. Similar phenomena have been subsequently observed in amorphous $FeCl_2$ and $FeBr_2$ [17,18]. However, there is no further evidence for the presence of 90° ferromagnetic interactions. Since most amorphous insulators containing Fe^{2+} ions prefer antiferromagnetic rather than ferromagnetic interactions [19,20], the observed ferromagnetic transitions are probably not intrinsic in such amorphous systems. Ota *et al*. reported in 1986 that the mixture of antiferromagnetic oxides, $BiFeO_3$ and $ZnFeO_4$, leads to ferromagnetic amorphous phase [21]. Since then, amorphous oxides based on amorphous ferrites have been widely studied [22-26]. Unfortunately, subsequent studies using high-resolution transmission electron microscope (HRTEM) observation and Mössbauer measurements revealed that the ferromagnetic behavior in such systems arises from ferrimagnetic nanocrystalline phases embedded in the amorphous matrixes [27,28]. In contrast to the previous controversial reports on amorphous ferromagnetic insulators, recently Akamatsu *et al*. reported a clear ferromagnetic transition in a Eu^{2+}-containing oxide glass with Eu^{2+} concentration of 45% in cation ratio [29]. The structure of the glass was confirmed to be amorphous from HRTEM measurement. The ferromagnetic transition of the glass was attributed to the predominance of ferromagnetic interactions, different from most of the amorphous insulators. This result makes it attractive and necessary to further investigate amorphous Eu^{2+}-containing systems.

Due to captivating features of Eu^{2+}-containing compounds, in this work I have systematically investigated magnetic properties of amorphous europium titanate and europium zirconate thin films as well as magnetic and dielectric properties of bulk polycrystalline $EuZrO_3$. This thesis is composed of the following parts:

Chapter 1 briefly describes the theoretical background of magnetism for Eu^{2+}-containing compounds and reviews the research progress in related studies. Since the magnetic properties of a system, especially an amorphous system, are mainly determined by the interactions between the magnetic ions, the description on theoretical background primarily involves the mechanism of various magnetic interactions concerning Eu^{2+} ions. The review is focused on magnetic properties of europium chalcogenides and europium titanate [30].

Chapter 2 introduces the preparation, structural and magnetic properties of amorphous europium titanate thin films with nominal compositions of mEuO-TiO_2 (m=1, 2, 4) [31,32]. The measurements of ^{151}Eu conversion electron Mössbauer (CEM) and extended X-ray absorption fine structure (EXAFS) spectra indicate that the local structures of Eu^{2+} ions in amorphous EuO-TiO_2 and 2EuO-TiO_2 thin films are similar to that in EuO and the coordination number of Eu^{2+} and Eu-O bond length decrease with an increase of m. All the thin films demonstrate predominant ferromagnetic interactions as implied by the positive Weiss temperatures, and undergo a reentrant spin glass transition after a ferromagnetic transition as the temperature is decreased. The mechanism of magnetic interactions and phase transition has been discussed in terms of their structures.

Chapter 3 describes the structural and magnetic properties of bulk polycrystalline $EuZrO_3$ and amorphous europium zirconate thin films with nominal compositions of mEuO-ZrO_2 (m=1, 4) [33,34]. The crystal structure of $EuZrO_3$ has been refined to be an orthorhombic perovskite by Rietveld analysis of X-ray diffraction (XRD) pattern. An antiferromagnetic transition has been observed for the first time in $EuZrO_3$ below the Néel temperature (T_N) of 4.1 K with a positive Weiss temperature of 0.07 K. The

amorphous europium zirconate thin films exhibit ferromagnetic and reentrant spin-glass transitions with ferromagnetic transition temperatures slightly higher than those of amorphous europium titanate thin films.

Chapter 4 introduces results on magnetodielectric properties of bulk polycrystalline $EuZrO_3$ [35]. No quantum paraelectric transition has been observed in $EuZrO_3$ in the whole temperature region. At low temperatures $EuZrO_3$ shows a magnetodielectric coupling similar to that in $EuTiO_3$, and the coupling constant has been evaluated based on mean-field calculations. The magnitude of the coupling constant in $EuZrO_3$ is much smaller than that in $EuTiO_3$ due to the difference in the covalency between the Zr-O and Ti-O bonds.

The final part is devoted to the summary of the present thesis.

References

1. I. Žutić, J. Fabian, and S. D. Sarma, *Rev. Mod. Phys.* **76**, 323 (2004).
2. G. Binasch, P. Grünberg, F. Saurenbach, and W. Zinn, *Phys. Rev. B* **39**, 4828 (1989).
3. M. N. Baibich, J. M. Broto, A. Fert, F. Nguyen van Dau, F. Petroff, P. Eitenne, G. Creuzet, A. Friederich, and J. Chazelas, *Phys. Rev. Lett.* **61**, 2472 (1988).
4. B. T. Matthias and R. M. Bozorth, *Phys. Rev. Lett.* **7,** 160 (1961).
5. L. Passell, O. W. Dietrich, and J. Als-Nielsen, *Phys. Rev. B* **14**, 4897 (1976).
6. Chia-Ling Chien, S. DeBenedetti, and F. De Barros, *Phys. Rev. B* **10**, 3913 (1974).
7. J. E. Greedan, C. L. Chien, and R. G. Johnston, *J. Solid State Chem.* **19**, 155 (1976).
8. H. Haugen, D. Huertas-Hernando, and A. Brataas, *Phys. Rev. B* **77**, 115406 (2008).
9. T. Yokoyama, *Phys. Rev. B* **77**, 073413 (2008).
10. T. Katsufuji and H. Takagi, *Phys. Rev. B* **64**, 054415 (2001).
11. A. J. Gubanov, *Sov. Phys.-Solid State* **2**, 468 (1960).
12. T. Mizoguchi, N. Ueda, K. Yamauchi, and H. Miyajima, *J. Phys. Soc. Jpn.* **34**, 1691 (1973).
13. K. Yamada, Y. Ishikawa, Y. Endoh, and T. Masumoto, *Solid State Commun*. **16**, 1335 (1975).
14. L. J. Schowalter, M. B. Salamon, C. C. Tsuei, and R. A. Craven, *Solid State Commun*. **24**, 525 (1977).
15. X. Ze, Y. Ishikawa, S. Ishiot, and M. Takahashit, *J. Phys. F: Met. Phys.* **15**, 1787 (1985).
16. F. J. Litterst, *J. Physique* **36**, L 197 (1975).

17. A. J. F. Boyle, G. M. Kalvius, D. M. Gruen, J. R. Clifton, and R. L. McBeth, *J. Physique* **32**, C1 224 (1971).
18. F. J. Litterst, G. M. Kalvius, and A. J. F. Boyle, *A. I. P. Conference Proceedings* **18**, 616 (1974).
19. H. Akamatsu, K. Fujita, S. Murai, and K. Tanaka, *Appl. Phys. Lett.* **92**, 251908 (2008).
20. J. P. Sanchez, J. M. Friedt, R. Horne, and A. J. van Duyneveldt, *J. Phys. C: Solid State Phys.* **17**, 127 (1984).
21. N. Ota, M. Okubo, S. Masuda, and K. Suzuki, *J. Magn. Magn. Mater.* **54-57**, 293 (1986).
22. K. Suzuki, H. Onodera, M. Sakurai, S. Masuda, A. Matsumoto, and H. Sadamura, *IEEE Trans. Magn.* **MAG-22**, 1090 (1986).
23. S. Nakamura and N. Ichinose, *J. Non-Cryst. Solids* **95-96**, 849 (1987).
24. T. Fujii, S. Jmzenji, Y. Asahara, A. Kajima, and T. Shinjo, *J. Appl. Phys*. **64**, 5434 (1988).
25. S. Soeya, S. Nakamura, and N. Ichinose, *J. Appl. Phys.* **68**, 2875 (1990).
26. G. Srinivasan, B. Uma Maheshwar Rao, J. Zhao, and M. S. Seehra, *Appl. Phys. Lett*. **59**, 372 (1991).
27. S. Nakamura and N. Ichinose, *Jpn. I. Appl. Phys*. **28**, 984 (1989).
28. S. Nakamura, Y. Hiratsu, and N. Ichinose, *Jpn. J. Appl. Phys.* **30**, L844 (1991).
29. H. Akamatsu, K. Fujita, S. Murai, and K. Tanaka, *Phys. Rev. B* **81**, 014423 (2010).
30. K. Fujita, N. Wakasugi, S. Murai, Y. Zong, and K. Tanaka *Appl. Phys. Lett.* **94**, 062512 (2009).

31. Y. Zong, K. Fujita, H. Akamatsu, S. Murai, and K. Tanaka, *J. Non-Cryst. Solids* in press (2010).
32. H. Akamatsu, K. Fujita, Y. Zong, S. Murai, and K. Tanaka, *Phys. Rev. B* submitted (2010).
33. Y. Zong, K. Fujita, H. Akamatsu, S. Murai, and K. Tanaka, *J. Solid State Chem*. **183**, 168 (2010).
34. Y. Zong, K. Fujita, H. Akamatsu, S. Murai, and K. Tanaka, *Phys. Stat. Sol. (c)* in press (2010).
35. T. Kolodiazhnyi, K. Fujita, L. Wang, Y. Zong, K. Tanaka, Y. Sakka, and E. Takayama-Muromachi, *Appl. Phys. Lett*. **96**, 252901 (2010).

Chapter 1 Magnetic properties of Eu^{2+}-containing compounds

Since the discovery of ferromagnetism in EuO in 1961 [1], much attention has been paid to Eu^{2+}-containing compounds, followed with rapid development of new magnetic materials and understandings of their magnetic behaviors [2-5]. In this chapter, the theoretical background on the magnetism of Eu^{2+}-containing compounds will be described briefly, and then a few important examples will be separately presented.

1.1 Theoretical background

1.1.1 Magnetic couplings

In magnetic materials, the magnetic moments are coupled with one another through exchange interactions. The magnetic exchange interactions are quantum mechanical in nature and usually written in the form of a spin Hamiltonian as $H_{ij} = -J_{ij}S_i \cdot S_j$, where J_{ij} is the exchange constant, S_i and S_j are the magnetic moments at lattice sites *i* and *j*. There are three types of exchange interactions which are currently believed to exist: (I) direct exchange, (II) indirect exchange, and (III) superexchange interactions.

(I) Direct exchange

Direct exchange exists between magnetic moments which are close enough to have sufficient overlap of their wave functions. The direct exchange is expected to originate from the overlap of the electronic wave functions and the Coulomb electrostatic repulsion. According to Pauli Exclusion Principle, the electrons with parallel spins

will stay away from each other in order to reduce the Coulomb repulsion. Therefore the direct exchange usually favors an antiparallel configuration of the spin. Since the wave functions of the magnetic *d* or *f* electrons decay exponentially with distance from the nucleus, the direct exchange can only act in a short range and will decrease rapidly as the ions are separated.

(II) Indirect exchange

When magnetic ions are separated over relatively large distances with little direct overlap between neighboring magnetic *d* or *f* electrons, the magnetic exchange interaction will operate through an intermediary. In metals, this type of exchange is well known as the RKKY interaction named after Ruderman, Kittel, Kasuya and Yoshida and the intermediary are the conduction electrons (itinerant electrons) [6-8]. A magnetic ion induces a spin polarization in the conduction electrons in its neighborhood. This spin polarization in the itinerant electrons is felt by the moments of other magnetic ions within the range, leading to an indirect coupling. Since the RKKY exchange coefficient (J) oscillates from positive to negative as the separation of the ion changes and has a damped oscillatory nature, the magnetic coupling resulting from the RKKY exchange can be either ferromagnetic or antiferromagnetic, depending on the separation distance between a pair of magnetic ions.

Indirect exchange can also exist in insulting magnetic materials. For example, in materials containing rare-earth ions, since the 4*f* magnetic electrons of rare-earth ions are well shielded by the 5*s* and 5*p* electrons, the direct exchange between 4*f* electrons is expected to be very weak. Instead, it has been suggested that an indirect exchange takes place through the overlap of the partially filled 5*d* states [9]. This process can be viewed as a 4*f* electron is excited to the 5*d* band, experiences an exchange interaction

with the 4*f* spin on a nearest neighbor and returns to the initial state. Such an indirect exchange interaction generally leads to a ferromagnetic coupling of the magnetic moments.

(III) Superexchange

Superexchange is the primary magnetic mechanism in magnetic insulators. It works between magnetic moments on ions separated too far to be connected via direct exchange, but coupled over a relatively long distance through a ligand or an anion. Superexchange interaction was first proposed by Kramers [10] and then formulated by Anderson [11]. Later the Kramers-Anderson (KA) mechanism was evolved by Kanamori [12] and Goodenough [13] in order to apply to various transition metal oxides. According to their results, the superexchange interactions depend on the sorts of transition metal ions and metal-oxygen-metal bond angles. For most transition metal oxides, the superexchange interactions can be changed from strong antiferromagnetic to weak ferromagnetic ones when the cation–anion–cation angle is varied from 180° to 90°. Figure 1.1 illustrates the superexchange between two Fe^{3+} ions via an intermediate O^{2-} ion. The O^{2-} ion transfers a 2*p* electron to the neighboring Fe^{3+} ion. Due to the covalent mixing of the *p* and *d* wave functions, the 3*d* spin on Fe^{3+} ions is aligned parallel to the 2*p* spin, and since the two 2*p* spins must be opposite in direction according to Pauli Exclusion Principle, the 3*d* spins on the two Fe^{3+} ions are paired in antiparallel direction. This causes an antiferromagnetic coupling between the two Fe^{3+} ions.

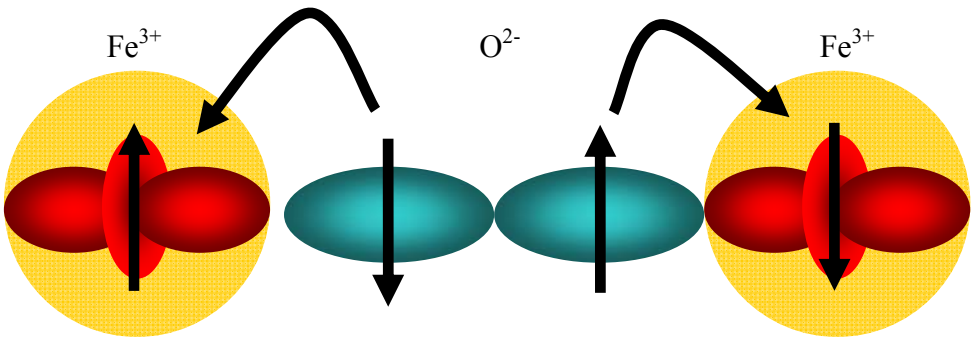

Fig. 1.1: A scheme for superexchange interactions between two Fe^{3+} ions via an intermediate O^{2-} ion.

1.1.2 Magnetic mechanism in Eu^{2+}-containing compounds

Eu^{2+} ion has a $4f^7$ electronic configuration ($1s^2\ 2s^2p^6\ 3s^2p^6d^{10}\ 4s^2p^6d^{10}f^7\ 5s^2p^6$) with a spherically symmetric ${}^8S_{7/2}$ state. Since the 4*f* electrons are shielded by 5*s* and 5*p* closed shells, direct exchange is expected to contribute very weakly to the magnetic orderings in Eu^{2+}-containing compounds. Therefore the coupling of spins on Eu^{2+} ions is through indirect exchange and/or superexchange interactions. Below is a brief description of these two mechanisms in Eu^{2+}-containing compounds.

(I) Indirect exchange

Insulators and some of semiconductors containing Eu^{2+} ions are nearly ideal examples of Heisenberg magnets where the magnetism is determined by the exchange interactions between nearest-neighboring (NN) and next-nearest-neighboring (NNN) Eu^{2+} ions. Europium titanate ($EuTiO_3$) is a typical example for Eu^{2+}-containing insulators, while europium chalcogenides (EuX: X=O, S, Se, and Te) for Eu^{2+}-containing semiconductors. The overlap of the 5*d* states makes possible an indirect mechanism between 4*f* spins on NN Eu^{2+} ions through 5*d* bands. The exchange constant is given by [14]

$$J \sim J^{intra} b^2/U^2, \tag{1.1}$$

where J^{intra} is the intra-atomic exchange parameter between the 4*f* and 5*d* states of Eu^{2+} ions which is almost unchanged for different Eu^{2+}-containing compounds, *b* is the transfer integral between NN Eu^{2+} ions and dependent on the distance of separation, and *U* is the energy separation between the 4*f* and 5*d* states of Eu^{2+} ions. Therefore, the magnitude of *J* varies with the NN Eu^{2+} distance and the 4*f*-5*d* energy difference.

In Eu^{2+}-containing metals or semiconductors like carrier-doped EuX, the dominant

indirect exchange is RKKY exchange through conduction electrons populated in the 5*d* orbitals. Similar to the RKKY exchange in other systems, the exchange constant is a function of the distance (R) between two Eu^{2+} ions, which is given by [6-8]

$$J \sim \frac{\cos(2k_F R)}{(k_F R)^3}, \tag{1.2}$$

where k_F is the Fermi wave function and depends on the number of free conduction electrons per magnetic ion (n), $k_F \sim (n)^{1/3}$ [15]. However, for a Eu^{2+}-containing semiconductor with a very small n so that the conduction electrons can be viewed as partially localized, the RKKY exchange will be rather different from that described in Eq. (1.2). In such case, the overlap of the 5*d* orbitals on the NN Eu^{2+} is necessary for the conduction electrons to produce a magnetic exchange interaction [15].

(II) Superexchange

The superexchange through an anion in Eu^{2+}-containing compounds is suggested to be much more complicated than that in transition metal oxides due to the special electronic structure of Eu^{2+}. Kasuya proposed three competing mechanisms of superexchange in europium chacogenides and estimated the magnitude of these interactions with 180° cation-anion-cation configuration [16]:

(i) The Kramers-Anderson superexchange (J_{KA}).

Similar to the superexchange in transition metal oxides, the 4*f* electrons on Eu^{2+} ions are coupled through the 2*p* state of anions. This exchange is antiferromagnetic and is very weak due to the small overlap between 2*p* and 4*f* states as shown in Fig. 1.2. The magnitude of J_{KA} was evaluated to be 0.5×10^{-6} and 0.6×10^{-6} eV for EuO and EuSe, respectively.

(ii) Superexchange via the *d*–*f* exchange interaction (J_{df}).

The 2*p* electrons of anions are transferred to the 5*d* orbitals of NN Eu^{2+} ions and then affect the 4*f* spins via the *d*–*f* exchange interaction. The value of J_{df} in EuSe was estimated to be -1.6×10^{-5} eV, well consistent with the experimental value of the exchange constant between NNN Eu^{2+} ions. Therefore, this mechanism was suggested to be responsible for the antiferromagnetic coupling between NNN Eu^{2+} ions in EuS, EuSe, and EuTe.

(iii) A mix of J_{KA} and J_{df} (J_c).

The Eu^{2+} 5*d* and anion 2*p* orbitals form bonding and antibonding molecular orbitals via hybridization. An oxygen electron is excited from the bonding to the antibonding 5*d*-2*p* molecular orbital, which has exchange interaction with both Eu spins, its place is taken by a Eu 4*f* electron, after which the 5*d* electron fills the 4*f* hole. The sign of J_c is expected to be opposite to that of J_{df}, and this mechanism could explain the positive exchange constants between NNN Eu^{2+} ions in EuO and $EuTiO_3$.

Although Kasuya only considered 180° cation-anion-cation configuration in his calculation, these mechanisms should also be applicable to the cation-anion-cation configurations with other angles. However, theoretical evaluation of the superexchange intensities with such configurations has not been carried out until now. It was only suggested, from the experimental results, that the superexchange interactions between Eu^{2+} with 90° cation-anion-cation configuration are negative [3,9].

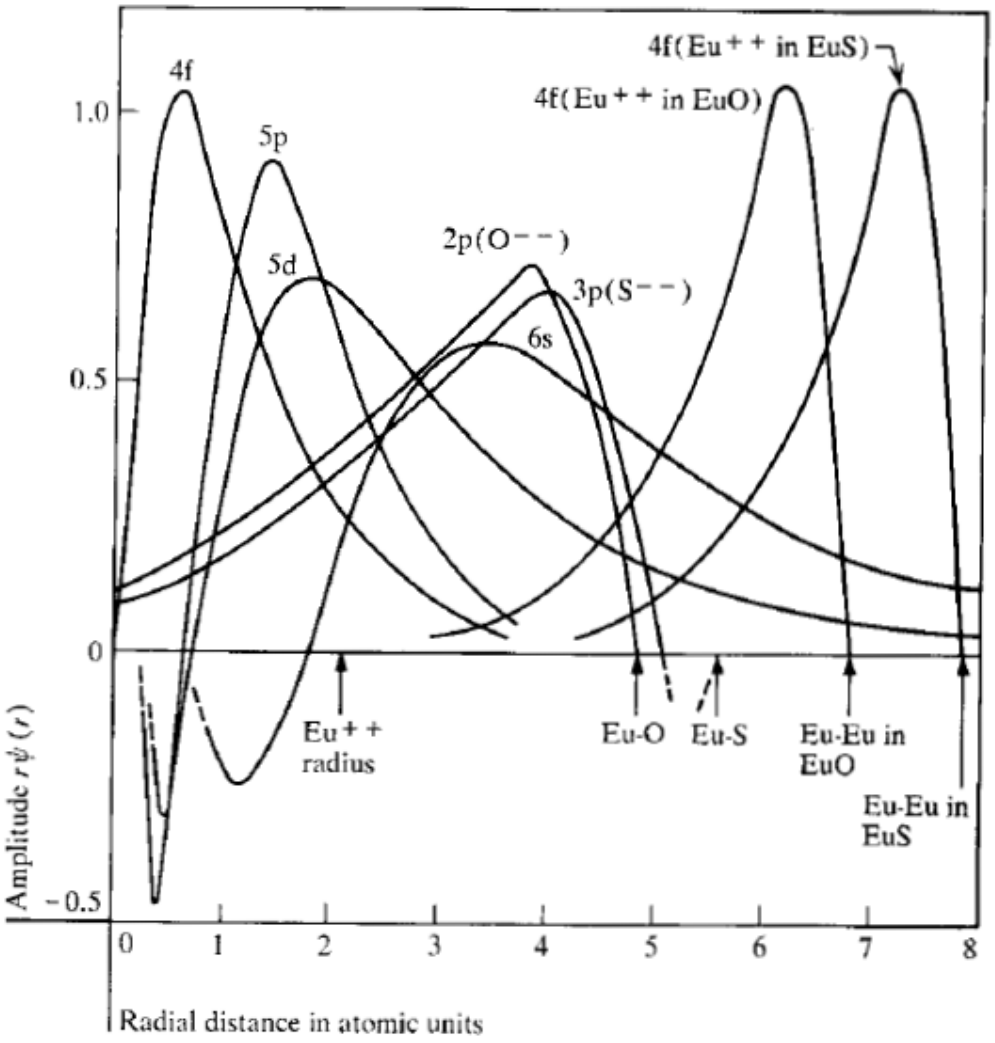

Fig. 1.2: The overlap of cation-cation and anion-cation wave functions in EuO and EuS [16]. The arrows indicate the lattice distance between NN Eu and chalcogen ions.

1.2 Eu^{2+}-containing compounds

Eu^{2+}-containing compounds have been widely studied for their intriguing magnetic and electrical properties, among which most attention has been paid to EuX and europium titanates. For instance, EuO is a well-known ferromagnet with tunable conductivity by doping it with oxygen vacancies or rare-earth ions [15,17,18], which makes it a potential material for spin injection. $EuTiO_3$ exhibits antiferromagnetic behavior with strong magnetodieletric coupling [19,20], while Eu_2TiO_4 and $Eu_3Ti_2O_7$ are ferromagnets with ferromagnetic transition temperature around 8 K [20]. Below is an individual introduction to the previous studies of EuX and $EuTiO_3$, respectively.

1.2.1 EuX

The research on EuX can be traced back to 1960s and recently the interest has been renewed for their potential application in spintronic devices. EuX have NaCl-type crystal structure with lattice parameters of 5.14 (EuO), 5.96 (EuS), 6.20 (EuSe) and 6.60 Å (EuTe). They are intrinsic magnetic semiconductors, which is very rare for rare-earth compounds. The band gaps of EuO, EuS, EuSe, and EuTe at room temperature are 1.12, 1.65, 1.80, and 2.0 eV, respectively. As ideal Heisenberg magnets, their magnetic properties are mainly determined by the exchange interactions between NN and NNN Eu^{2+} ions. The exchange interactions between NN Eu^{2+} ions are dominated by indirect interactions while those between NNN Eu^{2+} ions are dominated by 180° Eu-O-Eu superexchange interactions as mentioned above.

Figure 1.3 plots the exchange constants between NN and NNN Eu^{2+} ions (J_1 and J_2, respectively) and the Weiss temperature θ as a function of the lattice constant of EuX.

From oxide to telluride the positive value of J_1 decreases sharply while the value of J_2 first changes from positive to negative and then becomes stronger in magnitude. For EuO both J_1 and J_2 are positive, resulting in ferromagnetic transition with Curie temperature T_C=69 K [21]. The value of J_2 becomes negative for EuS but the magnitude is lesser than J_1, leading to a ferromagnetic phase with T_C=16 K [21]. Due to the competitive values of J_1 and J_2, the magnetic phase diagram of EuSe is a little complicated. It is a metamagnet with an antiferromagnetic transition temperature T_N=4.6 K and changes into a ferrimagnetic phase below 2.8 K with a mixed phase of MnO-type antiferromagnetic and ferrimagnetic ordering. Below T_N=1.8 K it again enters in antiferromagnetic phase with MnO-type antiferromagnetic ordering [22]. The relatively larger negative magnitude of J_2 leads to antiferromagnetic transition with T_N=10 K in EuTe.

Although the ferromagnetic transition temperature T_C is low in bulk EuX, a lattice contraction induced by pressure [24-27], chemical doping [17,23,28,29] or interfacial strain [30-32], which increases the hybridization between Eu^{2+} 4*f* and 5*d* states, significantly increases T_C. For instance, the increase of T_C up to 140 K was observed in Eu-riched EuO films [28] and EuO bulk doped with Gd or Ho [17,29]. The value of T_C in EuO can reach 200 K with a hydrostatic pressure of about 10 GPa [27]. Ingle *et al.* made first-principles calculations on EuO thin films and suggested that a 5.5% biaxially compressed strain would allow an increase of T_C up to 175 K [32]. A room temperature of T_C (290 K) was demonstrated in EuS with a pressure of 88 G Pa [26]. These results together with the successful reports on EuO integration with Si and GaN [30], keep up the promise for the usage of EuX in spin-electronics.

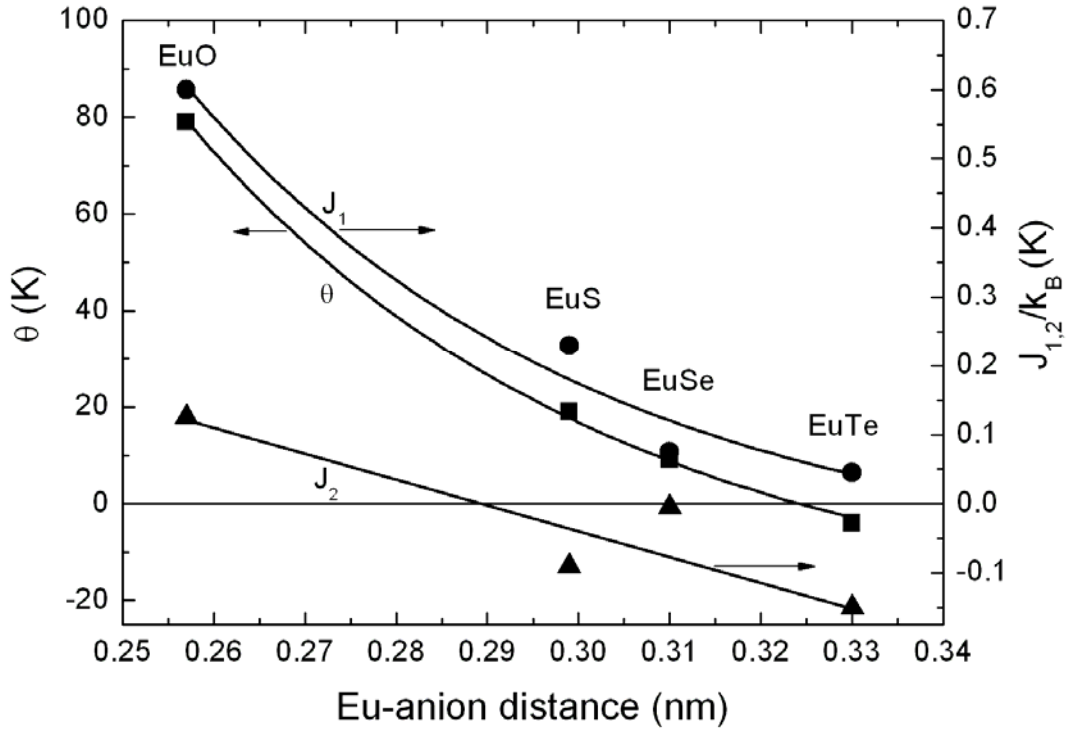

Fig. 1.3: Weiss temperature θ (triangles) and NN and NNN exchange parameters J_1 (squares) and J_2 (circles) versus the lattice constant for different EuX. Data were collected by Wachter [23].

1.2.2 $EuTiO_3$

$EuTiO_3$ has a cubic perovskite structure with Eu^{2+} ions on the dodecahedral sites and Ti^{4+} ions on the tetragonal sites, as indicated in Fig. 1.4(a). Stoichiometric $EuTiO_3$ is an antiferromagnetic insulator with T_N=5.5 K [20], and exhibits quantum paraelectric properties with strong magnetodielectric coupling (coupling constant between spin correlation and dielectric constants α=2.74×10^{-3}) at low temperatures (see Fig. 1.4(c)) [19]. The magnetic structure of $EuTiO_3$ is *G*-type antiferromagnetic with NN Eu^{2+} ions coupling with each other antiferromagnetically and NNN Eu^{2+} ions coupling with each other ferromagnetically, as illustrated in Fig. 1.4(b).

It was suggested that NN Eu^{2+} ions couple through indirect exchange and 90° Eu-O-Eu superexchange while NNN Eu^{2+} ions couple through 180° Eu-O-Eu superexchange [3,9]. The exchange constants estimated under the molecular-field theory are J_1/k=-0.014 and J_2/k=+0.037 K, respectively [20]. The much smaller value of J_1 compared to that in EuO was ascribed to the small crystal-field splitting of 5*d* state in $EuTiO_3$ which results in a weak indirect exchange. As suggested by Chien *et al.* [20], the 4*f*-5*d* energy difference averaged over 5*d* sublevels can be assumed to be the same for different compounds (U_0≈3.5 eV), therefore the value of *U* in Eq. (1.1) can be viewed as a sum of U_0 and the crystal-field splitting of 5*d* levels (10*Dq* for cubic crystal-field splitting). For $EuTiO_3$, *U* can be written as

$$U = U_0 - \frac{3}{5}(10Dq). \tag{1.3}$$

According to a theoretical calculation by Chien *et al.* [20], the value of 10 *Dq* in $EuTiO_3$ is one order smaller than that in EuO, which then explains the smaller J_1 in $EuTiO_3$. In addition, the number of antiferromagnetic 90° superexchange interactions in $EuTiO_3$ for

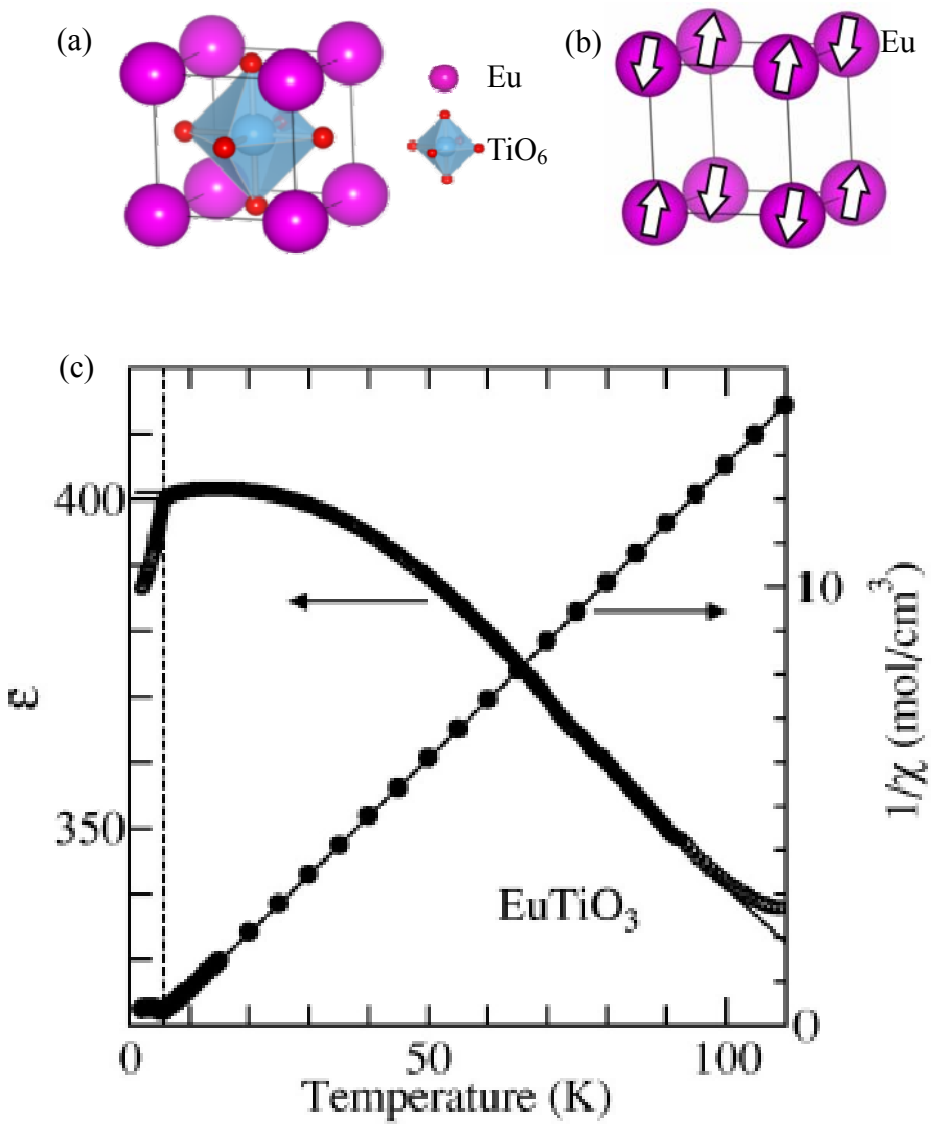

Fig. 1.4: (a) and (b) Crystal and magnetic structure of $EuTiO_3$; (c) Temperature dependence of dielectric constants at 100 kHz (left axis) and inverse magnetic susceptibility (right axis) for $EuTiO_3$ [19].

a pair of NN Eu^{2+} ions is doubled over that in EuO due to the increase of Eu^{2+} coordination number, which results in a negative value of J_1 [3,9].

Due to the significantly larger magnitude of J_2 compared to that of J_1, $EuTiO_3$ is one of the few antiferromagnets with ferromagnetic molecular field as revealed by the positive value of θ (+3.8 K) [20]. Thus, the magnetic structure of $EuTiO_3$ can be viewed as follows: two face centered cubic sublattices, where Eu^{2+} spins order ferromagnetically with the relatively strong interactions, are weakly coupled with each other in an antiferromagnetic way, resulting in the *G*-type antiferromagnetic ordering whose magnetic energy is slightly different from that of the ferromagnetic ordering. In such a situation, a small perturbation could lead to a big change of the magnetic structure. A first-principles calculation by Ranjan *et al.* [33] demonstrated that the ground state magnetic structure of bulk $EuTiO_3$ changes from *G*-type antiferromagnetic to ferromagnetic with an increase in the lattice volume. A similar calculation on $EuTiO_3$ thin film by Fennie *et al.* [34] indicates that the *G*-type antiferromagnetic phase is stable in the absence of the strain but the ferromagnetic phase becomes more stable when the strain exceeds 1.2% as shown in Fig. 1.5. Recently our experimental results on epitaxial $EuTiO_3$ thin films show that thin films with 2.4% out-of-plane elongation exhibit ferromagnetic behaviors [35], which is coincident with the theoretical calculations. In addition, the transition from the *G*-type antiferromagnetic phase to ferromagnetic phase can be realized via carrier doping in $EuTiO_3$. For instance, it has been reported that a partial substitution of trivalent rare-earth ions (e.g. La^{3+}, Gd^{3+}) for Eu^{2+} ions results in the occurrence of ferromagnetic metals, which is suggested to arise from the carrier-mediated RKKY interaction [36].

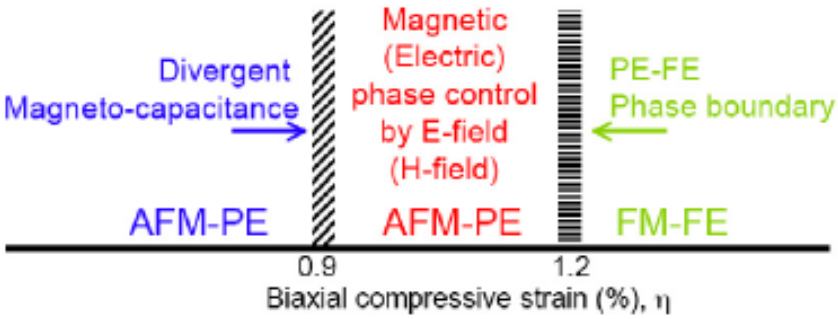

Fig. 1.5: Compressive epitaxial strain (η) phase diagram of $EuTiO_3$ thin film [34]. AFM: antiferromagnetic; FM: ferromagnetic; PE: paraelectric; FE: ferroelectric.

References

1. B. T. Matthias, R. M. Bozorth, and J. H. Van Vleck, *Phys. Rev. Lett.* **7**, 160 (1961).
2. H. Shafer, *J. Appl. Phys.* **36**, 1145 (1965).
3. J. E. Greedan and G. J. McCarthy, *Mat. Res. Bull.* **7**, 531 (1972).
4. V. G. Zubkov, A. P. Tyutyunnik, V. A. Pereliaev, G. P. Shveikin, J. Köhler, R. K. Kremer, A. Simon, and G. Svensson, *J. Alloys Compd.* **226**, 24 (1995).
5. G. K. Strukova, D. V. Shovkun, V. N. Zverev, I. E. Batov, S. A. Zver'kov, and S. S. Khasanov, *Physica C* **351**, 363 (2001).
6. M.A. Ruderman and C. Kittel, *Phys. Rev.* **96**, 99 (1954).
7. T. Kasuya, *Prog. Theor. Phys.* **16**, 45 (1956).
8. K. Yoshida, *Phys. Rev.* **106**, 893 (1957).
9. T. R. McGuire, M. W. Shafer, R. J. Joenk, H. A. Alperin, and S. J. Pickart, J. Appl. Phys. **37**, 981 (1966).
10. H. A. Kramers, *Physica* **1**, 182 (1934).
11. P. W. Anderson, Phys. Rev. **79**, 350 (1950).
12. J. Kanamori, J. Phys. Chem. Solids **10**, 87 (1959).
13. J. B. Goodenough, Phys. Rev. **100**, 564 (1955).
14. J. B. Goodenough, *Magnetism and the Chemical Bond* (Interscience, New York, 1963).
15. F. Holtzberg, T. R. McGuire, S. Methfessel, and J. C. Suits, *Phys. Rev. Lett.* **13**, 18 (1964).
16. T. Kasuya, *IBM J. Res. Dev.* **14**, 214 (1970).
17. A. Mauger, M. Escorne, C. Godart, J. P. Desfours, and J. C. Achard, *J. Phys. Colloq*.

(Paris) **41**, C5-263 (1980).

18. Y. Shapira, S. Foner, and T. B. Reed, *Phys. Rev. B* **8**, 2299 (1973).
19. T. Katsufuji and H. Takagi, *Phys. Rev. B* **64**, 054415 (2001).
20. C. L. Chien, S. DeBenedetti, and F. De Barros, *Phys. Rev. B* **10**, 3913 (1974).
21. L. Passell, O. W. Dietrich, and J. Als-Nielsen *Phys. Rev.* B **14**, 4897 (1976).
22. R. Griessen, M. Landolt, and H. R. Ott, *Solid State Commun*. **9**, 2219 (1971).
23. P. Wachter, *Handbook on the Physics and Chemistry of Rare Earths* (North-Holland, Amsterdam, 1979), Vol. 2, p. 507.
24. I. N. Goncharenko and I. Mirebeau, *Phys. Rev. Lett.* **80**, 1082 (1998).
25. J. Kunes, W. Ku, and W. E. Pickett, *J. Phys. Soc. Jpn.* **74**, 1408 (2005).
26. K. Rupprecht, Ph.D. thesis, Universität Paderborn, (2004).
27. D. DiMarzio, M. Croft, N. Sakai, and M. W. Shafer, *Phys. Rev. B* **35**, 8891 (1987).
28. O. Massenet, Y. Capiomont, and N. V. Dang, *J. Appl. Phys*. **45**, 3593 (1974).
29. H. Ott, S. J. Heise, R. Sutarto, Z. Hu, C. F. Chang, H. H. Hsieh, H.-J. Lin, C. T. Chen, and L. H. Tjeng, *Phys. Rev. B* **73**, 094407 (2006).
30. A. Schmehl, V. Vaithyanathan, A. Herrnberger, S. Thiel, C. Richter, M. Liberati, T. Heeg, M. Rockerath, L. Kourkoutis, S. Muhlbauer *et al.*, *Nature Mater.* **6**, 882 (2007).
31. R. T. Lechner, G. Springholz, T. U. Schülli, J. Stangl, T. Schwarzl, and G. Bauer, *Phys. Rev. Lett*. **94**, 157201 (2005).
32. N. J. C. Ingle and I. S. Elfimov, *Phys. Rev. B* **77**, 121202 (R) (2008).
33. R. Ranjan, H. S. Nabi, and R. Pentcheva, *J. Phys. C*: *Condensed Matter* **19**, 406217(2007)
34. C. J. Fennie and K. M. Rabe, *Phys. Rev. Lett*. **97**, 267602 (2006).

35. K. Fujita, N. Wakasugi, S. Murai, Y. Zong, and K. Tanaka, *Appl. Phys. Lett.* **94**, 062512 (2009).

36. T. Katsufuji and Y. Tokura, *Phys. Rev. B* **60**, R15021 (1999).

Chapter 2 Structural and magnetic properties of amorphous europium titanate thin films

2.1 Introduction

Amorphous ferromagnets are attractive because they combine the advantages of ferromagnets and amorphous materials. Most amorphous ferromagnets discovered to date are ferromagnetic amorphous alloys where the magnetic atoms are coupled with each other through RKKY interactions [1-4]. However, ferromagnetism has been rarely found in amorphous insulators where short range superexchange interactions are dominant. In most insulating oxide and fluoride glasses, antiferromagnetic superexchange interactions via anions are dominant, as demonstrated by the negative values of θ [5-7]. The random distribution of magnetic ions, as well as the prevailing antiferromagnetic interactions among magnetic ions, causes geometrical frustration in the alignment of magnetic moments at low temperatures, eventually leading to the spin glass transition. One of the exceptions is the Eu^{2+}-containing glasses. In 1979, Shoenes *et al*. [8] reported that a europium silicate glass with a composition of $Eu_{0.14}Si_{0.31}O_{0.55}$, in which Eu^{2+} ions accounted for 27 % in cation ratio, was a paramagnet down to 1.5 K and had a positive θ of 1 K in contrast to most amorphous oxides, although no explanation for the origin of the positive θ was provided. Despite of the fascinating fact, the magnetic properties of Eu^{2+}-containing amorphous oxides have been rarely investigated since then. Further studies on amorphous oxide systems with high concentration of Eu^{2+} are thus necessary to understand the magnetic interactions. Recently, Akamatsu *et al*. has prepared borate, silicate, and borosilicate glasses with Eu^{2+} concentration of 10 to 45 % (in cation ratio) by using a conventional

melt-quenching method, and found that all of as-obtained glasses exhibit positive θ values [9]. The result indicates that the ferromagnetic interactions are predominant among Eu^{2+} ions in any oxide glasses containing high concentration of Eu^{2+} ions. Besides, a para-ferromagnetic transition at around 2.2 K was observed in oxide glasses containing 45% Eu^{2+}; which is the first report of ferromagnetic amorphous oxide.

As mentioned in Chapter 1, crystalline $EuTiO_3$ is a rare antiferromagnet with predominant ferromagnetic interactions. Although its ground state is *G*-type antiferromagnetic, a small perturbation like an expansion of the lattice would result in a ferromagnetic ordering of the magnetic moments. Therefore it is of great interest to examine what the magnetic property of $EuTiO_3$ will be if its structure changes from crystalline phase to amorphous one. However, no studies on the magnetic properties of amorphous $EuTiO_3$ ($EuO\text{-}TiO_2$) have been reported up to now.

Based on these points, in this work we have systematically fabricated amorphous europium titanate thin films with nominal compositions of mEuO-TiO_2 (m=1, 2, 4) by a pulsed laser deposition (PLD) method and investigated their structural and magnetic properties. The amorphous nature of as-deposited thin films was confirmed by HRTEM images and selected-area electron diffraction (SAED) patterns as well as XRD patterns, and the valence state of europium ions was examined by ^{151}Eu CEM spectra. The local structure of Eu^{2+} ions were investigated by X-ray absorption fine structure (XAFS) spectroscopy. All of the thin films exhibit positive θ values, indicating that ferromagnetic interactions are dominant among Eu^{2+} ions. Analyses of AC magnetic susceptibilities indicate that with decreasing temperature the amorphous europium titanates reenter into a spin-glass phase after the ferromagnetic transition, suggesting the coexistence of ferromagnetic and antiferromagnetic interactions in such systems.

2.2 Experimental

Thin films of *m*EuO-TiO_2 (*m*=1, 2, 4) were deposited on silica glass substrates by the PLD method (see Fig. 2.1). The silica glass substrate and high-density target were set in a vacuum chamber with a base pressure of 10^{-6} Pa. A KrF excimer laser operated at a wavelength of 248 nm, a repetition frequency of 10 Hz, and an energy of 180 mJ was focused on the target. The film deposition was performed at room temperature under the base pressure (~10^{-6} Pa). The targets used for thin films deposition were prepared as follows:

(i) Target for deposition of EuO-TiO_2

A polycrystalline $EuTiO_3$ pellet was used as the target for the deposition of EuO-TiO_2. It was prepared from reagent-grade Eu_2O_3 and TiO_2 powders by a high-temperature solid-state reaction method. Firstly Eu_2O_3 and TiO_2 powders with a molar ratio of 1:1 were thoroughly mixed and sintered in air at 1400 ºC for 12 h to get a pure $Eu_2Ti_2O_7$ powder. The obtained $Eu_2Ti_2O_7$ powder was then annealed under a flowing gas of 95 vol % Ar + 5vol % H_2 at 1200 ºC for 24 h. After the mixture was reground thoroughly, the sintering process was repeated two more times. Finally, the obtained powder with a pure $EuTiO_3$ phase (see Fig. 2.2(a)) was pressed into a pellet and sintered again under the flowing gas of 95 vol % Ar + 5vol % H_2 at 1200 ºC for 24 h to get a dense target for PLD.

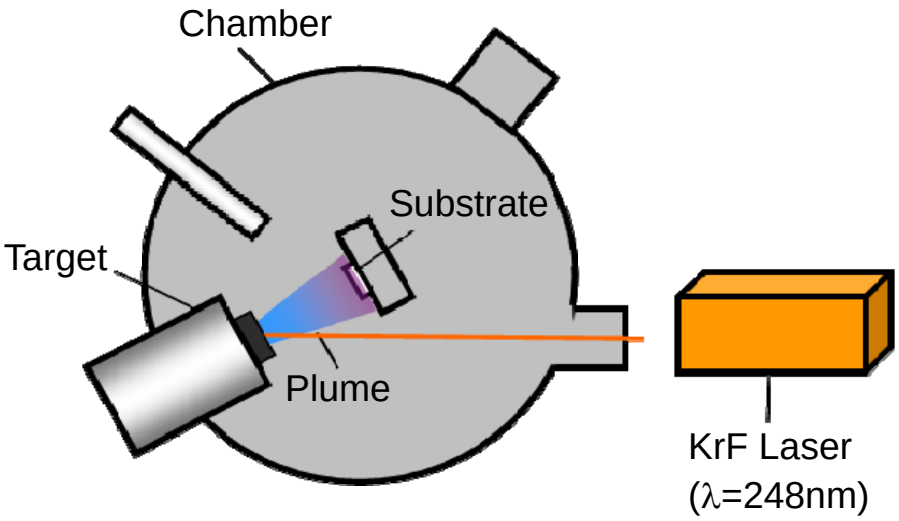

Fig. 2.1: A scheme for thin film fabrication using PLD in this work. A high-power KrF excimer laser (λ=248 nm, 10 Hz repetition frequency) is focused inside the high-vacuum chamber to strike the target and then the target material is vaporized in a plasma plume on the substrate to form a thin film.

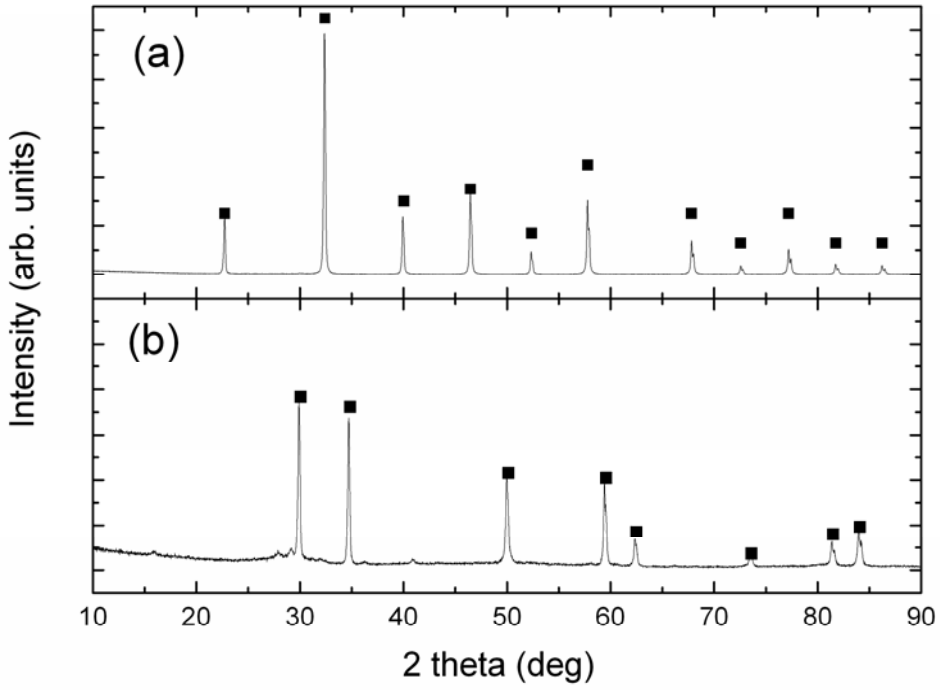

Fig. 2.2: Powder XRD patterns of polycrystalline $EuTiO_3$ (a) and EuO (b) powders. The solid squares stand for the expected reflection positions for $EuTiO_3$ and EuO, respectively.

(ii) Targets for deposition of 2EuO-TiO_2 and 4EuO-TiO_2

The targets used for the deposition of 2EuO-$TiO_2$and 4EuO-TiO_2 were prepared from EuO and TiO_2 powders in order to efficiently increase the Eu^{2+} concentration in the targets. To prepare EuO powder, Eu_2O_3 and slightly excessive graphite pwderes were thoroughly mixed and pressed into a pellet. The pellet was then sintered at 1450 ºC for 6 h in an Ar(95)/H_2(5) (vol %) atmosphere. The reaction is described by the formula: Eu_2O_3+C→2EuO+CO. Although the XRD pattern of the resultant product (see Fig. 2.2(b)) revealed the presence of a minor impurity phase identified as Eu_3O_4 (~2 wt%), the major crystalline phase was EuO. The resultant EuO pellet was reground into powder and thoroughly mixed with TiO_2 with a mole ratio of 2:1 to prepare the target for 2EuO-TiO_2 and 4:1 to prepare the target for 4EuO-TiO_2, respectively. The mixtures were again pressed into pellets and sintered at 1500 ºC for 10 h in the Ar(95)/H_2(5) (vol %) atmosphere. The obtained pellets were carefully polished and used for PLD deposition.

The thickness of the resultant thin films was estimated to be about 200 nm by a surface profiler (Alpha-Step IQ, KLA-Tencor). The molar ratios of Eu to Ti were evaluated to be 0.99:1, 2.04:1, and 3.75:1 for EuO-TiO_2, 2EuO-TiO_2 and 4EuO-TiO_2 thin films, respectively, by Rutherford backscattering (RBS) measurements and subsequent analysis with the simulation program SIMNRA.

The XRD analysis (Cu *Kα* radiation Rint2500, Rigaku) and SAED analysis combined with HRTEM observation (JEM-2100F, JEOL) were carried out to identify the amorphous nature of the resultant films. For the HRTEM observation, the cross-sectional specimen was prepared by an Ar ion milling at 5 kV using a liquid-nitrogen-cooling system. In order to examine the valence state, ^{151}Eu CEM

spectroscopy was performed at room temperature using $^{151}Sm_2O_3$ with activity of 1.85 GBq as a 21.5 keV γ-ray source. The velocity calibration was done with the magnetic hyperfine spectrum of α-Fe foil obtained using ^{57}Co-doped Rh as a 14.4 keV γ-ray source. Mössbauer spectrum of EuF_3 was utilized as a standard of Doppler velocity. As a reference, the CEM spectrum of EuS with rock-salt structure was also measured in order to determine the full width at half maximum (FWHM) of Eu^{2+} absorption peak in cubic symmetry; the FWHM for our experimental setup was estimated to be about 2.5 mm/s, which is comparable to the reported value [10].

XAFS spectra of the amorphous thin films were recorded at the beamline BL-12 of Photon Factory, National High Energy Institute of Japan. The storage ring operates under 2.5 GeV positron energy and 330 mA positron current. The beam was monochromatised by a double crystal Si (111) monochromator. The spectra were measured using a 19-element pure-Ge solid-state detector at the Eu L_3-edge and Ti K-edge at room temperature under a fluorescence detection mode. The obtained spectra were normalized to the edge-step height and energy after removing the background. The Eu L_3-edge X-ray absorption near-edge structure (XANES) spectra were further normalized to the first absorption maximum of each spectrum for estimation the fraction of Eu^{3+} in the thin films. The extended XAFS (EXAFS) structural analysis was performed using the ARTEMIS program [11], which makes use of theoretical standards from the FEFF6 [12]. The normalized EXAFS spectra were then Fourier transformed using the Hanning window in the range of k = 2–8 $Å^{-1}$ with a k^3 weighting. As references, the Eu L_3-edge XAFS spectra of bulk crystalline $EuTiO_3$, Eu_2O_3 and Ti k-edge ones of bulk crystalline Ti_2O_3 and TiO_2 were also measured under a transmission detection mode. By fitting their Fourier-transformed EXAFS spectra,

the values of passive electron reduction factor S_0^2 were evaluated to be 0.9 and 0.8 for the Eu L_3-edge and Ti K-edge spectra, respectively. These values were then used for analyzing the spectra of the amorphous thin films in order to evaluate the coordination number of Eu and Ti.

The magnetic measurements were carried out with a superconducting quantum interference device magnetometer (Quantum Design MPMS-XL). The DC magnetic susceptibilities were measured under zero-field-cooled (ZFC) and field-cooled (FC) modes at DC magnetic fields of 1, 10 and 100 Oe in a temperature region of 2-300K and the magnetization as a function of magnetic fields were obtained at 2 K in a magnetic field region of –5~5 T. The AC magnetic measurements were performed at an AC magnetic field of 1 Oe in a temperature region of 2-30 K and a frequency region of 0.1-300 Hz. DC magnetic fields of 0.1-5 Oe were applied for the DC magnetic field superimposed AC magnetic measurements.

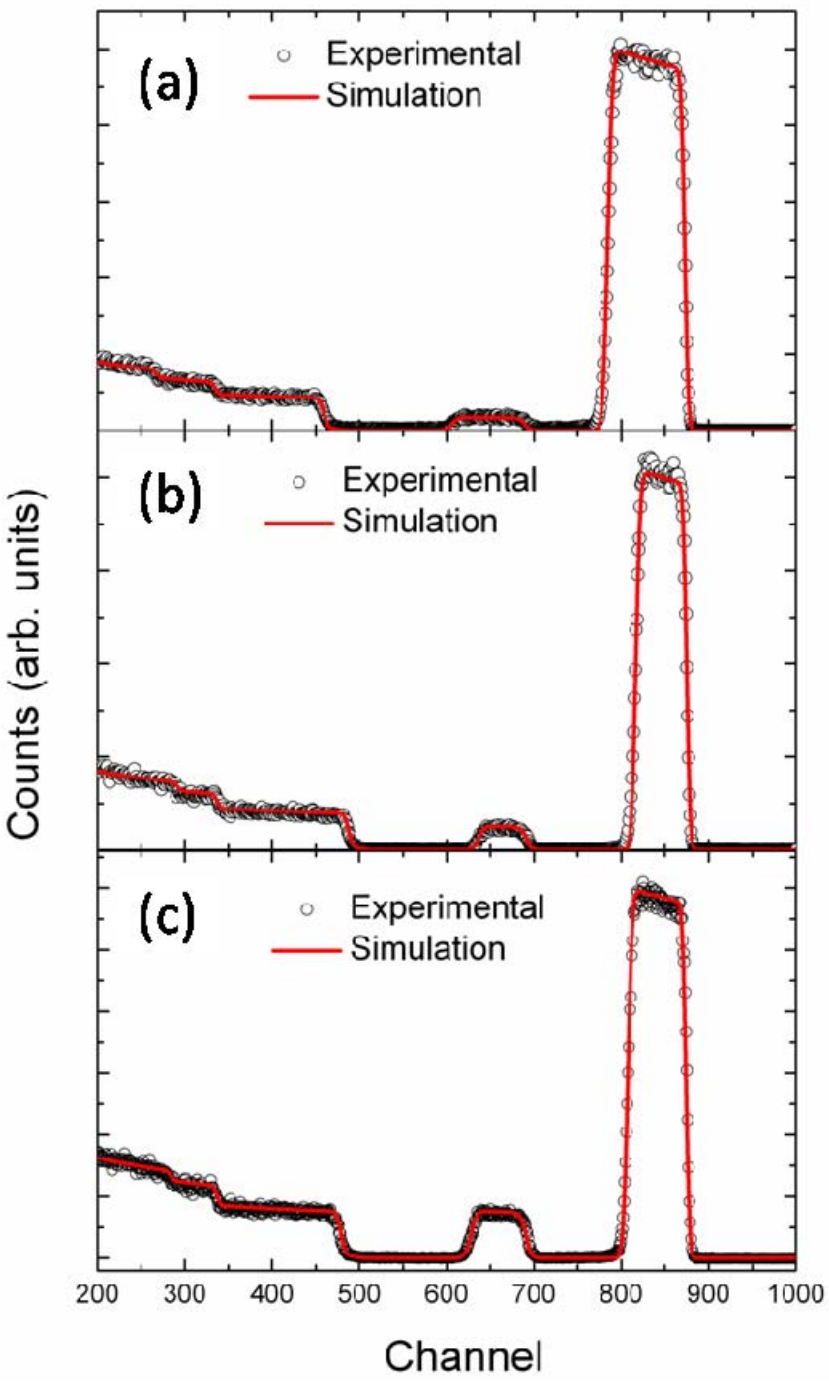

Fig. 2.3: Experimental (open circles) and the simulated (solid lines) RBS spectra of $EuO\text{-}TiO_2$ (a), $2EuO\text{-}TiO_2$ (b), and $4EuO\text{-}TiO_2$ (c).

2.3 Results and discussion

2.3.1 XRD analysis, TEM observation, and CEM spectroscopy

Figure 2.4 shows the XRD patterns for EuO-TiO_2 (a), 2EuO-TiO_2 (c) and 4EuO-TiO_2 (e) prepared by PLD method, respectively. No sharp diffraction peaks ascribed to crystalline phases are observed, indicating the amorphous nature of thin films. A broad peak around $2\theta = 20°$ and a shoulder around $2\theta = 30°$ arise from the silica glass substrate and thin films, respectively. The amorphous nature was further corroborated by HRTEM images and SAED patterns, as demonstrated in Fig. 2.4 (b), (d) and (f).

Figure 2.5 displays the room-temperature ^{151}Eu CEM spectra for EuO-TiO_2 (a), 2EuO-TiO_2 (b) and 4EuO-TiO_2 (c), respectively. The spectra mainly consist of two peaks around –13 and 0.5 mm/s, which are assigned to the absorptions due to Eu^{2+} and Eu^{3+}, respectively [13]. From the area ratio of the two absorptions, the fractions of Eu^{2+} over total Eu were estimated to be 97%, 90% and 70% for EuO-TiO_2, 2EuO-TiO_2 and 4EuO-TiO_2, respectively. Given that the Debye temperature (θ_D) for Eu^{2+} is lower than that for Eu^{3+} (e.g. $\theta_D = 145$ K and 261 K for Eu^{2+} and Eu^{3+} in a fluorozirconate glass, respectively [14]), the real concentrations of Eu^{2+} are expected to be larger than the values obtained above. Also, the content of Eu^{3+} in 4EuO-TiO_2 may be over estimated because CEM measurements preferentially probe the surface layer of the thin films which is easily subject to oxidation. A close look at Fig. 2.5 reveals that the Eu^{2+} absorption bands are split due to the quadrupole interactions between the electric field gradient and the electric quadrupole moment of ^{151}Eu nucleus [13]. Therefore, we have analyzed the Eu^{2+} absorption bands with the method developed by Shenoy and

Dunlap [15]. The γ-ray resonance energy between excited and ground states is given by

$$R(I_Z^*, I_Z) = eV_{ZZ}[Q_e P(I^*, I_Z^*) - Q_g P(I, I_Z)] + \delta\,, \tag{2.1}$$

where e is the elementary charge, V_{zz} is the electric field gradient in the direction z, Q_e and Q_g are the excited- and ground-state nuclear quadrupole moments, respectively, I^* and I are the excited- and ground-state nuclear spins, respectively, I_z^* and I_z are the z projections of excited- and ground-state nuclear spins, respectively, and δ is the isomer shift. $P(I^*, I_z^*)$ and $P(I, I_z)$ are written as

$$P(I, I_Z) = \sum_{N=0}^{4} a_N(I, I_Z)\eta^N\,, \tag{2.2}$$

where η is the asymmetry parameter of the electric gradient, and $a_N(I, I_z)$ is the eigenvalue coefficients (see Ref. 15). The transition intensity is expressed by

$$A(I^*, I_Z^*, I, I_Z) = \sum_{N=0}^{4} b_N(I^*, I_Z^*, I, I_Z)\eta^N\,, \tag{2.3}$$

where $b_N(I^*, I_z^*, I, I_z)$ is the intensity coefficient (see Ref. 15). For ^{151}Eu, $I^* = 7/2$, $I = 5/2$, and $Q_e/Q_g = 1.34$ [16], and thus, there are 12 possible transitions in the presence of quadrupole interactions. In the calculation of theoretical spectrum for Eu^{2+} absorption bands, we assume that each absorption line of the 12 transitions is represented by a Lorentzian with FWHM of γ, which reflects the site-to-site variation of Eu^{2+}. We also neglect the magnetic hyperfine interactions because the amorphous thin films are paramagnetic at room temperature as described below. For the Eu^{3+} absorption bands, a single Lorentzian was simply used to reproduce the spectral shape due to the poor spectral resolution. The background curve was corrected with the equation proposed by Marshall *et al*. [17].

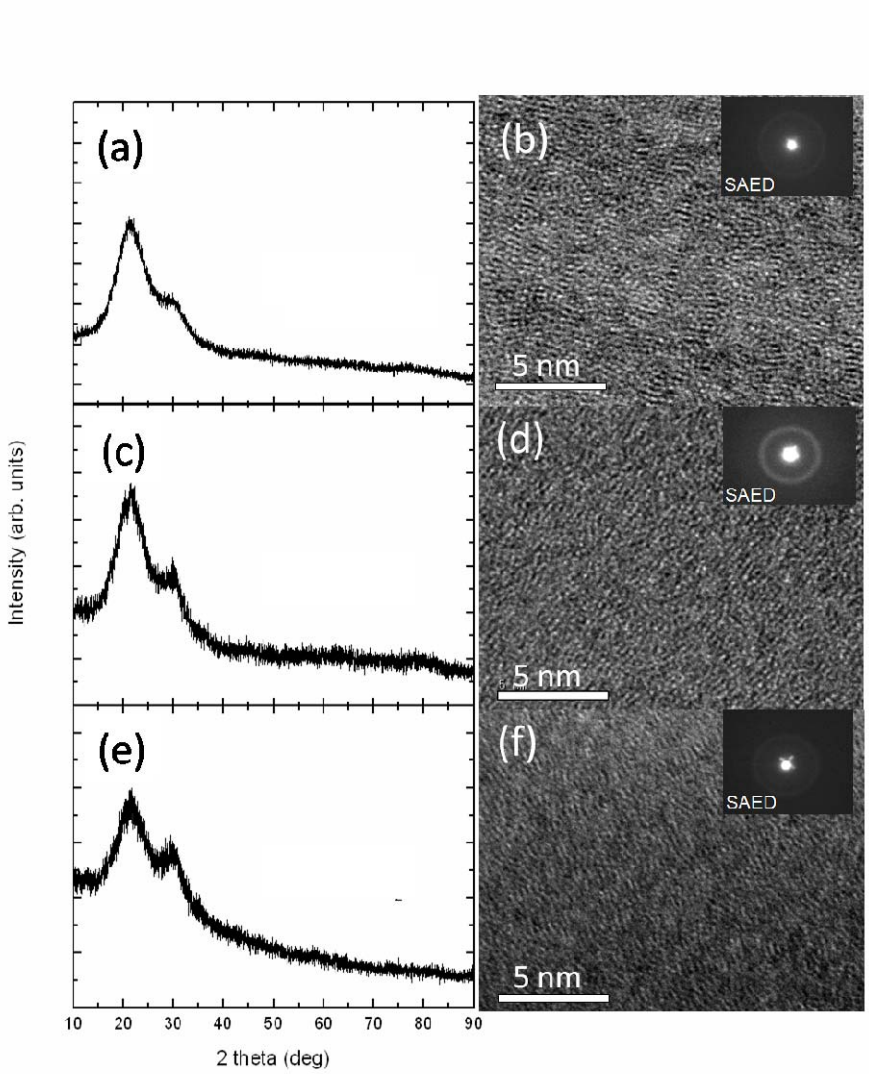

Fig. 2.4: XRD patterns (a,c,e) and TEM images (b,d,f) of EuO-TiO_2, 2EuO-TiO_2, and 4EuO-TiO_2, respectively. The inset in TEM images are SAED patterns.

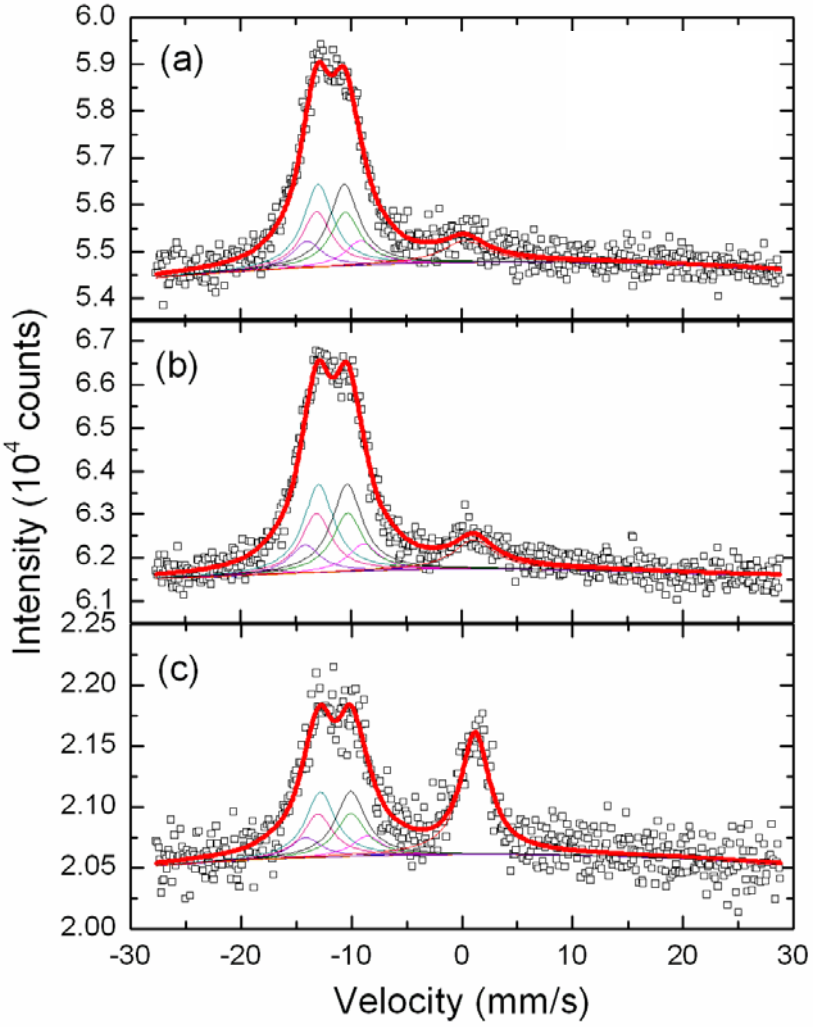

Fig. 2.5: ^{151}Eu CEM spectra measured at room temperature for EuO-TiO_2 (a), 2EuO-TiO_2 (b), and 4EuO-TiO_2 (c). The open squares represent the experimental data, and the solid lines are the fit of theoretical curve using Eqs. (2.1)-(2.3). The component lines corresponding to the 12 transitions are also shown for the Eu^{2+} absorption peak at around –12 mm/s.

The parameters obtained by fitting the CEM spectra are shown in Table 2.1. For oxides containing Eu^{2+}, the δ value reflects the electron density at the nucleus and can be a measure of the covalency of Eu^{2+}-O bond and/or the coordination number of Eu^{2+} [18]. The magnitude of δ for mEuO-TiO_2 (m=1, 2, 4) is smaller than that for crystalline $EuTiO_3$ with cubic perovskite-type structure (–12.5 mm/s) and decreases with the value of m, indicating an increase in the covalency of Eu^{2+}-O bond and/or a decrease in the coordination number of Eu^{2+} from crystalline to amorphous phase and with the value of m. Moreover, the non-zero quadrupole interaction parameters ($eV_{zz}Q_g$) and non-zero asymmetry parameters (η) indicate the deviation of the structure from cubic symmetry and the absence of axial symmetry for the coordination structure around Eu^{2+} in the amorphous thin films. In the case of Eu^{2+} with $^8S_{7/2}$ ground state, the quadrupole interaction parameter reflects the electric field gradient caused by the surrounding ligands (oxide ions in this case), because the resultant zero orbital angular momentum leads to no valence contribution [18]. The magnitude of $eV_{zz}Q_g$ for the amorphous thin films is comparable to those for the Eu^{2+}-containing bulk oxide glasses as reported previously ($eV_{zz}Q_g$ = –11.20 ~ –17.98 mm/s) [7,18,19] and increases with the value of m in mEuO-TiO_2 (m=1, 2, 4). The increase in the magnitude of $eV_{zz}Q_g$ suggests an increase in the asymmetry of the distribution of electrons supplied by oxide ions around a Eu^{2+} ion [19]. The values of γ are consistent for the three amorphous thin films and slightly larger than that for Eu^{2+} in a cubic site (2.5 mm/s), which is due to the site-to-site variation or the distortion of the amorphous structure.

Table 2.1: Parameters obtained by the fit of the CEM spectra using Eqs. (2.1)-(2.3).

	Eu^{2+}/Eu	δ (mm/s)	$eV_{zz}Q_g$ (mm/s)	η (mm/s)	γ (mm/s)
$EuO\text{-}TiO_2$	0.97	-11.8	-14.7	0.86	3.2
$2EuO\text{-}TiO_2$	0.90	-11.7	-15.7	0.93	3.3
$4EuO\text{-}TiO_2$	0.70	-11.5	-16.4	0.96	3.2

2.3.2 Eu L_3-edge and Ti K-edge XAFS

The Eu L_3-edge XANES spectra of mEuO-TiO_2 (m=1, 2, 4) are shown in Fig. 2.6 (a). The spectra of crystalline $EuTiO_3$ and Eu_2O_3 are also shown as references. The peak around 6970 eV and the shoulder around 6980 eV are ascribed to the absorptions of Eu^{2+} and Eu^{3+}, respectively. The absorption of Eu^{3+} ions in $4EuO\text{-}TiO_2$ is much stronger than those in $EuO\text{-}TiO_2$ and $2EuO\text{-}TiO_2$, indicating the existence of a relatively large amount of Eu^{3+} in $4EuO\text{-}TiO_2$. However, similar to the CEM measurement, XAFS measurements mainly detect the surface layer of the thin films, by which the amount of Eu^{3+} could be overestimated. A close look at Fig. 2.6 (a) in the energy region around the absorption edge is shown in Fig. 2.6 (b). The edge energy is decreased by 1 eV from crystalline $EuTiO_3$ to $EuO\text{-}TiO_2$ and slightly decreased with the increase of Eu^{2+} concentration in the amorphous thin films. Since the edge energy position is an approximate measure of the oxidation state of the absorbing atom and the covalency of bonding at given oxidation state, the decrease in edge energy indicates an increase in Eu-O bond covalency, which agrees with the results obtained from CEM spectra.

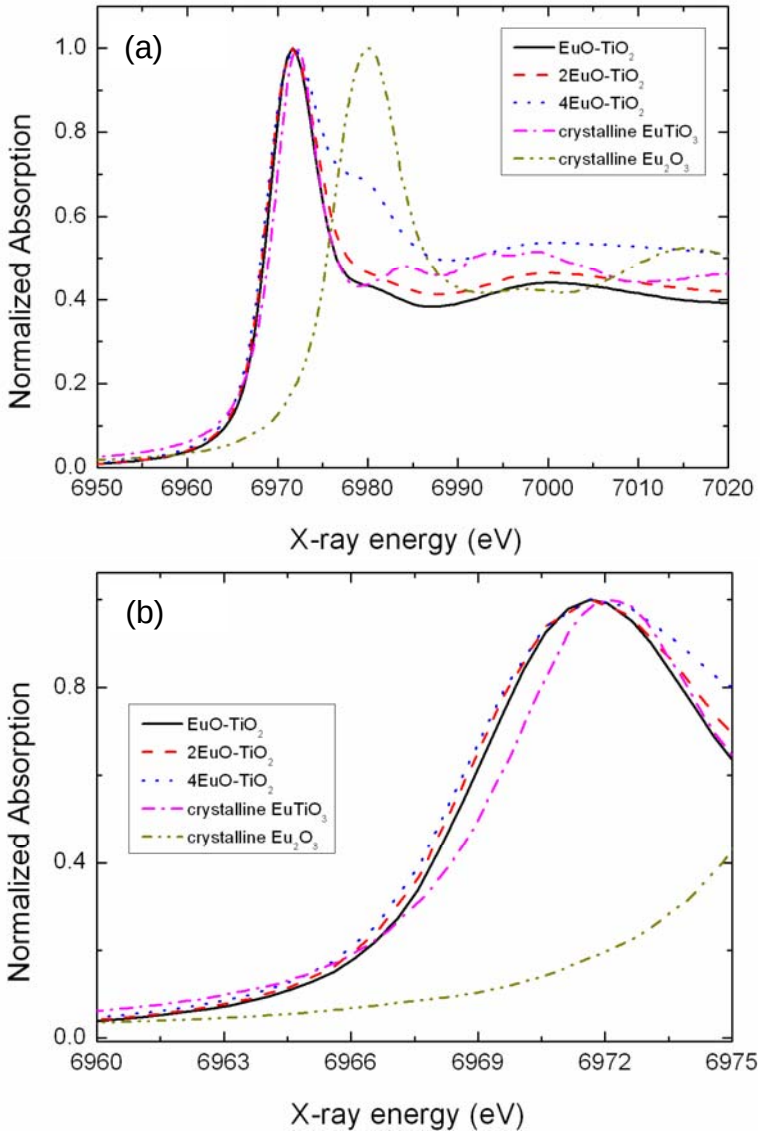

Fig. 2.6: (a) Normalized XANES spectra of the amorphous thin films. The spectra of crystalline $EuTiO_3$ and Eu_2O_3 are shown as reference. (b) A close look at (a) in the low energy region.

Table 2.2: Parameters obtained by fitting the Eu L_3-edge EXAFS spectra.

	n_{Eu2+}	$d_{Eu\text{-}O}$ (Å)	$\sigma^2_{Eu\text{-}O}$ (Å^2)
EuO-TiO_2	6.4(4)	2.480(1)	0.020(2)
2EuO-TiO_2	6.3(4)	2.472(6)	0.022(1)
4EuO-TiO_2	3.9(4)	2.431(7)	0.022(3)

Figure 2.7 shows the Fourier transform of the EXAFS oscillations for Eu. Only the peak around 1.9 Å corresponding to the first Eu-O shell was well developed due to the absence of local symmetry around Eu in the amorphous structure. By fitting this peak with a Quick First Shell (QFS) model of 6-cordinate crystal, the average coordination number of Eu^{2+} (n_{Eu2+}), the Eu-O bond distance ($d_{Eu\text{-}O}$) and the bond disorder ($\sigma^2_{Eu\text{-}O}$) were obtained, as shown in Table 2.2. The magnitudes of n_{Eu2+} and $d_{Eu\text{-}O}$ in EuO-TiO_2 and 2EuO-TiO_2 are much smaller than those in crystalline $EuTiO_3$ (n_{Eu2+}=12 and $d_{Eu\text{-}O}$=2.75 Å) and Eu_2TiO_4 (n_{Eu2+}=9 and $d_{Eu\text{-}O}$(avg)=2.70 Å), but very close to those in crystalline EuO (n_{Eu2+}=6 and $d_{Eu\text{-}O}$=2.57 Å), indicating that the local structures of Eu^{2+} ions in EuO-TiO_2 and 2EuO-TiO_2 thin films are possibly similar to that in EuO. A similar phenomenon has been observed in amorphous $SrTiO_3$ whose crystalline counterpart has the same structure to that of crystalline $EuTiO_3$; the coordination number of Sr^{2+} and the Sr-O bond distance were estimated to be 6.5 and 2.52 Å, respectively [20]. The values of n_{Eu2+} and $d_{Eu\text{-}O}$ decrease with the increase of m in mEuO-TiO_2 (m=1, 2, 4). The decrease of n_{Eu2+} with the increase of m is consistent with that obtained by CEM measurement.

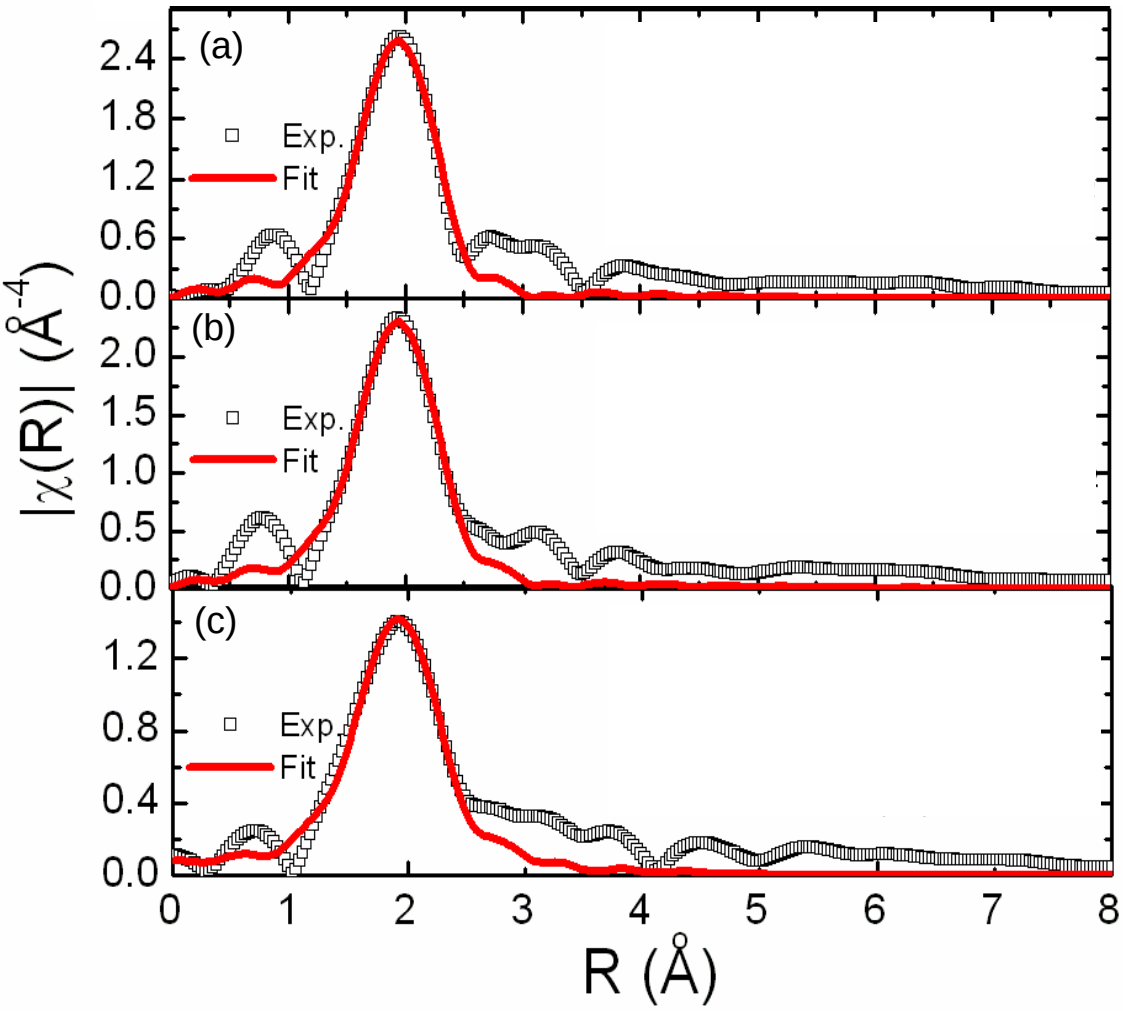

Fig. 2.7: Results of EXAFS fitting for EuO-TiO_2 (a), 2EuO-TiO_2 (b), and 4EuO-TiO_2 (c). The open squares are the Fourier transform of the Eu L_3-edge EXAFS oscillations and lines are the fit.

Figure 2.8(a) shows the Ti *K*-edge XANES spectra of the amorphous thin films as well as those of crystalline $EuTiO_3$ and anatase as references. The spectra of the thin films contain a pronounced pre-edge peak corresponding to the 1*s*-3*d* transition. The intensity of this peak is much stronger than those of crystalline $EuTiO_3$ and anatase, indicating that the local environment of the Ti in the thin films is noncentrosymmetric [21]. The information of the pre-edge peak has been used to distinguish the coordination state of Ti. It has been found that for 4-fold, 5-fold, and 6-fold coordinated Ti compounds, the correlation between the intensity and energy of the pre-edge peak separates into different domains, as shown in Fig. 2.8(b) [22]. By aligning the data obtained in this work with those reported in Ref. 22 using anatase for calibration, the correlation between the intensity and energy of the pre-edge peaks for the amorphous thin films almost falls into the domain of 4-fold coordination, suggesting the average coordination number of Ti in the amorphous thin films is near 4.

The local structure of Ti in the amorphous thin films was further evaluated through Ti *K*-edge EXAFS spectra. Figure 2.9 shows the Fourier transform of the Ti *K*-edge EXAFS oscillation. The spectra are dominated by a peak around 1.4 Å due to the absorption of the first Ti-O shell, which again confirms the disordered structure of the thin films. An octahedral QFS model was adopted to analyze this peak. The average coordination number of Ti^{4+} (n_{Ti4+}), the nearest Ti-O bond distance ($d_{Ti\text{-}O}$) and the bond disorder ($\sigma^2_{Ti\text{-}O}$) derived by fitting the theoretical curve to the experimental spectra are shown in Table 2.3. The values of n_{Ti4+} are consistent with the results of the XANES spectra and very close to those in the Ti^{4+}-containing oxide glasses [23]. It has been known that TiO_2 usually acts as an intermediate oxide or network-modifying oxide since it doesn't form glass by itself [24]. However, Sakka *et al*. [23] reported that

TiO_2 can be a glass-forming oxide in glasses (e.g., $K_2O \cdot TiO_2$, $Cs_2O \cdot TiO_2$, and so on) where Ti^{4+} ions have a small coordination number (i.e. $n_{Ti4+} = 4$) based on the concept of Zachariasen [24]. The low magnitudes of n_{Ti4+} in the present thin films suggest that Ti^{4+} serves as a glass-forming cation in the amorphous structure. Furthermore, the values of $d_{Ti\text{-}O}$ are smaller than those in crystals containing TiO_6 octahedra but comparable to those in crystals and glasses where Ti^{4+} ions are four coordinated by oxide ions [23,25-28], which confirms the low coordination state of Ti^{4+} in the amorphous thin films.

Table 2.3: Parameters obtained by fitting the Ti *K*-edge EXAFS spectra.

	n_{Ti4+}	$d_{Ti\text{-}O}$ (Å)	$\sigma^2_{Ti\text{-}O}$ (Å^2)
EuO-TiO_2	3.9(8)	1.88(1)	0.010(2)
2EuO-TiO_2	3.7(5)	1.830(8)	0.003(1)
4EuO-TiO_2	4.1(5)	1.850(8)	0.004(2)

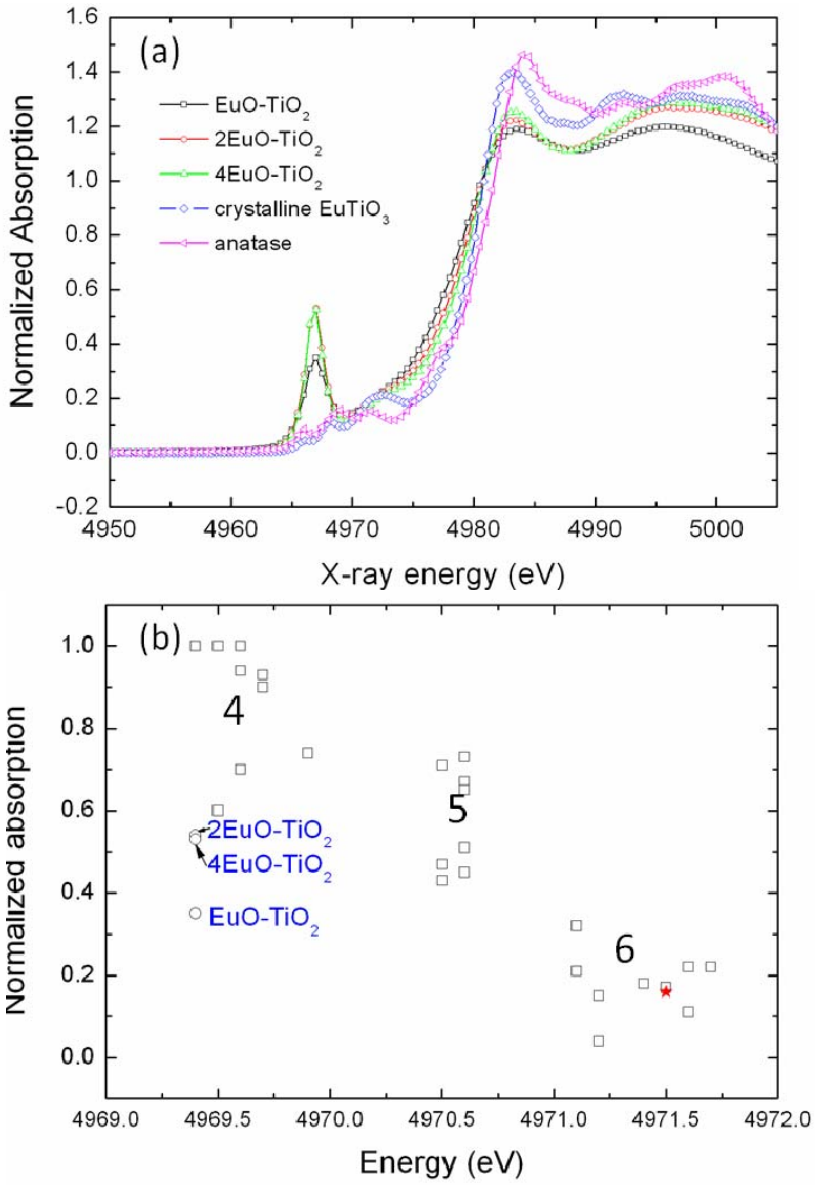

Fig. 2.8 (a) Ti *K*-edge XANES spectra. (b) Correlation between the intensity and energy of the pre-edge peak. The open squares, the solid star and the open circles refer to the data of different reference compounds taken from Ref. 22, that of anatase obtained in this work, and those of the amorphous thin films, respectively.

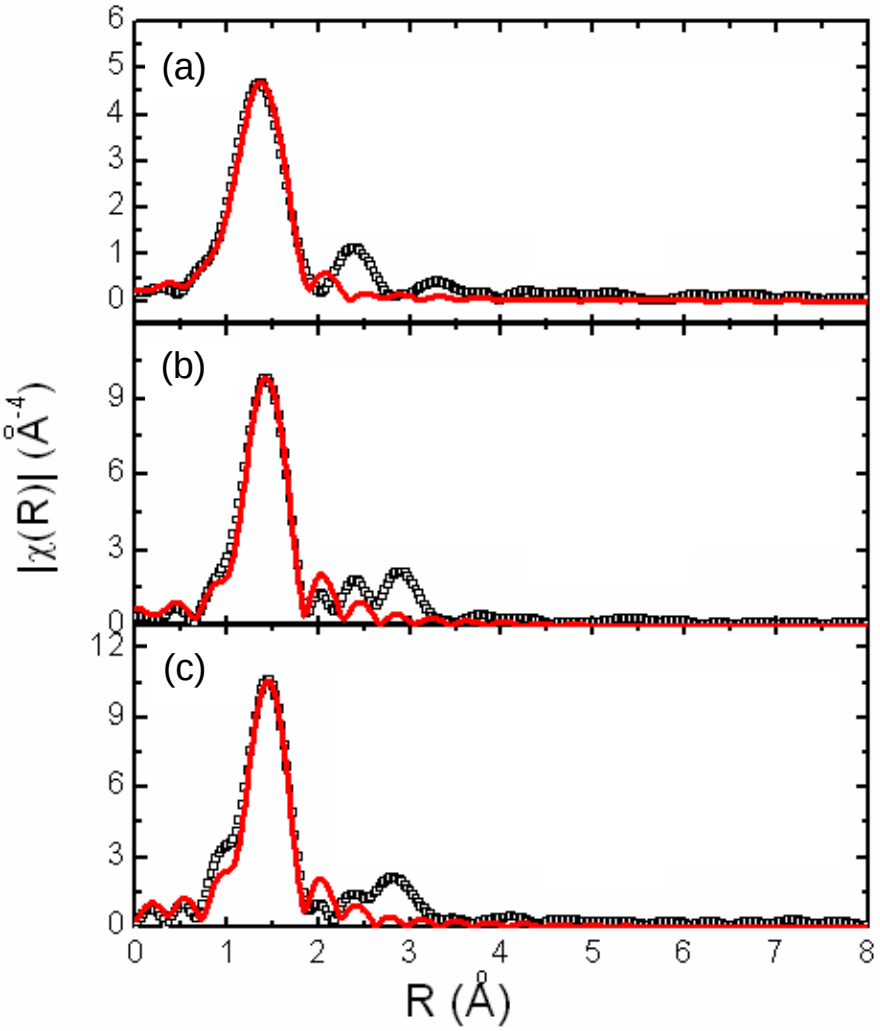

Fig. 2.9: Results of EXAFS fitting for EuO-TiO_2 (a), 2EuO-TiO_2 (b), and 4EuO-TiO_2 (c). The open squares are the Fourier transform of the Ti *K*-edge EXAFS oscillations and lines are the fit.

2.3.3 Magnetic properties

Figure 2.10(a) shows the temperature dependence of magnetizaiton, $M(T)$, measured under both ZFC and FC conditions in a magnetic field of 100 Oe for mEuO-TiO_2 (m=1, 2, 4) along the out-of plane axis. The thin films exhibit paramagnetic behaviors in the high temperature region. With decreasing temperature, an abrupt increase can be observed in the $M(T)$ curves, which indicates a magnetic transition from paramagnetic to ferromagnetic phase. The ferromagnetic transition temperatures T_C, defined by the infection point of the $M(T)$ curve, were estimated to be 5, 13 and 19 K for EuO-TiO_2, 2EuO-TiO_2 and 4EuO-TiO_2, respectively. Here, it is worth to mention that the value of T_C for EuO-TiO_2 is comparable to the magnetic transition temperature of crystalline $EuTiO_3$ (T_N =5.5 K [17]), while that for 2EuO-TiO_2 is higher than crystalline Eu_2TiO_4 (T_C =9 K [17]). These results are contrary to the usual understanding that magnetic transition temperature will be suppressed when the structure is transformed from crystalline phase to amorphous one [29].

The inverse magnetic susceptibility as a function of temperature $\chi^{-1}(T)$ (Fig. 2.10(b)) shows a linear relation above 10 K and is describable in terms of the Curie-Weiss law:

$$\chi = \frac{N_A(\mu_{eff})^2}{3k(T-\theta)}, \tag{2.4}$$

where N_A is the Avogadro's constant, μ_{eff} is the effective magnetic moment of Eu^{2+}, k is the Boltzmann constant. By fitting Eq. (2.4) to $\chi^{-1}(T)$, the values of θ were obtained as 8, 18, and 23 K for EuO-TiO_2, 2EuO-TiO_2 and 4EuO-TiO_2, respectively. The positive values of θ suggest that ferromagnetic interactions are dominant in the amorphous thin

films, which is consistent with the previous report on Eu^{2+}-containing glasses. Figure 2.10(c) shows θ as a function of the Eu^{2+} content for the amorphous thin films as well as the previously reported Eu^{2+}-containing oxide glasses. The value of θ approximately exhibits an exponential increase with the increase of Eu^{2+} concentration. Since the value of θ is proportional to the sum of all the magnetic interactions in the system, the exponential increase in θ indicates that the ferromagnetic interactions are strengthened with the increase of Eu^{2+} concentration. Also, the values of θ in EuO-TiO_2 and 2EuO-TiO_2 are significantly higher than their crystalline counterparts (θ=3.8 and 10 K for crystalline $EuTiO_3$ and Eu_2TiO_4 [17], respectively), which suggests an enhancement of the ferromagnetic interactions by amorphization.

In order to gain a deep insight into the magnetic behaviors at lower temperatures, the magnetization of the amorphous thin films was measured under lower magnetic fields. Figure 2.11(a) shows the $M(T)$ curves of EuO-TiO_2 measured at magnetic fields of 1 and 10 Oe. Below the sharp increase due to the ferromagnetic transition, a discrepancy between the ZFC and FC curves appears, indicating that the (meta)stable states in ZFC and FC modes are different. Apparently, there is some phenomenon (e.g. spin frustration) takes place at lower temperatures and breaks the ferromagnetic coupling.

The magnetization as a function of applied field ($M(H)$) was measured at 2 K for all the thin films. Figure 2.11(b) shows the $M(H)$ curve of EuO-TiO_2 as an example. The magnetization increases rapidly with increasing magnetic field in a low-field region and tends to be saturated at a field higher than 1 T. However, since the Eu^{2+} spins can be easily flipped perpendicular to the applied magnetic field due to the small magnetic anisotropy, the hysteresis loop in Fig. 2.11 (b) is not clearly observed.

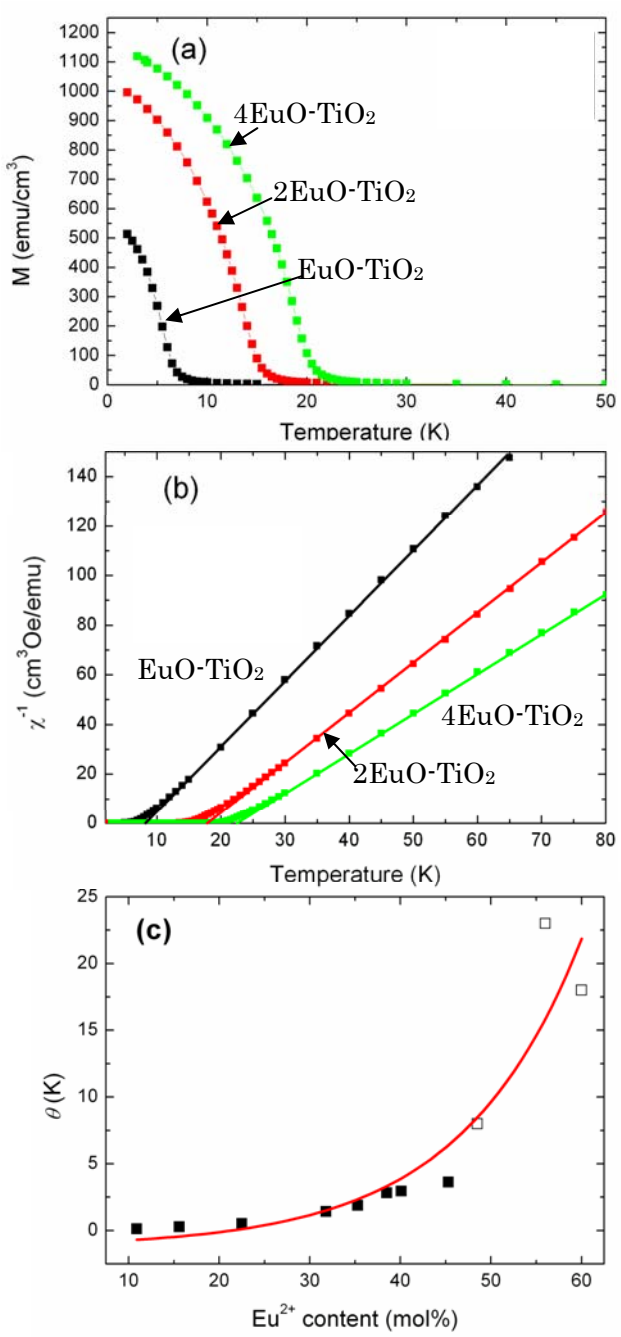

Fig. 2.10: (a) $M(T)$ curves of mEuO-TiO_2 (m=1, 2, 4) measured at magnetic field of 100 Oe. (b) $\chi^{-1}(T)$ for mEuO-TiO_2 (m=1, 2, 4) measured at magnetic field of 100 Oe (filled squares) as well as the fit of Curie-Weiss law to the experimental data (solid line). (c) The value of θ as a function of Eu^{2+} concentration for Eu^{2+}-containing glasses (solid squares, taken from Ref. 10) and the present thin films (open squares). The solid line is an exponential fit to the experimental data.

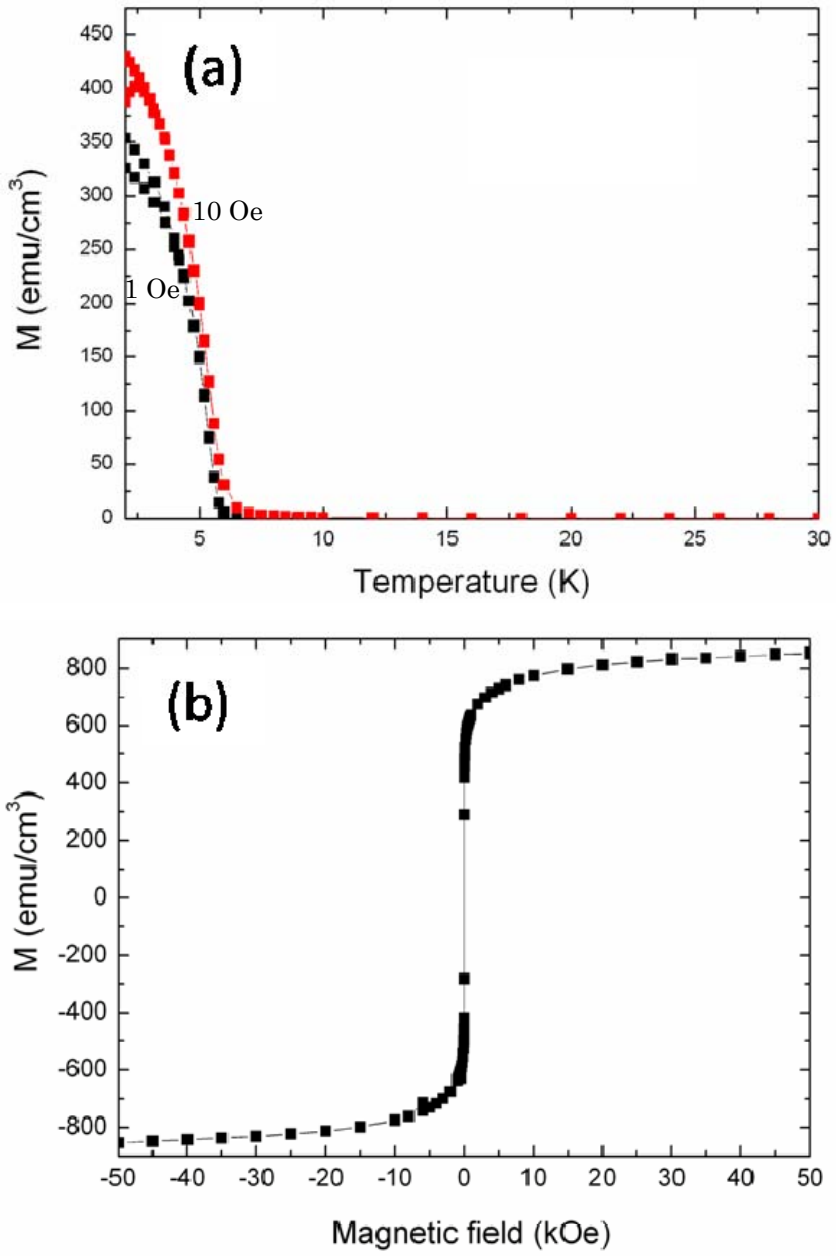

Fig. 2.11: (a) $M(T)$ curves of EuO-TiO_2 measured at magnetic field of 1 and 10 Oe. (b) $M(H)$ of EuO-TiO_2 measured at 2 K.

The magnetic properties of the amorphous thin films were further studied through the measurements of AC magnetization. Figure 2.12 depicts the temperature-dependent in-phase ($M'(T)$) and out-of-phase ($M''(T)$) components of AC magnetization measured with frequency (f) varying from 0.1 to 300 Hz. The applied AC magnetic field is 1 Oe. The M'(T) together with $M''(T)$ curves exhibit similar behaviors for the three thin films. The $M'(T)$ curves show an f-independent sharp increase upon cooling which is in accordance with the ferromagnetic transition seen in the $M(T)$ curves. Then with further decreasing temperature, the $M'(T)$ curves exhibit maxima with f-dependent intensities and positions. The peak positions are shifted to higher temperatures and the peak intensity is suppressed with increasing f. Correspondingly the $M''(T)$ curves exhibit f-dependent peaks and the peak positions are shifted to higher temperatures with increasing f. These features are in contrast to those of conventional ferromagnets which have almost f-independent peaks in $M'(T)$ and $M''(T)$ curves but reminiscent of spin glass behavior.

The peak temperature of the $M'(T)$ curves can be viewed as spin freezing temperature (T_f). The f-dependent shift of T_f, $\varphi = \Delta T_f/(T_f \Delta \log f)$, were evaluated to be 0.01, 0.02 and 0.0004 for EuO-TiO_2, 2EuO-TiO_2 and 4EuO-TiO_2, respectively. The values of φ for EuO-TiO_2 and 2EuO-TiO_2 are comparable to while that for 4EuO-TiO_2 is one order smaller than those for conventional spin glasses [30]. The f dependence of T_f is also analyzed by the power law which is a well-known testing equation for the spin glass phenomenon [31]:

$$\tau = \tau_0 \left(\frac{T_f - T_c}{T_c}\right)^{-z\nu} \tag{2.5}$$

where τ is equal to $1/f$, τ_0 is a characteristic relaxation time, T_c is a critical temperature

and $z\nu$ is a critical exponent. The obtained τ_0, T_c and $z\nu$ are shown in Table 2.4. The values of τ_0 are much smaller than those for conventional spin glasses (10^{-13} s) and the values of $z\nu$ are larger than any reported one [30-33]. Therefore it seems that the power law is not applicable to the present thin film systems. This is probably due to the closeness of the ferromagnetic and spin-glass transitions: the systems run into spin glass phase immediately after the ferromagnetic magnetic transitions with decreasing temperature. Both the ferromagnetic and the spin glass transition contribute to the peak in the $M'(T)$ curve. In the case of 4EuO-TiO_2, the ferromagnetic transition smears out the spin glass transition, which results in a very small φ. On the contrary, the relatively weak ferromagnetic transition peaks were overlapped by the spin glass ones for EuO-TiO_2 and 2EuO-TiO_2. Therefore the values of φ for EuO-TiO_2 and 2EuO-TiO_2 are comparable to those for conventional spin glasses. The systems which undergo a spin glass transition after a ferromagnetic transition are called as reentrant spin glasses.

Table 2.4: The values of τ_0, T_c and $z\nu$ obtained from Eq. (2.5).

	τ_0 (s)	T_c (K)	$z\nu$
EuO-TiO_2	9×10^{-19}	5	17
2EuO-TiO_2	2×10^{-17}	10	20
4EuO-TiO_2	6×10^{-49}	18	25

The reentrant spin glass nature of the thin films is corroborated by the measurement of DC magnetic field superimposed AC magnetization. Figure 2.13(a) shows the temperature dependent AC magnetization of EuO-TiO_2 measured at an applied AC field of 1 Oe with f =10 Hz under different DC fields. Both $M'(T)$ and $M''(T)$ curves are significantly suppressed by applying the DC fields. The inset of Fig.

2.13(a) is a close look at the $M'(T)$ curves, from which the two peaks ascribed to the spin glass (T_f) and ferromagnetic (T_C) transitions, which overlap with each other in the absence of DC field, can be observed when the amplitude of DC field reaches 5 Oe. Figure 2.13(b) depicts the frequency-dependent AC magnetization measured at an AC field of 1 Oe and a DC field of 5 Oe. With increasing f, T_f shifts to higher temperatures while T_C keeps unchanged for all frequencies. This again confirms the ferromagnetic and reentrant spin glass transitions in the amorphous thin films.

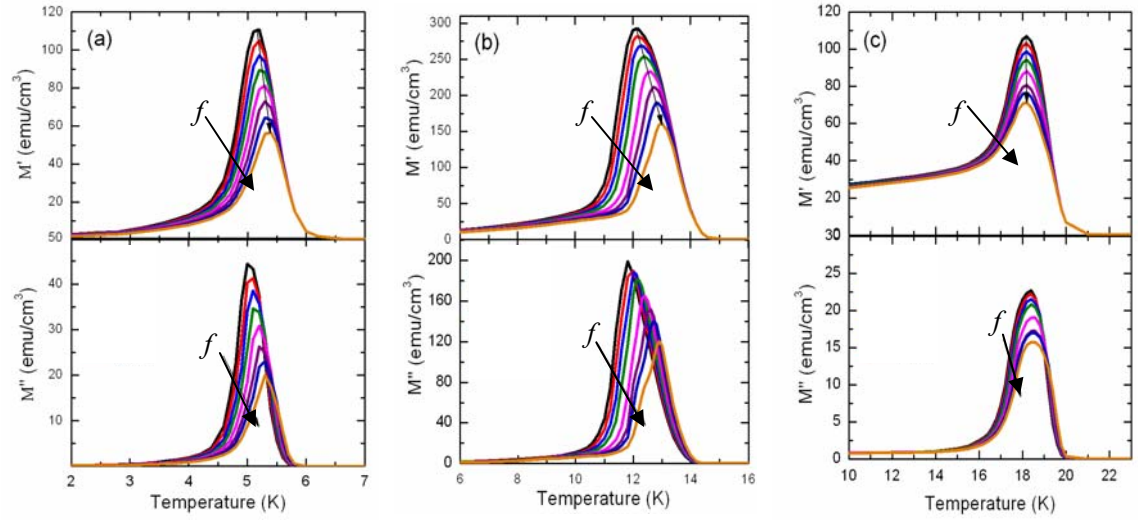

Fig. 2.12: $M'(T)$ and $M''(T)$ for EuO-TiO_2 (a), 2EuO-TiO_2 (b), and 4EuO-TiO_2 (c) measured at AC field of 1 Oe with f of 0.1, 0.3, 1, 3, 10, 30, 100, and 300 Hz (from top to end).

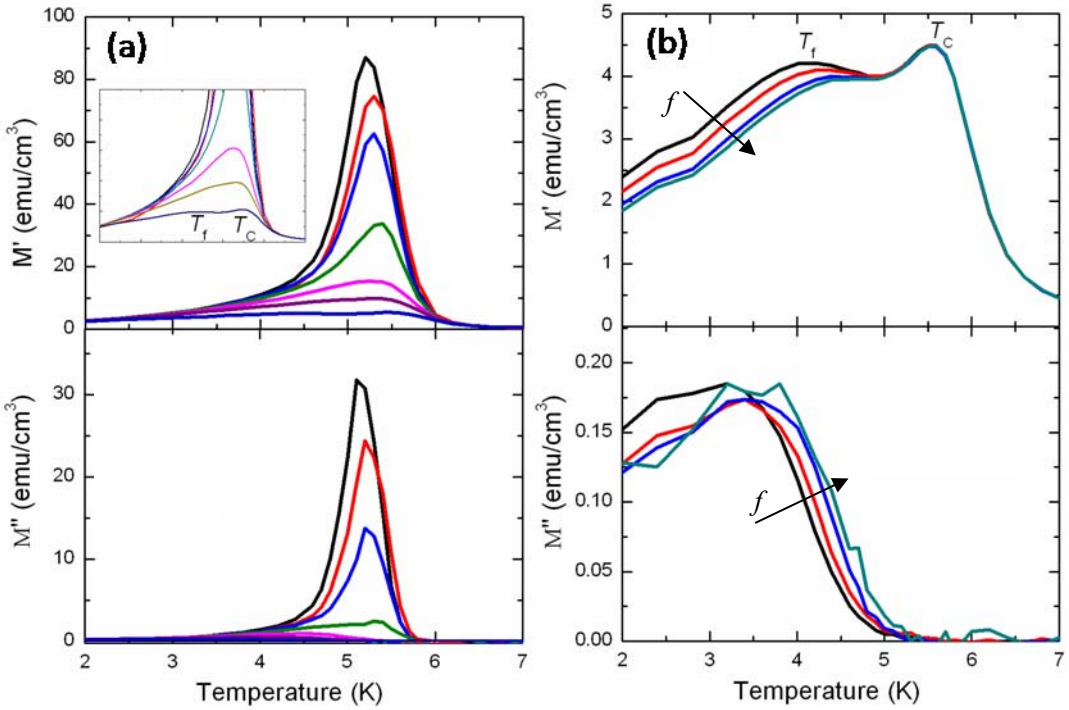

Fig. 2.13: (a) $M'(T)$ and $M''(T)$ for the EuO-TiO_2 measured at AC field of 1 Oe and superimposed DC fields of 0, 0.1, 0.2, 0.5, 1, 2, 5 Oe (from up to down). The inset of (a) is an enlarge show of $M'(T)$. (b) $M'(T)$ and $M''(T)$ at an AC field of 1 Oe and a DC field of 5 Oe with f of 1, 10, 100, and 300 Hz (from top to end).

The magnetic mechanism in amorphous europium titanate thin films can be understood as follows:

I. The predominance of ferromagnetic interactions results in ferromagnetic transition.

As mentioned above, ferromagnetic interactions are dominant in the present amorphous thin films. The random distribution of Eu^{2+} ions as well as the predominance of ferromagnetic interactions is supposed to result in ferromagnetic ordering of the magnetic moments. It should be noted that the amorphization of crystalline $EuTiO_3$, which breaks the delicate balance between antiferromagnetic and ferromagnetic ordering, is an effective and easy way to drive it from antiferromagnetic to ferromagnetic phase. The enhancement of ferromagnetic interactions in amorphous phase and with the increase of m in mEuO-TiO_2 (m=1, 2, 4) is probably due to the variation of the structure. As indicated by the EXAFS results, the Eu^{2+} ions in EuO-TiO_2 and 2EuO-TiO_2 have local environment similar to those in EuO. Since the ferromagnetic interactions in EuO are much stronger than those in crystalline $EuTiO_3$ and Eu_2TiO_4 [16], a change of the structure of $EuTiO_3$ and Eu_2TiO_4 from crystalline to amorphous phase could strengthen the ferromagnetic interactions. Also, the decrease in the values of n_{Eu2+} and $d_{Eu\text{-}O}$ with the increase of m, which tends to reduce the number of antiferromagnetic 90° superexchange interactions and intensify the ferromagnetic indirect interactions between NN Eu^{2+} ions, can result in enhancement of ferromagnetic interactions.

II. Coexistence of ferromagnetic and antiferromagnetic interactions leads to reentrant spin glass transition.

The amorphous structure of the thin films has wide distributions of Eu-O-Eu angles and Eu-Eu distances. Therefore antiferromagnetic superexchange interactions

besides the ferromagnetic interactions are also expected to exist in the systems and the competition between the two kinds of magnetic interactions could result in spin frustration. The process of the reentrant spin glass transition can be described by a random-field theory [34-37]. In this theory, the reentrant spin glass system contains a ferromagnetic part with high spin concentration and a spin glass part with low spin concentration together with an interface part. With decreasing temperature, the spins in the ferromagnetic part order ferromagnetically, while the spins in the spin glass part are weakly magnetized under the influence of the ferromagnetic order in the ferromagnetic part. As the temperature is decreased further, the spins in the spin glass part freeze in cooperation with all other spins in the system through the interface between ferromagnetic and spin glass parts.

2.4 Conclusions

Thin films of mEuO-TiO_2 (m=1, 2, 4) were deposited on silica glass substrate by the PLD method and their structural and magnetic properties were investigated. The resultant thin films were confirmed to be amorphous by XRD pattern, HRTEM image, and SAED pattern. The valence state of Eu in the thin films was studied by ^{151}Eu CEM spectra. EXAFS analysis indicates that the Eu^{2+} ions in EuO-TiO_2 and 2EuO-TiO_2 have local environment similar to those in EuO and the values of n_{Eu2+} and $d_{Eu\text{-}O}$ decrease with the increase of m in mEuO-TiO_2 (m=1, 2, 4). All the thin films have positive θ and undergo a reentrant spin glass transition after a ferromagnetic transition. The magnetic mechanism in the present thin films was discussed in terms of their structures.

References

1. T. Mizoguchi, N. Ueda, K. Yamauchi, and H. Miyajima, *J. Phys. Soc. Jpn.* **34**, 1691 (1973).
2. K. Yamada, Y. Ishikawa, Y. Endoh, and T. Masumoto, *Solid State Commun*. **16**, 1335 (1975).
3. L. J. Schowalter, M. B. Salamon, C. C. Tsuei, and R. A. Craven, *Solid State Commun*. **24**, 525 (1977).
4. X. Ze, Y. Ishikawa, S. Ishio, and M. Takahashi, *J. Phys. F: Met. Phys.* **15**, 1787 (1985).
5. J. L. Shaw, A. C. Wright, R. N. Sinclair, G. K. Marasinghe, D. Holland, M. R. Lees, and C. R. Scales, *J. Non-Cryst. Solids* **345**, 245 (2004).
6. K. Tanaka, H. Akamatsu, S. Nakashima, and K. Fujita, *J. Non-Cryst. Solids* **354**, 1346 (2008).
7. H. Akamatsu, K. Tanaka, K. Fujita, and S. Murai, *J. Phys. C*: *Condensed Matter* **20**, 235216 (2008).
8. J. Shoenes, E. Kaldis, W. Thöni, and P. Wachter, *Phys. Stat.Sol.* **51**, 173 (1979).
9. H. Akamatsu, K. Fujita, S. Murai, and K. Tanaka, *Phys. Rev. B* **81**, 014423 (2010).
10. I. Felner and I. Nowik, *Solid State Commum*. 28, 67 (1978).
11. B. Ravel and M. Newville, *J. Synchrotron Radiat.* **12**, 537 (2005).
12. J. J. Rehr and R.C. Albers, *Rev. Mod. Phys.* **72**, 621 (2000).
13. F. Grandjean and G. J. Long, *Mössbauer Spectroscopy Applied to Inorganic Chemistry* (Plenum Press, New York, 1989), pp. 513-97.
14. J. M. D. Coey, A. McEvoy, and M. W. Shafer, *J. Non-Cryst. Solids* **43**, 387 (1981).

15. G. K. Shenoy and B. D. Dunlap, *Nucl. Instrum. Methods* **71**, 285 (1969).
16. C. L. Chien, S. DeBenedetti, and F. De Barros, *Phys. Rev. B* **10**, 3913 (1974).
17. S. W. Marshall, J. A. Nelson, and R. L. Wilenzick, *Commun. ACM* **8**, 313 (1965).
18. K. Fujita, K. Tanaka, K. Hirao, and N. Soga, *J. Am. Ceram. Soc.* **81**, 1845 (1998).
19. K. Tanaka, K. Fujita, N. Matsuoka, K. Hirao, and N. Soga, *J. Mater. Res.* **13**, 1989 (1998).
20. S. Blonkowski, E. Defay, and X. Biquard, *Phys. Rev. B* **79**, 104108 (2009).
21. L. A. Grunes, *Phys. Rev. B* **27**, 2111 (1983).
22. F. Farges. G. E. Brown, and J. J. Rehr, *Phys. Rev. B* **56**, 1809 (1997).
23. S. Sakka, H. Kozuka, K. Fukuni, and F. Miyaji, *J. Non-Cryst. Solids* **123**, 176 (1990).
24. W. H. Zachariasen, *J. Am. Chem. Soc.* **54**, 3841 (1932).
25. Y, M. Kim and P. J. Bray, *J. Chem. Phys.* **53**, 716 (1970).
26. J. Zarzycki, *J. Mater. Sci.* **6**, 130 (1971).
27. K. K. Wu and I. D. Brown, *Acta Cryst.*. **B29**, 2009 (1973).
28. W. Schartau and R. Hoppe, *Z. Anorg. Allg. Chem.* **408**, 60 (1974).
29. M. Eibschutz and M. E. Lines, *Hyperfine Interactions* **27**, 47 (1986).
30. J. A. Mydosh, *Spin Glasses: An Experimental Introduction* (Taylor & Francis, London, 1993).
31. K. Jonason, J. Mattsson, and P. Nordblad, *Phys. Rev. B* **53**, 6507 (1996).
32. K. Binder and A. P. Young, *Rev. Mod. Phys.* **49** 435 (1977).
33. M. D. Mukadam, S. M. Yusuf, P. Sharma, S. K. Kulshreshtha, and G. K. Dey, *Phys. Rev. B* **72**, 174408 (2005).
34. G. Aeppli, S. M. Shapiro, R. J. Birgeneau, and H. S. Chen, *Phys. Rev. B* **25**, 4882

(1982).

35. H. Maletta, G. Aeppli, and S. M. Shapiro, *Phys. Rev. Lett.* **48**, 1490 (1982).
36. G. Aeppli, S. M. Shapiro, R. J. Birgeneau, and H. S. Chen, *Phys. Rev. B* **28**, 5160 (1983).
37. S. Niidera and F. Matsubara, *Phys. Rev. B* **75**, 144413 (2007).

Chapter 3 Structural and magnetic properties of bulk polycrystalline $EuZrO_3$ and amorphous europium zirconate thin films

3.1 Structural and magnetic properties of bulk polycrystalline $EuZrO_3$

3.1.1 Introduction

Eu^{2+}-bearing perovskite oxides, $EuM^{4+}O_3$ (e.g. M = Ti, Nb), have been studied in the last several decades for their intriguing magnetic and electrical properties [1-7]. A variety of magnetic and electrical properties have been observed, depending on the kind of M cations, oxygen non-stoichiometry, and aliovalent cationic substitution. For instance, europium niobate ($EuNbO_3$) behaves like a ferromagnetic metal [1,2], while the introduction of oxygen vacancies converts it into a superconductor with a critical temperature of about 6 K [3]. On the other hand, $EuTiO_3$ is an antiferromagnetic insulator with quantum paraelectric properties as mentioned above [4-7]. Compared to $EuNbO_3$ and $EuTiO_3$, the structure and physical properties of $EuZrO_3$ have been less investigated. Shafer [8] first prepared $EuZrO_3$ by a high-temperature solid-state reaction using ZrO_2 and EuO as starting materials and ascribed its crystal structure to a cubic perovskite. Recently, Viallet *et al*. [9] performed XRD pattern refinement on $EuZrO_3$ prepared by the same procedure in Ref. 8 and showed that it crystallizes in orthorhombic symmetry at room temperature. Namely, the previous reports on the crystal structure of $EuZrO_3$ are quite controversial. In addition, the magnetic ordering of $EuZrO_3$ has not been observed down to 4 K [8,9], which was the lowest measurement temperature ever reported. Therefore, further investigation is necessary to clarify both the crystal structure and magnetism of $EuZrO_3$.

In this study, we have synthesized bulk polycrystalline $EuZrO_3$ following the method described in Refs. 8 and 9, and examined its crystal structure and magnetic properties. Almost all europium ions are present as the divalent state in the synthesized $EuZrO_3$, as revealed by ^{151}Eu Mössbauer spectroscopy. The crystal structure is refined to an orthorhombic perovskite-type structure (*Pbnm* space group) through Rietveld analysis of the XRD pattern. In contrast to previous reports, measurements of magnetic susceptibility down to 2 K demonstrate that orthorhombic perovskite $EuZrO_3$ behaves as an antiferromagnet below about 4.1 K. This is the first observation of magnetic ordering in $EuZrO_3$.

3.1.2 Experimental

Polycrystalline $EuZrO_3$ was prepared from powders of EuO and ZrO_2 following the reaction described by the formula, $EuO + ZrO_2 = EuZrO_3$. Firstly EuO powder was prepared using the method described in Chapter 2. The obtained EuO was then thoroughly mixed with reagent-grade ZrO_2. After that the mixture was pressed into a pellet and sintered at 1550 ºC for 10 h in an Ar(95)/H_2(5) (vol%) atmosphere.

Powder XRD patterns were recorded on a Rigaku Rint 2500 X–ray diffractometer with Cu *Kα* radiation. Rietveld analysis was performed by a least-square method using the GSAS refinement program [10,11,12]. The lattice constants, atomic coordinates, occupation factors, and isotropic thermal parameters were refined freely for all atoms. Crystal structure of $EuZrO_3$ was drawn with the refined parameters using the VESTA software [13]. ^{151}Eu Mössbauer effect measurements were performed in a standard transmission geometry at room temperature to evaluate the valence state of europium ions and the local environment around Eu^{2+} ions. The γ-ray source is same with the

CEM measurements and the velocity calibration was done with the same method described in Chapter 2. Magnetic susceptibilities were carried out with a SQUID magnetometer (Quantum Design MPMS-XL) in a temperature range of 2-300 K under both ZFC and FC conditions at an external magnetic field of 50 Oe. The field dependence of magnetization was recorded at 2 K under magnetic fields up to 5 T.

3.1.3 Results and discussion

3.1.3.1 Crystal structure

Figure 3.1 shows the XRD pattern of the polycrystalline $EuZrO_3$ sample at room temperature (open circles). All the diffraction peaks can be indexed as an orthorhombic perovskite phase (*Pbnm* space group), which is consistent with the result reported by Viallet *et al.* [9] but not with that by Shafer [8]. Utilizing the orthorhombic structure of $SrZrO_3$ as a starting model, Rietveld refinement was performed, yielding an overall good agreement between the observed and calculated diffraction profiles (solid line). The final refinement converged to R_{wp} = 7.8%, R_p = 5.2%, and χ^2 = 1.92. The R_p factor is much smaller than that in Ref. 9 (11.9%). Some structural parameters deduced from the Rietveld refinement are summarized in Tables 1 and 2. The refined lattice constants, a = 5.79469(9), b = 5.82521(7), and c = 8.19799(14) Å, are close to those reported in Ref. 9. A view of the crystal structure of $EuZrO_3$ is illustrated in Fig. 3.2(a). The structure shows a $GdFeO_3$-type distortion through the rotation of ZrO_6 octahedra, due to the smaller size of Eu^{2+} ion compared to the cubo-octahedral interstice formed by the corner-sharing ZrO_6 network. The rotating angles in *a-b* plane (Φ) and normal to *a-b* plane (Θ) are estimated to be 6.2° and 12.7°, respectively, as shown in Figs. 3.2(b) and (c). The degree of the structure

distortion of ABO_3-type perovskites can be evaluated by the tolerance factor, $t = < A-O > / \sqrt{2} < B-O >$, where <*A*-O> and <*B*-O> represent the mean cation-oxygen interatomic distances of *A* and *B* sites, respectively [14]. Geometrically, *t* equals to 1 for an ideal (cubic) perovskite. For $EuZrO_3$ where Eu^{2+} and Zr^{4+} ions occupy the *A*- and *B*-sites, respectively, *t* is estimated to be 0.983, which again suggests a certain distortion from ideal perovskite structure.

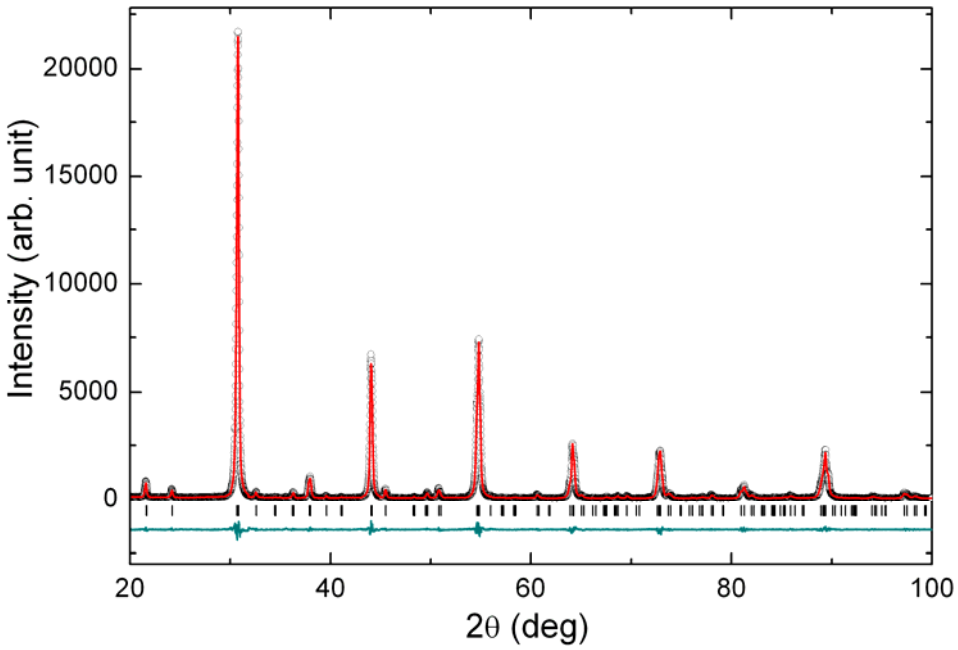

Fig. 3.1: Powder XRD pattern of $EuZrO_3$ synthesized by the solid-state reaction between EuO and ZrO_2 (open circles) and the profile calculated by the Rietveld refinement (line). Vertical ticks indicate the expected reflection positions for the orthorhombic $EuZrO_3$. The bottom curve is the difference between experimental and calculated profiles.

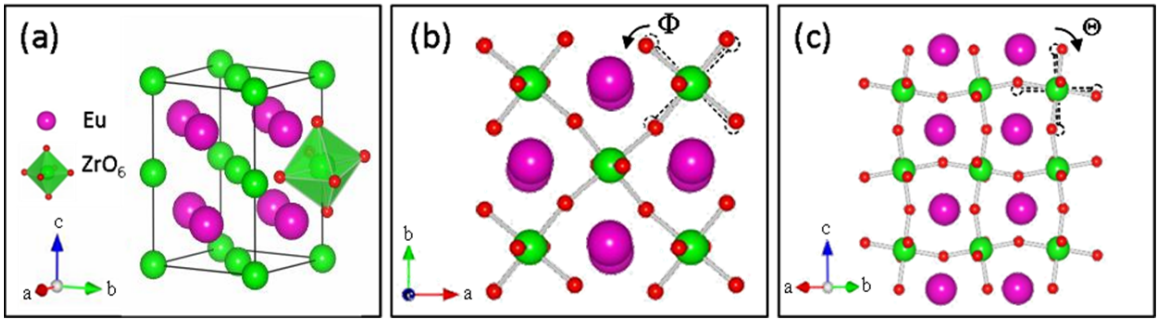

Fig. 3.2: (a) Crystal structure of $EuZrO_3$ drawn based on Rietveld refinement results. (b) and (c) illustrate the structure of $EuZrO_3$ projected along the [001] and [110] directions, respectively. The dashed lines indicate the corresponding positions of ZrO_6 octahedra in the ideal perovskite structure.

Table 1: Atomic coordination, site occupancy, and isotropic thermal factors (*U*iso) for orthorhombic $EuZrO_3$.

	x	***y***	***z***	**Ocuppancy**	***U*iso (Å^2)**
Eu	0.00557(25)	0.52478(8)	0.25	0.988(1)	0.0183(2)
Zr	0	0	0	0.971(2)	0.0136(3)
O1	-0.0789(19)	-0.0115(9)	0.25	1.029(24)	0.0189(48)
O2	0.2171(13)	0.2798(11)	0.0458(11)	0.981(18)	0.0238(35)

Lattice constants (*Pbnm*): a = 5.79469(9), b = 5.82521(7), and c = 8.19799(14) Å.
Weighted profile R_{wp} = 7.8%, profile R_p = 5.2%, and reduced χ^2 = 1.92.

Table 2: Selected distances (Å) in $EuZrO_3$.

NN Eu-Eu (×2)	4.1540(21)	NN Eu-O1	2.482(11)	NN Zr-O1 (×2)	2.100(2)
NN Eu-Eu (×2)	4.0630(20)	NN Eu-O1	2.745(5)	NN Zr-O2 (×2)	2.093(7)
NN Eu-Eu (×2)	4.10966(11)	NN Eu-O1	3.162(5)	NN Zr-O2 (×2)	2.115(7)
Mean NN <Eu-Eu>	4.1089	NN Eu-O1	3.329(12)	Mean NN <Zr-O>	2.103
NNN Eu-Eu (×2)	5.7950(20)	NN Eu-O2 (×2)	2.518(7)		
NNN Eu-Eu (×2)	5.8252(7)	NN Eu-O2 (×2)	2.755(8)		
NNN Eu-Eu (×4)	5.6640(11)	NN Eu-O2 (×2)	2.974(9)		
NNN Eu-Eu (×4)	5.9535(11)	NN Eu-O2 (×2)	3.438(8)		
Mean NNN <Eu-Eu>	5.8092	Mean NN <Eu-O>	2.924		

3.1.3.2 ^{151}Eu Mössbauer spectroscopy

Figure 3.3 shows the room-temperature ^{151}Eu Mössbauer spectrum of $EuZrO_3$. Two peaks are observed around -13 and 0.5 mm/s, assigned to Eu^{2+} and Eu^{3+} absorption, respectively. The fraction of Eu^{2+} relative to the total europium ions was estimated to be about 0.96 from the area ratio of the two absorption peaks, which is comparable to those in $EuZrO_3$ and $EuTiO_3$ as reported previously [5,8]. The Eu^{2+} absorption peak in Fig. 3.3 is asymmetrically broadened with a shoulder around -11.5 mm/s, suggesting the presence of electric quadrupole interaction between the electric field gradient and the electric quadrupole moment of ^{151}Eu nucleus. Since the analysis of asymmetric Mössbauer spectrum using a single Lorentzian gives rise to a significant error in isomer shift value [15], we have utilized the method developed by Shenoy and Dunlap as described in Chapter 2 [16]. During the calculation 12 possible transitions with a Lorentzian line shape were taken into account, and the magnetic hyperfine interaction was ignored because $EuZrO_3$ is paramagnetic at room temperature as described below. The fit of the theoretical curve to the Eu^{2+} absorption peak yields δ = -12.64±0.02 mm/s, $eV_{zz}Q_g$ = -10.32±0.21 mm/s, γ = 2.65±0.05 mm/s, and η = 0.46±0.05. The δ value of $EuZrO_3$ is very close to that of cubic perovskite $EuTiO_3$ (-12.5±0.1 mm/s) but slightly different from that of $EuZrO_3$ (-13.1±0.2 mm/s) reported by Berkooz [17] (Note that the values of δ reported in Ref. 17, which were relative to Eu_2O_3, are converted to those referred to EuF_3 by adding 1.037 mm/s to the original values). It is most probable that the difference in δ between the present $EuZrO_3$ and the one reported previously stems from the fact that the contribution of quadrupole interactions is taken into account in the present analysis; otherwise, the δ value is equal to the datum derived by Berkooz,

corresponding exactly to the peak position of the Eu^{2+} absorption (see Fig. 3). Based on the above analyses of XRD pattern and Mössbauer spectrum, we believe that the δ value (-12.64 mm/s) obtained in this work is more reliable. On the other hand, since the quadrupole interaction for Eu^{2+} -containing compounds mainly reflects the electric field gradient caused by the surrounding ligands due to the small anisotropy of 4*f* electrons [18], the non-zero quadrupole interaction ($eV_{zz}Q_g$ = -10.32 mm/s) and non-zero asymmetry parameter (η = 0.46) indicate the presence of non-axial electric field gradients at Eu^{2+} sites, consistent with the orthorhombic structure of $EuZrO_3$ where the Eu^{2+} sites have the point symmetry $m(C_{1h})$. The value of γ is almost the same to the FWHM of absorption peak obtained for cubic EuS (2.5 mm/s), ensuring the occupation of single crystallographically equivalent sites by Eu^{2+} ions.

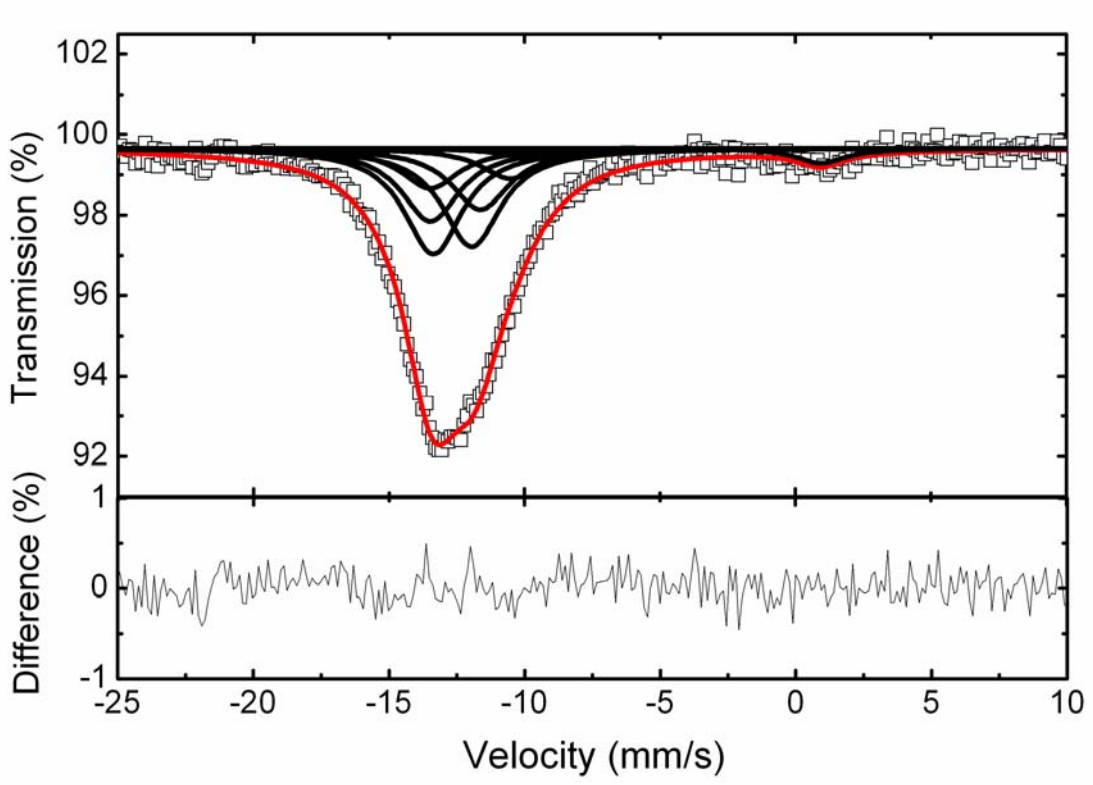

Fig. 3.3: Room-temperature Mössbauer spectrum of $EuZrO_3$ (open squares). The solid line represents the theoretical spectrum calculated by Eqs. (2.1)-(2.3) in which the presence of quadrupole interaction is considered. The component lines of the 12 transitions (solid black lines) are also shown for the Eu^{2+} absorption peak at around -12 mm/s. The Eu^{3+} absorption peak at around 0.5 mm/s is simply analyzed by a single Lorenzian because of the poor shape resolution. The bottom curve is the difference between experimental and calculated profiles.

3.1.3.3 Magnetic properties

Figure 3.4(a) illustrates the magnetic susceptibility (χ) as a function of temperature (T) measured for $EuZrO_3$ under the external magnetic field of 50 Oe. A kink structure corresponding to a magnetic transition is observed at 4.1 K without any divergence between ZFC and FC magnetic susceptibilities. The magnetization (M) as a function of external magnetic field (H) at 2 K is shown in Fig. 3.4(b). Since the Eu^{2+} ion has an $S = 7/2$ spin with a Heisenberg character and least magnetic anisotropy, the Eu^{2+} spins are first flipped and then gradually changed into FM arrangement with increasing H. The magnitude of M tends to be saturated at higher H than 3 T. The saturation magnetization is 6.87 μ_B, which is very close to the theoretical spin-only magnetic moment of Eu^{2+} (7 μ_B). This result, together with the presence of kink structure in the χ-T curve, indicates the antiferromagnetic order at the ground state.

We have analyzed the χ-T curve in the high-temperature region by considering the contribution arising from both Eu^{2+} and impurity Eu^{3+} ions:

$$\chi_{\text{mol}} = c\chi_{\text{mol}}(\text{Eu}^{2+}) + (1-c)\chi_{\text{mol}}(\text{Eu}^{3+}) + \chi_0, \tag{3.1}$$

where c is the molar ratio of Eu^{2+} to the total europium ions, and χ_0 is the temperature-independent term. The magnetic susceptibility of Eu^{2+}, $\chi_{\text{mol}}(Eu^{2+})$, can be calculated by the Curie-Weiss law as represented by Eq. 2.4. The ground state $^7F_0$ of Eu^{3+} is nonmagnetic, and the excited states ^7F_J (J = 1, 2, ..., 6) are so close to the ground state that the energy differences are comparable to kT at room temperature. In consideration of the first three excited states, the magnetic susceptibility of Eu^{3+}, $\chi_{\text{mol}}(Eu^{3+})$, can be written as [19]

$$\chi_{\text{mol}}(\text{Eu}^{3+}) = \frac{N_A\mu_B^2}{3kT} \times \frac{24/a + (13.5-1.5/a)e^{-a} + (67.5-2.5/a)e^{-3a} + (189-3.5/a)e^{-6a}}{1+3e^{-a}+5e^{-3a}+7e^{-6a}}, \tag{3.2}$$

where $a = \lambda/kT$ is the ratio of the multiplet width (λ is the spin-orbit coupling constant) to the thermal energy. If we take $\lambda = 370$ cm^{-1} as reported for $EuAlO_3$ [20] and $\mu_{eff} = 7.94\ \mu_B$ as obtained theoretically, the experimental susceptibility can be well reproduced with Eqs. (3.1), (3.2), and (2.4) (see the solid line in Fig. 3.4(a)), yielding $c = 0.97$ and $\theta = +0.07$ K. The value of c is very close to that obtained from the Mössbauer measurement. The positive θ value implies the predominance of ferromagnetic interactions between localized Eu^{2+} spins in $EuZrO_3$.

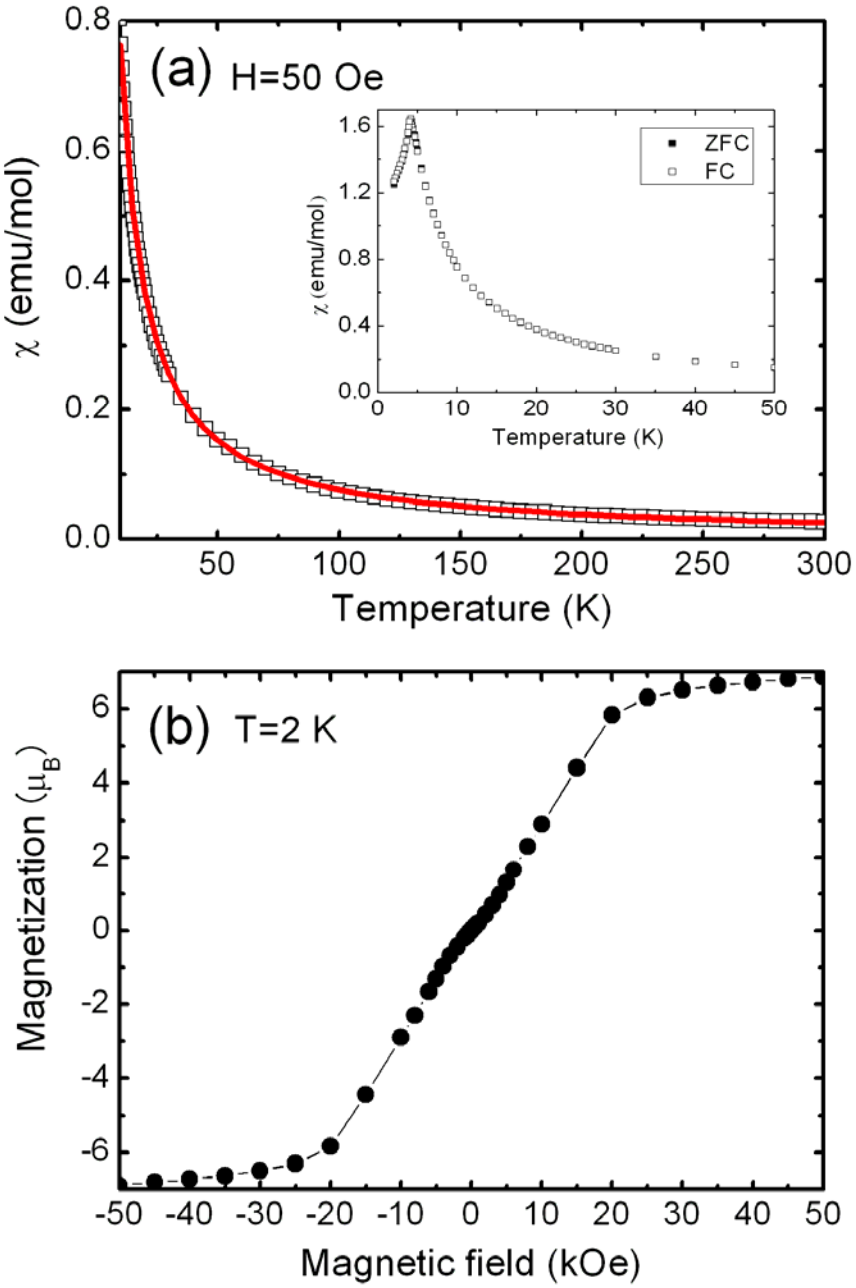

Fig. 3.4: (a) Temperature dependence of magnetic susceptibility of $EuZrO_3$ (open squares) measured in a magnetic field (H) of 50 Oe. The solid line represents the theoretical curve. The inset shows both FC (open squares) and ZFC (closed squares) curves in the low temperature region. (b) Field dependence of magnetization of $EuZrO_3$ (closed circles) measured at 2 K. The solid line is a guide for the eye.

In the final part, we will address the mechanism responsible for the observed antiferromagnetic ordering in $EuZrO_3$. In Eu^{2+}-containing crystalline oxides with perovskite-type structure, the magnetic structure is predominantly determined by the NN and NNN exchange interactions between Eu^{2+} ions [4-6,21-23]. For antiferromagnetic perovskites where magnetic ions are located on a simple cubic lattice, there exist three types of antiferromagnetic ordering, namely, *A*-, *C*-, or *G*- type (see Fig. 3.5), and the values of J_1 and J_2 can be derived from the following equations using the molecular-field approximation [23],

$$\theta = \frac{2S(S+1)}{3k}(6J_1 + 12J_2), \tag{3.3}$$

$$T_{N1} = \frac{2S(S+1)}{3k}(2J_1 - 4J_2), \tag{3.4}$$

$$T_{N2} = \frac{2S(S+1)}{3k}(2J_1 + 4J_2), \tag{3.5}$$

$$T_{N3} = \frac{2S(S+1)}{3k}(-6J_1 + 12J_2), \tag{3.6}$$

where T_{N1}, T_{N2}, and T_{N3} are the Néel temperatures for *A*-, *C*-, and *G*-type antiferromagnetic ordering, respectively. In pseudocubic perovskite $EuZrO_3$, Eu^{2+} ions locate on an approximately cubic lattice. Disregarding the structure distortion and setting S = 7/2, one obtains J_1/k = +0.033 K and J_2/k = -0.031 K for an *A*-type antiferromagnetic structure using Eqs. (3.3) and (3.4), while the analysis on a *G*-type antiferromagnetic structure using Eqs. (3.3) and (3.6) yields J_1/k = -0.032 K and J_2/k = +0.017 K. There is no solution by combining Eq. (3.3) with Eq. (3.5), so the possibility of the *C*-type antiferromagnetic ordering can be ruled out for $EuZrO_3$. Although we do not have further experimental evidence to distinguish the *A*-type antiferromagnetic structure from the *G*-type one for $EuZrO_3$ at this moment, previous analysis of magnetic structure for a series of Eu^{2+} -containing perovskite oxides may

allow us to deduce the magnetic structure of $EuZrO_3$. In cubic perovskite $EuTiO_3$, the values of J_1/k and J_2/k are evaluated to be -0.014 K and = +0.037 K, respectively. Greedan *et al.* [23] applied the molecular-filed approximation to cubic perovskite $EuMg_{0.5}W_{0.5}O_3$ and $EuLu_{0.5}Ta_{0.5}O_3$, and compared their J_1 and J_2 values with those obtained for $EuTiO_3$. They found that the J_1 and J_2 values vary systematically with the NN and NNN Eu^{2+} distances, respectively, if a *G*-type antiferromagnetic ordering is assumed for $EuMg_{0.5}W_{0.5}O_3$ and $EuLu_{0.5}Ta_{0.5}O_3$. Namely, the value of J_1/k decreases from –0.014 K ($EuTiO_3$) to –0.095 K ($EuLu_{0.5}Ta_{0.5}O_3$) with increasing the NN Eu^{2+} distance from 3.904 to 4.100 Å, while the value of J_2/k decreases from +0.037 K ($EuTiO_3$) to –0.016 K ($EuLu_{0.5}Ta_{0.5}O_3$) as the NNN Eu^{2+} distance increases from 5.52 to 5.80 Å. Considering the fact that the mean NN and NNN Eu^{2+} distances in $EuZrO_3$ are 4.1089 and 5.8092 Å, respectively (see Table 2), the systematic variations of J_1 and J_2 values with NN and NNN Eu^{2+} distances are more compatible for the *G*-type antiferromagnetic structure than for the *A*-type one. Here, it should be noted that there exist differences in the J_1 and J_2 values for the *G*-type antiferromagnetic ordering between $EuLu_{0.5}Ta_{0.5}O_3$ and $EuZrO_3$ despite their similar NN and NNN Eu^{2+} distances. This may be caused by the neglect of the structural distortion in $EuZrO_3$ involving the distribution of Eu-O-Eu bond angles during the above calculation. Also, it is anticipated for orthorhombic perovskite $EuZrO_3$ with *A* sites occupied by magnetic ions that the presence of single-ion anisotropy and magnetic dipole-dipole interactions may lead to spin canting; however, the degree of spin canting should be considerably small in $EuZrO_3$ since Eu^{2+} is an *S*-state ion, which is similar to the case in orthorhombic perovskite $GdAlO_3$ where Gd^{3+} ions are in the same *S* ground state [24]. Further studies are required to clarify the magnetic structure in $EuZrO_3$.

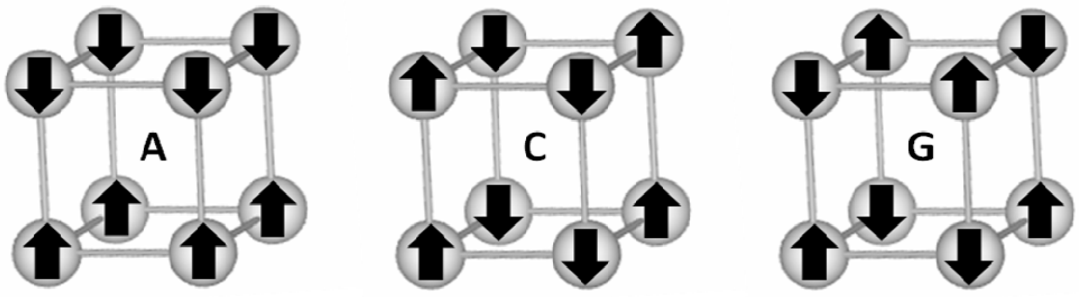

Fig. 3.5: Schematic depiction of the *A*-, *C*-, and *G*- type AFM structures. The arrows represent spin orientation in a cubic lattice.

3.1.4 Conclusion

In summary, perovskite $EuZrO_3$ was synthesized through a high temperature solid-state reactionand its structural and magnetic properties were examined. Through the Rietveld analysis of XRD data the crystal structure of $EuZrO_3$ was refined to orthorhombic perovskite (*Pbnm* space group) with lattice constants a = 5.79469(9), b = 5.82521(7), and c = 8.19799(14) Å. The analysis of ^{151}Eu Mössbauer spectrum indicates that almost all the europium ions are present as Eu^{2+} and occupy the distorted sites with non-axial electric field gradients. An antiferromagnetic behavior of $EuZrO_3$ is observed below T_N~4.1 K with a positive θ of 0.07 K. The possible mechanism of the magnetic transition has been discussed.

3.2 Magnetic properties of amorphous europium zirconate thin films

3.2.1 Introduction

The ferromagnetism discovered in amorphous europium titanate thin films is quite unique in comparison with most insulating amorphous magnets which usually show spin glass behaviors. To further confirm the ferromagnetic nature in such systems, it is necessary to extend the study to other amorphous Eu^{2+}-containing systems. The results mentioned above demonstrate that crystalline $EuZrO_3$ has similar magnetic structure to crystalline $EuTiO_3$, that is, a G-type antiferromagnetic structure with dominant ferromagnetic interactions. Therefore a small structural perturbation is expected to result in a large variation of the magnetic properties in $EuZrO_3$. This makes amorphous europium zirconates good candidates for the study of the magnetism of amorphous Eu^{2+}-containing systems.

In this study, amorphous zirconate thin films with nominal composition of $EuO\text{-}ZrO_2$ and $4EuO\text{-}ZrO_2$ have been prepared by the PLD method and their structural and magnetic properties have been examined. Both $EuO\text{-}ZrO_2$ and $4EuO\text{-}ZrO_2$ exhibit ferromagnetic transitions with reentrant spin glass transitions. The value of T_C in $4EuO\text{-}ZrO_2$ was estimated to be about 22 K, which is the highest value among Eu^{2+}-containing amorphous insulating materials.

3.2.2 Experimental

Thin films of $EuO\text{-}ZrO_2$ and $4EuO\text{-}ZrO_2$ were prepared by a PLD method via the same experimental procedure to that for the preparation of amorphous europium titanate thin films. The laser energy and frequency were set as 180 mJ and 10 Hz, respectively.

The thin films were deposited on silica glass substrates at room temperature under the base pressure of 10^{-6} Pa. The target for the deposition of EuO-ZrO_2 was the polycrystalline $EuZrO_3$ pellet described above, while that for the deposition of 4EuO-ZrO_2 was prepared from EuO and ZrO_2 powders with a mole ratio of 4:1 under an Ar(95)/H_2(5) (vol%) atmosphere. The thickness of the thin films examined by a surface profiler (Alpha-Step IQ, KLA-Tencor) was about 160 nm. RBS measurements indicate that the molar ratio of Eu to Zr in the thin film were 0.95:1 and 3.45:1 for EuO-ZrO_2 and 4EuO-ZrO_2, respectively (see Fig. 3.6). The structure of the thin films was characterized by XRD (Rint2500, Rigaku) with Cu *Kα* radiation and HRTEM observations (JEM-2100F, JEOL). The valence state of Eu ions was examined by ^{151}Eu CEM measurements using the same procedures as described in Chapter 2. The magnetization of the thin films was recorded on a SQUID magnetometer (Quantum Design MPMS-XL). The DC magnetic susceptibilities were measured under ZFC and FC modes at DC magnetic fields of 20, 50 and 100 Oe in a temperature region of 2-300K and the magnetization as a function of magnetic fields were obtained at 2 K in a magnetic field region of −5~5 T. The AC magnetic measurements were carried out at an AC magnetic field of 3 Oe and DC magnetic fields of 0-5 Oe in a temperature region of 2-30 K with frequency varying from 0.1 to 300 Hz.

3.2.3 Results and discussion

The XRD patterns of EuO-ZrO_2 and 4EuO-ZrO_2 are shown in Fig. 3.7 (a), which indicate that no crystalline structure exists in the thin films. The amorphous nature of the thin films was also confirmed by HRTEM measurements. The HRTEM image and the SAED pattern of EuO-ZrO_2 are shown in Fig. 3.7 (b).

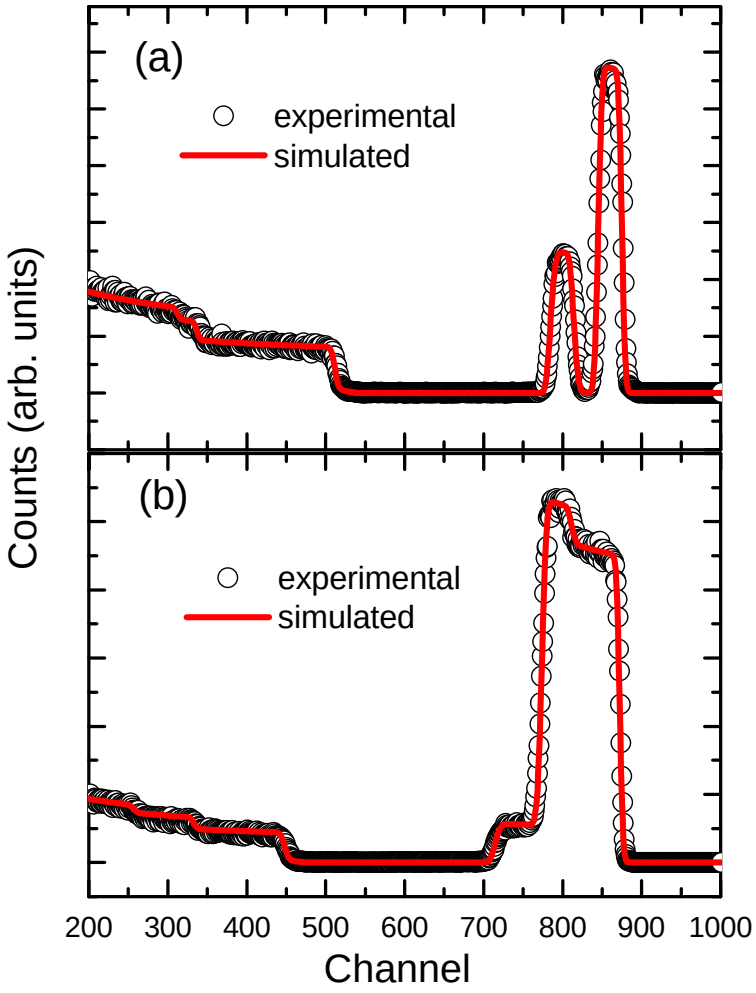

Fig. 3.6: Experimental (open circles) and the simulated (solid lines) RBS spectra of EuO-ZrO_2 (a) and 4EuO-ZrO_2 (b).

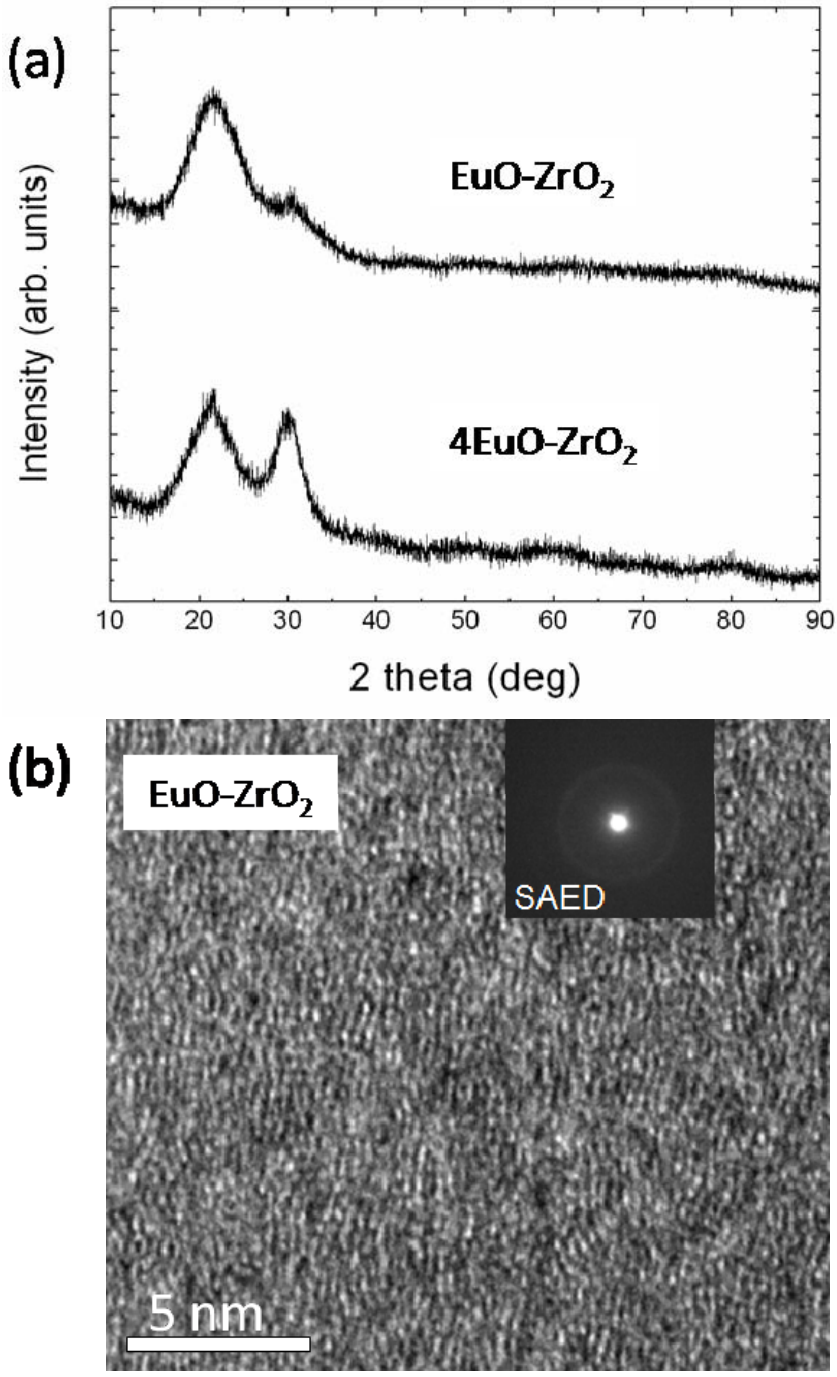

Fig. 3.7: (a) XRD patterns of $EuO\text{-}ZrO_2$ and $4EuO\text{-}ZrO_2$. (b) TEM image of $EuO\text{-}ZrO_2$. The inset shows SAED pattern of $EuO\text{-}ZrO_2$.

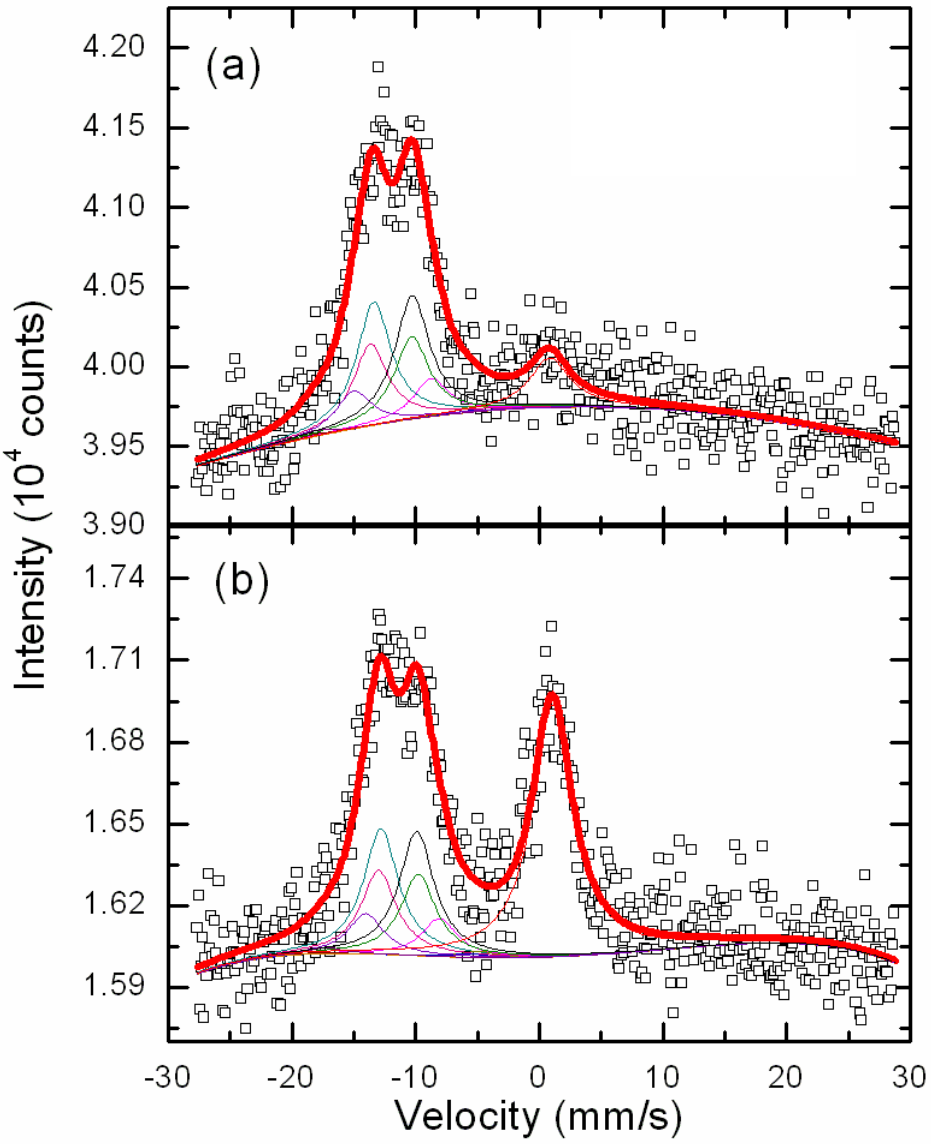

Fig. 3.8: ^{151}Eu CEM spectra measured at room temperature for EuO-ZrO_2 (a) and 4EuO-ZrO_2 (b). The open squares represent the experimental data, and the solid lines are the fit of theoretical curve using Eqs. (2.1)-(2.3). The component lines corresponding to the 12 transitions are shown for the Eu^{2+} absorption peak at around –12 mm/s.

Figure 3.8 shows the room-temperature CEM spectra of EuO-ZrO_2 and 4EuO-ZrO_2. Similar to those of amorphous europium titanate thin films, the spectra are composed of two peaks around –13 and 0.5 mm/s, corresponding to the absorptions due to Eu^{2+} and Eu^{3+}, respectively. The fractions of Eu^{2+} over total Eu estimated from the area ratio of the two absorptions are 96% and 63% for EuO-ZrO_2 and 4EuO-ZrO_2, respectively. Again, it should be mentioned that CEM measurement which preferentially probes the surface layer of the thin film may result in a relatively large deviation in the value for 4EuO-ZrO_2. The Eu^{2+} absorption bands show a hyperfine structure due to the presence of quadrupole interactions. Using the same method for analyzing the spectra of amorphous europium titanate thin films, the isomer shift (δ), quadrupole interaction parameter ($eV_{zz}Q_g$), FWHM of the absorption (γ), and asymmetry parameter of the electric gradient (η) were estimated and summarized in Table 3.3. The δ value for EuO-ZrO_2 is close to that for EuO-TiO_2, indicating similar coordination number of Eu^{2+} in both systems. In the same way, the coordination number of Eu^{2+} in 4EuO-ZrO_2 could be similar to that in 4EuO-TiO_2. The magnitudes of $eV_{zz}Q_g$ and η for EuO-ZrO_2 and 4EuO-ZrO_2 are slightly higher than those for amorphous europium titanate thin films, suggesting the distribution of electrons supplied by oxide ions around a Eu^{2+} ion is more asymmetrical in amorphous europium zirconate thin films than that in amorphous europium titanate thin films. The γ values for EuO-ZrO_2 and 4EuO-ZrO_2, which reflect the site-to-site variation or the distortion of the amorphous structure, are consistent with those for amorphous europium titanate thin films.

Table 3.3 Parameters obtained by the fit of the CEM spectra using Eqs. (2.1)-(2.3).

	δ (mm/s)	$eV_{zz}Q_g$ (mm/s)	η (mm/s)	γ (mm/s)
EuO-ZrO_2	-11.9	-18.3	1.0	3.4
4EuO-ZrO_2	-11.3	-18.0	0.86	3.4

Figures 3.9(a) and (b) depict the $M(T)$ curves of EuO-ZrO_2 and 4EuO-ZrO_2 measured under ZFC and FC conditions at different magnetic fields. The magnetic behaviors of EuO-ZrO_2 and 4EuO-ZrO_2 are very similar to those of amorphous europium titanate thin films. With decreasing temperature the $M(T)$ curves exhibit a sharp increase, which is a signature of ferromagnetic transition. The values of T_C were estimated to be 8 and 22 K for EuO-ZrO_2 and 4EuO-ZrO_2, respectively. The T_C value in 4EuO-ZrO_2 is higher than any other amorphous insulating Eu^{2+}-containing materials ever reported. With further decreasing temperature the $M(T)$ curves measured at magnetic fields of 20 and 50 Oe exhibit a discrepancy between those under ZFC and FC conditions, indicating a reentrant spin glass transition at lower temperatures. The $\chi^{-1}(T)$ curves of EuO-ZrO_2 and 4EuO-ZrO_2 are shown in Fig. 3.9(c), demonstrating a nearly linear behavior in the high temperature region. By fitting Eq. (2.4) to the high temperature region of $\chi^{-1}(T)$, the values of θ were obtained to be 11 and 26 K for EuO-ZrO_2 and 4EuO-ZrO_2, respectively. The positive θ values again suggest that ferromagnetic interactions are dominant in amorphous Eu^{2+}-containing oxides. The $M(H)$ curves of EuO-ZrO_2 and 4EuO-ZrO_2 (see Fig. 3.9(d)) show an abrupt increase with the increase of magnetic field and are almost saturated at 1 T, which are similar to those of amorphous europium titanate thin films.

The AC magnetizations of EuO-ZrO_2 and 4EuO-ZrO_2 were measured to further understand their magnetic properties. Figure 3.10 shows $M'(T)$ and $M''(T)$ curves of

the thin films measured at an AC field of 3 Oe with f varying from 0.1 to 300 Hz. The $M'(T)$ curve exhibits a sharp f-independent increase and a peak with peak position shifting to higher temperature upon increasing f. These behaviors are very alike the reentrant spin glass behavior observed in amorphous europium titanate thin films. Through Eq. (2.5) the f-dependent peak shift φ was evaluated to be about 0.01 for EuO-ZrO_2 and 4EuO-ZrO_2. This value is comparable to those in conventional spin glasses [25], suggesting that the peaks in $M'(T)$ curves are dominated by spin glass transitions. Further evidences for the reentrant spin glass transition in EuO-ZrO_2 and 4EuO-ZrO_2 can be obtained from the DC field superimposed AC measurements. Figure 3.11(a) gives the $M'(T)$ and $M''(T)$ curves of EuO-ZrO_2 measured at an AC field of 3 Oe with f of 10 Hz under different DC fields. The peaks in $M'(T)$ and $M''(T)$ curves are suppressed by applying DC field, and when the DC field reaches 5 Oe, a shoulder at T_C appears in higher temperature side of the $M'(T)$ curves. The shoulder position does not change while the main peak position shifts to higher temperature with varying f (see Fig. 3.11(b)), suggesting that both ferromagnetic and spin glass transitions occur in the thin films.

The magnetic mechanism in EuO-ZrO_2 and 4EuO-ZrO_2 is supposed to be similar to that in amorphous europium titanate thin films as discussed in Chapter 2. The slightly higher T_C and θ values in EuO-ZrO_2 and 4EuO-ZrO_2 compared to those in EuO-TiO_2 and 4EuO-TiO_2 are probably due to the difference in their structures resulting from the different ion radii of Zr^{4+} and Ti^{4+}. However, because of the absence of structural information for EuO-ZrO_2 and 4EuO-ZrO_2, a detailed explanation on this issue can not be given at this moment.

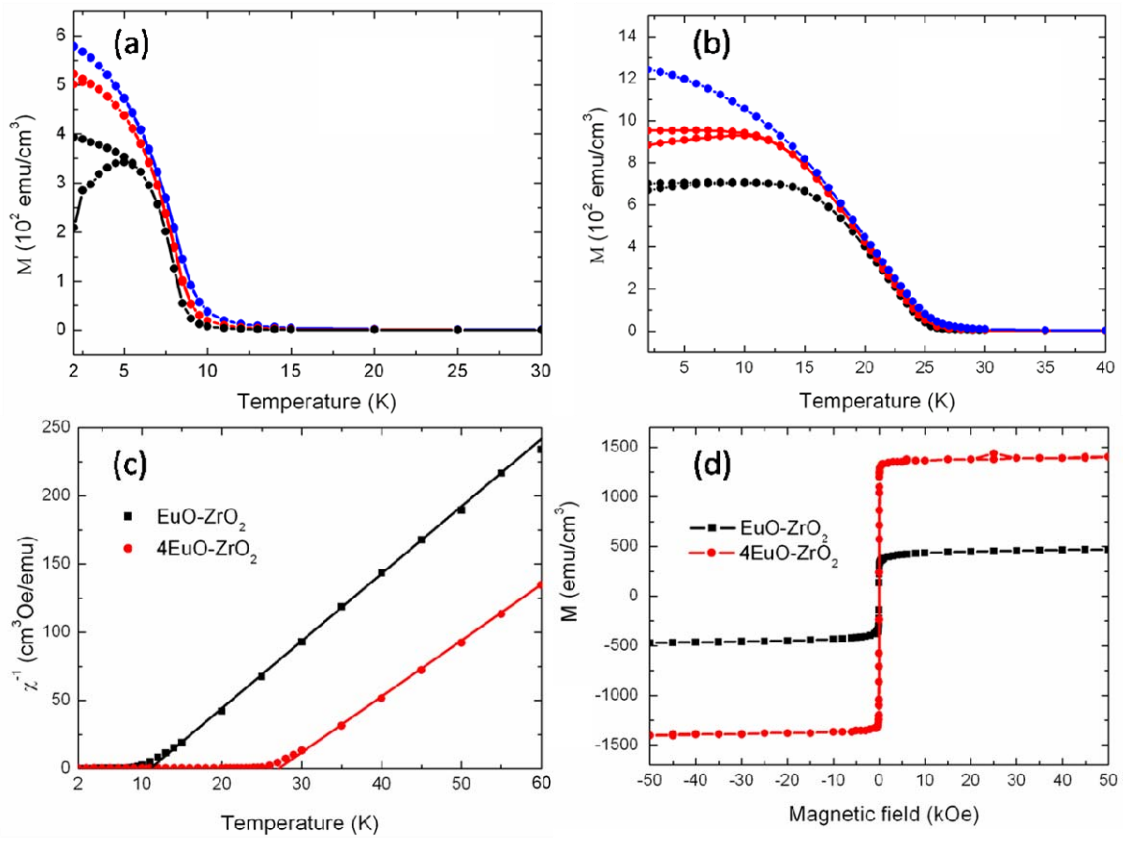

Fig. 3.9: $M(T)$ curves for EuO-ZrO_2 (a) and 4EuO-ZrO_2 (b) measured at magnetic fields of 20, 50 and 100 Oe (from up to down). (c) $\chi^{-1}(T)$ for EuO-ZrO_2 (solid squares) and EuO-ZrO_2 (solid circles) measured at magnetic field of 50 Oe as well as the fit of Curie-Weiss law to the experimental data (solid lines). (d) $M(H)$ of EuO-ZrO_2 and 4EuO-ZrO_2 measured at 2 K.

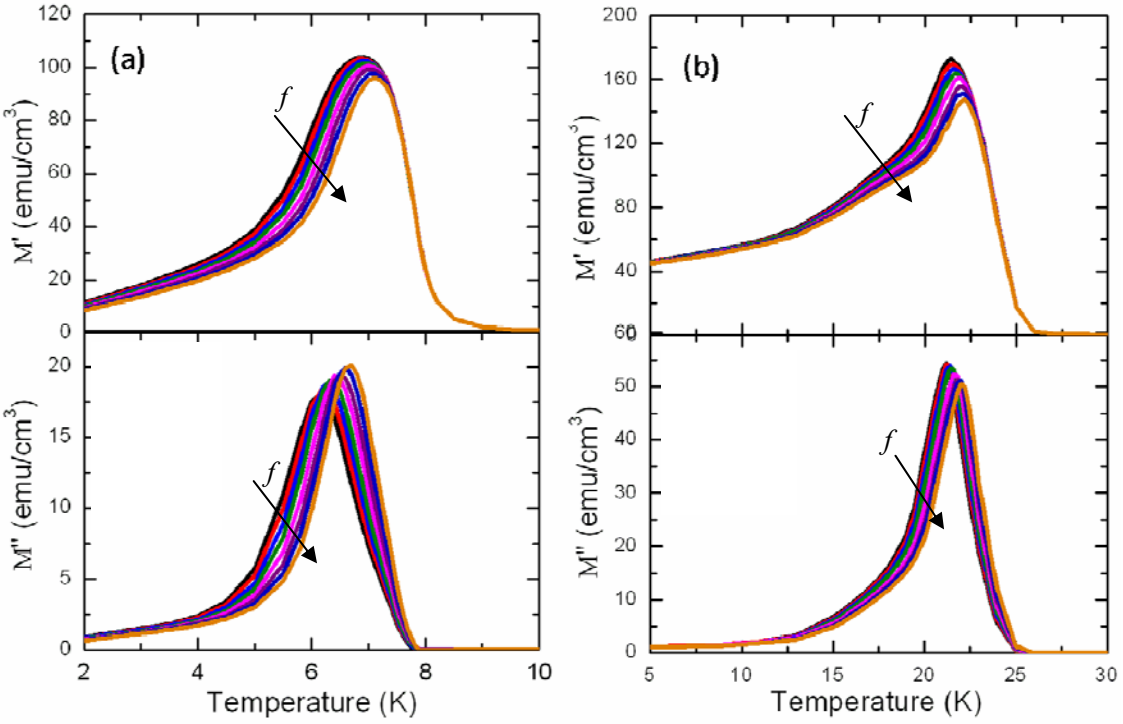

Fig. 3.10: $M'(T)$ and $M''(T)$ for EuO-ZrO_2 (a) and 4EuO-ZrO_2 (b) measured at AC field of 3 Oe with f of 0.1, 0.3, 1, 3, 10, 30, 100, and 300 Hz (from top to end).

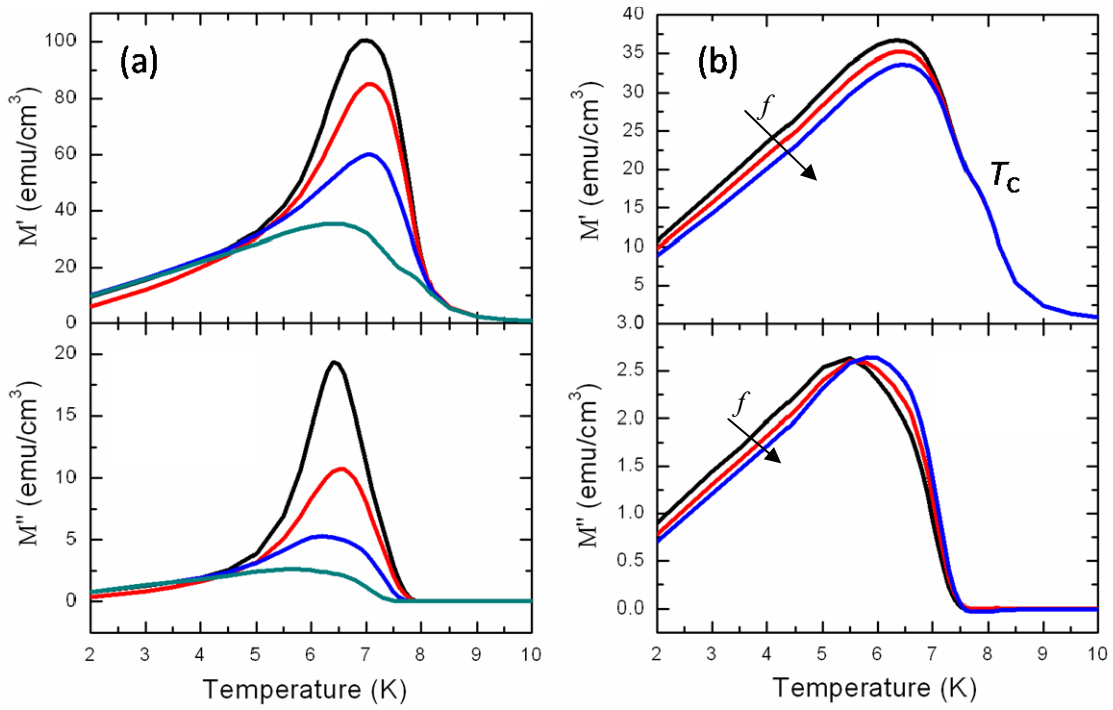

Fig. 3.11: (a) $M'(T)$ and $M''(T)$ for EuO-ZrO_2 measured at AC field of 3 Oe under superimposed DC fields of 0, 1, 2, and 5 Oe (from up to down). (b) $M'(T)$ and $M''(T)$ at an AC field of 3 Oe and a DC field of 5 Oe with f of 1, 10, and 100 Hz (from top to end).

3.2.4 Conclusions

Amorphous thin films of EuO-ZrO_2 and 4EuO-ZrO_2 have been prepared by a PLD method and their structural and magnetic properties have been investigated. Similar to amorphous europium titanate thin films, EuO-ZrO_2 and 4EuO-ZrO_2 exhibit ferromagnetic and reentrant spin glass transitions with positive θ. The observed ferromagnetic transitions confirm that ferromagnetism is intrinsic in such amorphous Eu^{2+}-containing oxides with high Eu^{2+} concentration.

References

1. V. G. Zubkov, A. P. Tyutyunnik, V. A. Pereliaev, G. P. Shveikin, J. Köhler, R. K. Kremer, A. Simon, and G. Svensson, *J. Alloys Compd.* **226**, 24 (1995).
2. K. Ishikawa, G. Adachia, and J. Shiokawa, *Mater. Res. Bull*. **16**, 419 (1981).
3. G. K. Strukova, D. V. Shovkun, V. N. Zverev, I. E. Batov, S. A. Zver'kov, and S. S. Khasanov, *Physica C* **351**, 363 (2001).
4. T. R. McGuire, M. W. Shafer, R. J. Joenk, H. A. Alperin, and S. J. Pickart, *J. Appl. Phys*. **37**, 981 (1966).
5. C. L. Chien, S. DeBenedetti, and F. De Barros, *Phys. Rev. B* 10, 3913 (1974).
6. R. Ranjan, H. S. Nabi, and R. Pentcheva, *J. Phys.: Condens. Matter* **19**, 406217 (2007).
7. T. Katsufuji and H. Takagi, *Phys. Rev. B* **64**, 054415 (2001).
8. A. H. Shafer, *J. Appl. Phys*. **36**, 1145 (1965).
9. V. Viallet, J. F. Marucco, J. Saint, M. Herbst-Ghysel, and N. Dragoe, *J. Alloys Compd*. **461**, 346 (2008).
10. H. M. Rietveld, *Acta Cryst*. **22**, 151 (1967).
11. A. C. Larson and R. B. Von Dreele, General Structure Analysis System(GSAS), *Los Alamos National Laboratory Report LAUR* 2000, 86-748
12. B. H. Toby, *J. Appl. Cryst*. **34**, 210 (2001).
13. K. Momma and F. Izumi, *J. Appl. Crystallogr*. **41**, 653 (2008).
14. S. Sasaki, C. T. Prewitt, and R. C. Liebermann, *Am. Mineral*. **68**, 1189 (1983).
15. B. A. Goodmen, N. N. Greenwood, and G. E. Turner, *Chem. Phys. Lett*. **5**, 181 (1970).

16. G. K. Shenoy and B. D. Dunlap, *Nucl. Instrum. Methods* **71**, 285 (1969).

17. O. Berkooz, *J. Phys. Chem. Solids* **30**, 1763 (1969).

18. F. Grandjean and G. J. Long, in: G. J. Long, F. Grandjean (Eds.), *Mössbauer Spectroscopy Applied to Inorganic Chemistry*, vol. 3, Plenum Press, New York, 1989, pp. 513-97.

19. J. H. Van Vleck, *The Theory of Electric and Magnetic Susceptibilities*, Clarendon Press, Oxford, 1932, p.248.

20. L. M. Holmes, R. Sherwood, and L.G. Van Uitert, *Phys. Rev*. **178**, 576 (1969).

21. T. Kasuya, *IBM J. Res. Dev*. **14**, 214 (1970).

22. J. E. Greedan and G. J. McCarthy, *Mat. Res. Bull*. **7**, 531 (1972).

23. J. E. Greedan, C. L. Chien, and R. G. Johnston, *J. Solid State Chem.* **19**, 155 (1976).

24. D. C. Cook and J. D. Cashion, *J. Phys., C: Solid St. Phys*. **13**, 4199 (1980).

25. J. A. Mydosh, *Spin Glasses: An Experimental Introduction* (Taylor & Francis, London, 1993).

Chapter 4 Magnetodielectric coupling in bulk polycrystalline $EuZrO_3$

4.1 Introduction

The coupling between electric dipoles and localized spins, by which the electrical (magnetic) property can be controlled by magnetic (electric) field, has attracted a lot of attention in the viewpoint of fundamental research and industrial applications [1-8]. Previous studies have focused on multiferroics where spontaneous polarization exists and linear magnetoelectrics where polarization can be induced by an applied magnetic field due to the presence of certain symmetry [1-4]. Recently, a new term magnetodielctrics has been introduced to classify magnetic materials which neither possess spontaneous polarization nor satisfy the symmetry constraints for the linear magnetoelectric effect, but nevertheless show a coupling between dielectric properties and magnetization [5-8]. Such materials usually depict a change in dielectric constant at the magnetic transition temperature or show finite magnetocapacitance.

A typical example of magnetodielectrics is $EuTiO_3$ [5]. As shown in Fig. 1.4 (c), the dielectric constant of $EuTiO_3$ follows the feature of normal quantum paraelectric above T_N and exhibits a sharp decrease below T_N. The dielectric property of $EuTiO_3$ is suggested to be associated with a soft phonon mode which tends to zero frequency when the temperature approaches zero. As a result, the energy scale of the dielectric constant is comparable to that of a magnetic interaction or magnetic field, which leads to a strong magnetodielectric coupling in $EuTiO_3$. Goian *et al.* proposed that similar to those in $SrTiO_3$, $PbTiO_3$, and $BaTiO_3$, the soft phonon mode in $EuTiO_3$ is Slater-type mode [9]. Since the Slater-type mode is largely dependent on the covalency of the B-O

bonds in the ABO_3-type perovskite [10], the magnetodielectric effect in $EuTiO_3$ can be understood in terms of the impact of the magnetic exchange interaction between Eu^{2+} ions on the electron density involved in the Ti-O bonding. One way to examine this hypothesis is to search for another $Eu^{2+}B^{4+}O_3$-type perovskite with similar magnetic property but different degree of covalency of the B-O bond. The above study has demonstrated that $EuZrO_3$ has very similar crystalline and magnetic structures to those of $EuTiO_3$. On the other hand, one may expect the valence electronic structure of these two perovskites to be quite different. Namely, in contrast to partially covalent Ti-O bond in $EuTiO_3$, the Zr-O bond in $EuZrO_3$ is more ionic, similar to the case of $SrZrO_3$. This makes $EuZrO_3$ an important reference material for understanding of the magnetodielectric effect in Eu^{2+}-based perovskites.

In this study, dielectric measurements have been performed in $EuZrO_3$ as a function of temperature and magnetic field. The dielectric constant gradually decreases upon cooling without any quantum paraelectric behavior; however, below T_N it exhibits a pronounced drop that qualitatively resembles that observed in $EuTiO_3$. The magnitude of the magnetodielectric effect in $EuZrO_3$ has been evaluated and discussed in comparison with that of $EuTiO_3$.

4.2 Experimental

The sample used for dielectric measurements was $EuZrO_3$ ceramic with 98 % density prepared from single phase $EuZrO_3$ powder by spark plasma sintering, SPS (Dr. Sinter, SPS-1050, Japan), at 1450 ℃ under 130 MPa uniaxial pressure and base vacuum pressure of 2×10^{-2} Pa [11]. The $EuZrO_3$ powder was prepared from Eu_2O_3 and ZrO_2 (both 99.9% pure) at 1300 ℃ for 20 h in pure hydrogen under a flow rate of 80 cm^3/min.

To release the residual lattice strain after SPS, the $EuZrO_3$ ceramics were annealed at 1300 ℃ in H_2 gas for 20 h. For dielectric measurements Au electrodes were spattered on the discs of 7 mm diameter and 1 mm thickness. Dielectric properties were measured with Agilent E4980 Precision LCR Meter in the temperature interval of 2.5-300 K and magnetic field of 0-8 T utilizing a home-made dielectric measurements probe with the Physical Property Measurement System (Quantum Design PPMS).

4.3 Results and discussion

Figures 4.1(a) and (b) show the dielectric constant (ε') and the loss tangent ($\tan\delta$) of $EuZrO_3$ as a function of temperature, respectively. The value of ε' is weakly temperature dependent with $d\varepsilon'/dT = 6.8\times10^{-3}$ K^{-1}. From 300 K to 5 K, ε' gradually decreases from 30.1 to 28.45 with no indication of the quantum paraelectric behavior. This is very similar to that in $SrZrO_3$ [12] and can be attributed to the predominantly ionic Zr-O bond which does not favor formation of the soft phonon mode. Above 175 K, ε' shows low-frequency dispersion which, we believe, arises from the finite electronic conductivity also evidenced from the large $\tan\delta$ values (Fig. 4.1(b)). The value of $\tan\delta$ exhibits a linear relationship with the inverse angular frequency (ω) (not shown). According to

$$\varepsilon^* = \varepsilon' + i\frac{\sigma'}{\varepsilon_0\omega}, \tag{4.1}$$

where ε_0 is the vacuum constant, we conclude that above 175 K the imaginary part of the dielectric constant is dominated by the electronic conductivity.

The low-temperature dielectric behavior of $EuZrO_3$ is shown in Fig. 4.2(a) as a function of applied magnetic field. The curve measured at $H = 0$ demonstrates an

anomalous drop below about 4 K, which is the temperature corresponding to the antiferromagnetic transition. With increasing magnetic field, ε' at low temperatures gradually increases and finally the cusp disappears. This behavior resembles that of magnetization, where the cusp disappears due to the ferromagnetic arrangement of the spins under a high magnetic field (Fig. 4.2(b)). The magnetic field dependent $\varepsilon'(H)/\varepsilon'(0)$ is shown in the inset of Fig. 4.2(a). The change of ε' is about 0.2% at 4 T, which is much smaller than that in $EuTiO_3$ [5].

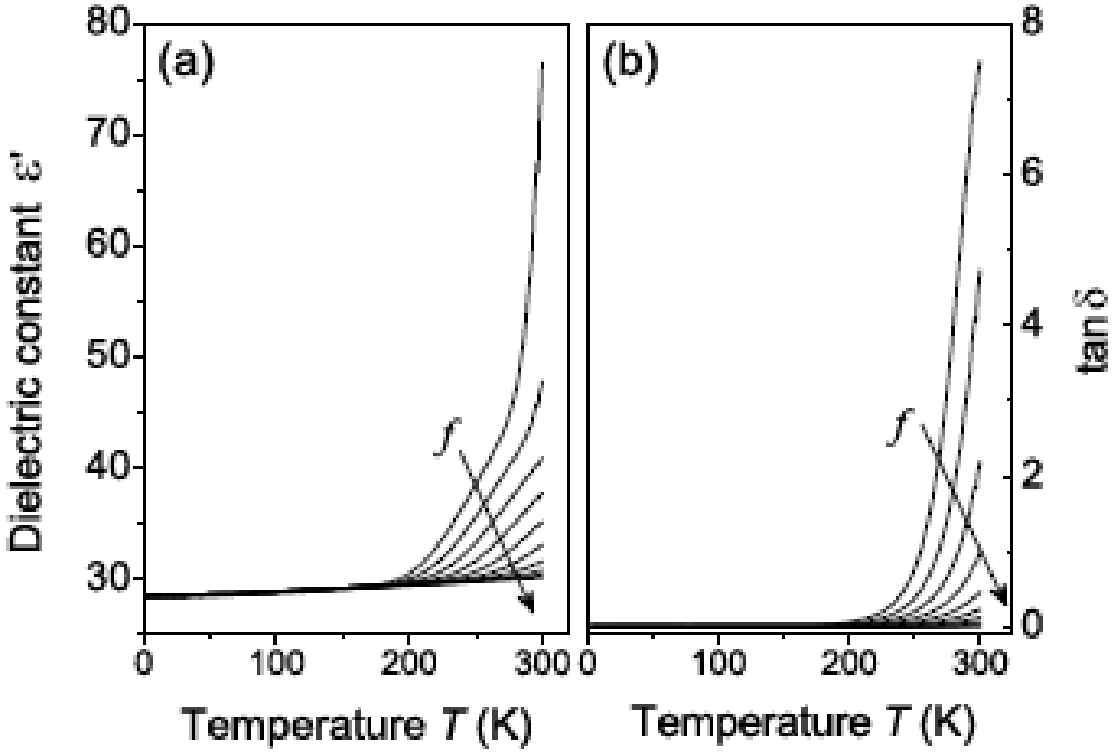

Fig. 4.1: Temperature dependence of (a) dielectric constant, ε', and (b) dielectric loss, $\tan\delta$, of $EuZrO_3$ at selected frequencies f = 0.1, 0.3, 0.7, 1.7, 4.4, 11.3, 29.2, 75.3, 194, and 500 kHz (from top to end).

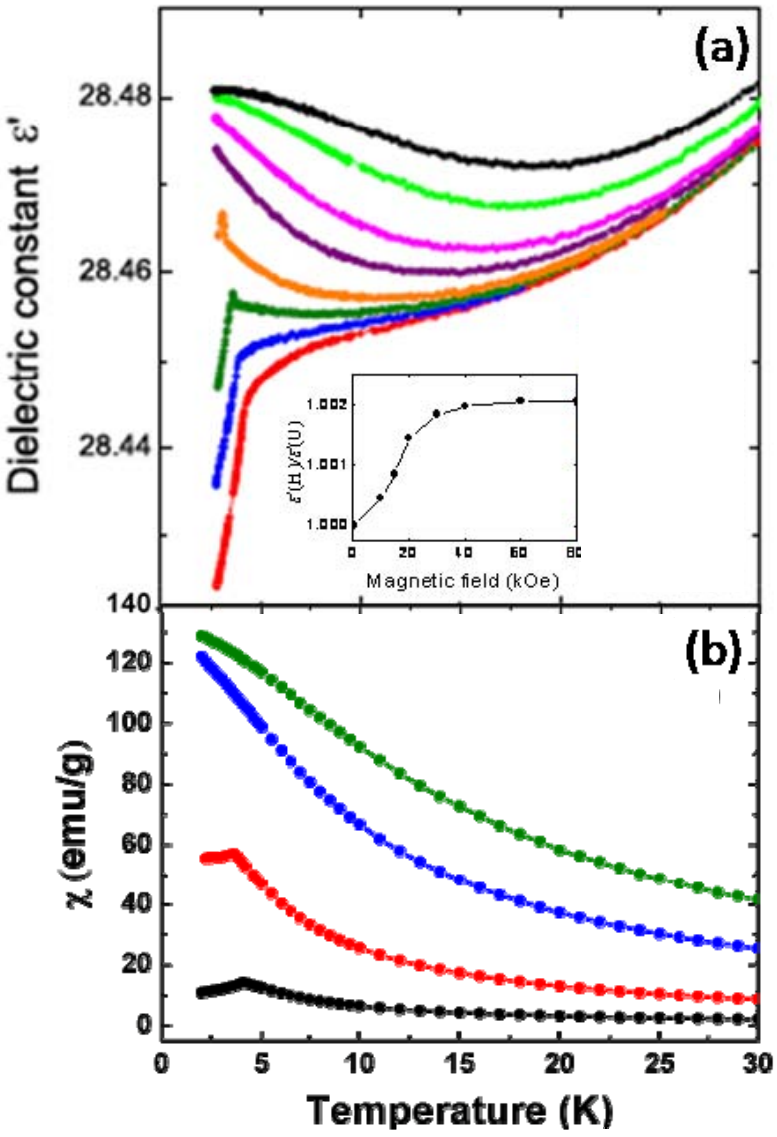

Fig. 4.2: (a) Dielectric constant at 200 kHz measured in magnetic fields of 0, 10, 15, 20, 30, 40, 60, 80 kOe (from up to down). The inset shows the magnetic field dependence of the dielectric constant (normalized to the value at zero field) at 2.5 K. (b) Magnetization measured in magnetic fields of 0.05, 10, 30, 50 kOe (from up to down).

To investigate the influence of magnetic interaction on the dielectric properties, we have performed a mean-field calculation of the spin system with S = 7/2 [5,13]. Assuming that the spins on Eu^{2+} in $EuZrO_3$ locate on a cubic lattice with a G-type antiferromagnetic ordering, under mean-field approximation the Hamiltonian can be written as

$$H = -\sum_{<i,j>} J_1 S_i \cdot S_j - \sum_{[i,j]} J_2 S_i \cdot S_j - \sum_i h \cdot S_i \,, \tag{4.2}$$

where S_i is the Heisenberg spin at Eu site i, and h is the external magnetic field parallel to the z axis. The exchange constants J_1 and J_2 equal to -0.032/k K and 0.017/k K, respectively, as evaluated in Chapter 3. <i,j> and [i,j] denote the summation over the NN and NNN neighbors, respectively. The G-type magnetic structure can be divided into two equivalent sublattices a and b. Thus,

$$H = H_a + H_b = 2H_a, \tag{4.3}$$

where H_a and H_b are the Hamiltonians belonging to a and b sublattices, respectively. In the mean-field approximation H_a can be calculated by

$$H_a = H_a^x \sum_{ai} S_{ai}^x + H_a^z \sum_{ai} S_{ai}^z \,, \tag{4.5}$$

where

$$H_a^x = -6J_1 \left\langle S_a^x \right\rangle - 12J_2 \left\langle S_a^x \right\rangle, \tag{4.6}$$

$$H_a^z = -h - 6J_1 \left\langle S_a^z \right\rangle - 12J_2 \left\langle S_a^z \right\rangle. \tag{4.7}$$

Here x and z denote the spin components. The thermoaverage of the spin components on the sublattice can be obtained as

$$\left\langle S_a^z \right\rangle = \frac{-H_a^z}{2\sqrt{(H_a^x)^2 + (H_a^z)^2}} \times \frac{\sum_{i=1}^{4} (2i-1) \sinh(\frac{(2i-1)}{2k_B T}) \sqrt{(H_a^x)^2 + (H_a^z)^2}}{\sum_{i=1}^{4} \cosh(\frac{(2i-1)}{2k_B T}) \sqrt{(H_a^x)^2 + (H_a^z)^2}} \,, \tag{4.8}$$

$$\left\langle S_a^x \right\rangle = \frac{H_a^x}{H_a^z}\left\langle S_a^z \right\rangle . \tag{4.9}$$

The spin correlation between nearest neighbors can be approximately evaluated by

$$\left\langle S_i \cdot S_j \right\rangle = \left\langle S_a^x \right\rangle^2 + \left\langle S_a^z \right\rangle^2 , \tag{4.10}$$

and the z component of the total spin moment can be expressed by

$$\left\langle S_z \right\rangle = 2\left\langle S_a^z \right\rangle . \tag{4.11}$$

The calculated values of $<S_i \cdot S_j>$ and $<S_z>$ at different temperatures under several magnetic fields are shown in Fig. 4.3(a) and (b), respectively. The behaviors of $<S_i \cdot S_j>$ and $<S_z>$ are very similar to those of ε' and magnetization, respectively, which gives a direct evidence for the magnetodielectric coupling. By fitting the experimental data of ε' to the following formula

$$\varepsilon'(H) = \varepsilon'(H = 0)(1 + \alpha\left\langle S_i \cdot S_j \right\rangle), \tag{4.12}$$

where ε' (H = 0) is dielectric constant at zero magnetic field, and α is the coupling constant between spin correlation and dielectric constants, the value of α was obtained to be 1.1×10^{-4}. This value is a factor of 27 lower than that of $EuTiO_3$ (i.e., 2.74×10^{-3} [5]), suggesting a much weaker magnetodielectric coupling in $EuZrO_3$ compared to that in $EuTiO_3$. In accord with the hypothesis of Goian *et al.* [9], this difference can be attributed to stronger covalency of the Ti-O bond in $EuTiO_3$ which favors formation of the soft phonon mode which, in turn, facilitates coupling with low-energy magnetic excitations.

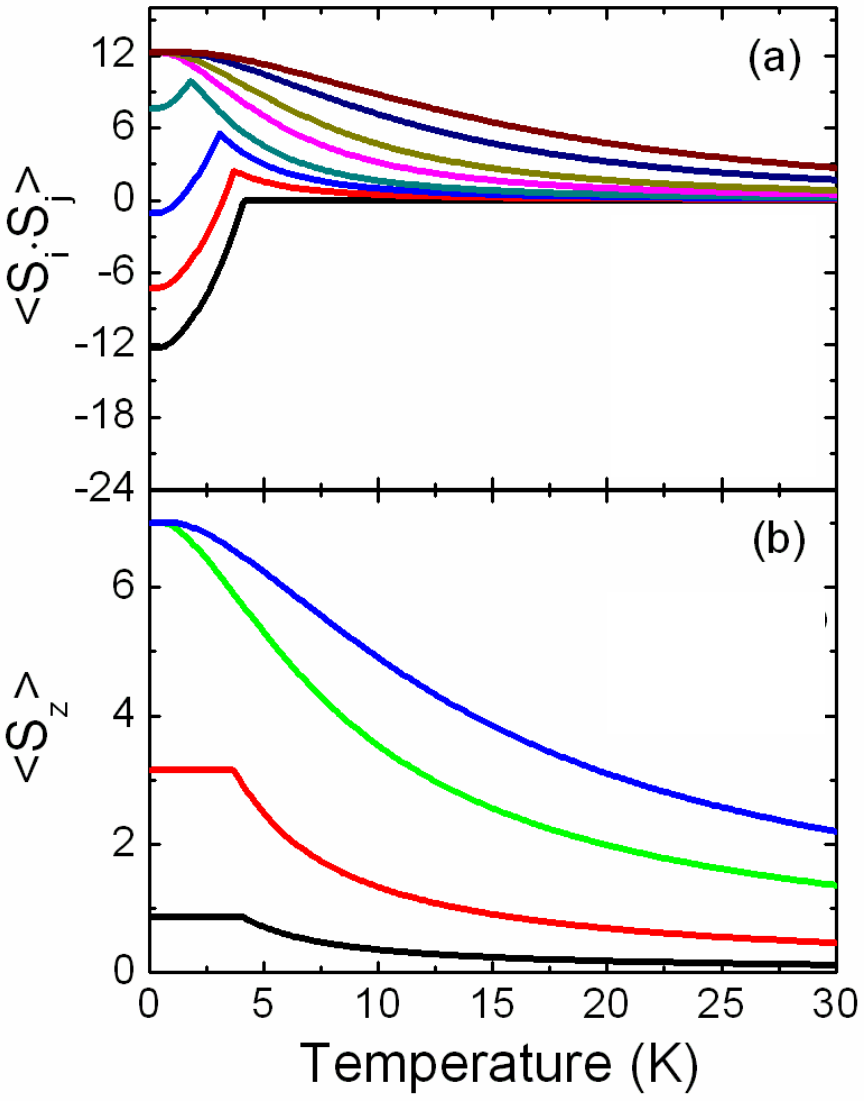

Fig. 4.3: (a) Spin pair correlation between nearest-neighbor sites $<S_i \cdot S_j>$ under magnetic fields of 0, 10, 15, 20, 30, 40, 60, 80 kOe (from up to down) and (b) the z component (parallel to the magnetic field) of the total magnetization $<S_z>$ measured under magnetic fields of 0.05, 10, 30, 50 kOe (from up to down) calculated under a mean-field approximation by assuming that the spins on Eu^{2+} in $EuZrO_3$ locate on a cubic lattice.

4.4 Conclusions

The dielectric properties of bulk polycrystalline $EuZrO_3$ have been measured and the magnetodielectric effect was examined based on a mean-field calculation of the spin system. At low temperatures $EuZrO_3$ shows a magnetodielectric effect qualitatively similar to that in $EuTiO_3$ but has no quantum paraelectric behavior. The magnitude of the magnetodielectric coupling in $EuZrO_3$ is much smaller than that in $EuTiO_3$, which can be understood by the difference in the covalency between the Zr-O and Ti-O bonds.

References

1. Z. J. Huang, Y. Cao, Y. Y. Sun, Y. Y. Xue, and C. W. Chu, *Phys. Rev. B* **56**, 2623 (1997).
2. N. Hill, *J. Phys. Chem. B* **104**, 6694 (2000).
3. T. Kimura, Y. Sekio, H. Nakamura, T. Siegrist, and A. P. Ramirez, *Nat. Mater.* **7**, 291 (2008).
4. T. Goto, T. Kimura, G. Lawes, A. P. Ramirez, and Y. Tokura, *Phys. Rev. Lett.* **92**, 257201 (2004).
5. T. Katsufuji and H. Takagi, *Phys. Rev.B* **64**, 054415 (2001).
6. R. Muralidharan, T. -H. Jang, C. -H. Yang, Y. H. Jeong, and T. Y. Koo, *Appl. Phys. Lett.* **90**, 012506 (2007).
7. M. S. Seehra and R. E. Helmick, *Phys. Rev. B* **24**, 5068 (1981).
8. G. Lawes, A. P. Ramirez, C. M. Varma, and M. A. Subramanian, *Phys. Rev. Lett.* **91**, 257208 (2003).
9. V. Goian, S. Kamba, J. Hlinka, P. Van¸ek, A. A. Belik, T. Kolodiazhnyi, and J. Petzelt, *Eur. Phys. J. B* **71**, 429 (2009).
10. R. E. Cohen, *Nature* **358**, 136 (1992).
11. S. Grasso, Y. Sakka, and G. Maizza, *Sci. Technol. Adv. Mater.* **10**, 053001 (2009).
12. D. Souptel, G. Behr, and A. M. Balbashov, *J. Cryst. Growth* **236**, 583 (2002).
13. H. Wu, Q. Jiang, and W. Z. Shen, *Phys. Rev. B* **69**, 014104 (2004).

Summary

In this thesis, for the purpose of gaining deep insight into mechanism of magnetic interactions and phase transition in Eu^{2+}-containing compounds and developing new types of spintronic devices, amorphous europium titanate and europium zirconate thin films as well as bulk polycrystalline $EuZrO_3$ have been fabricated and their structural, magnetic and dielectric properties have been investigated. The magnetic properties of the amorphous thin films were understood in terms of the local structures of Eu^{2+} ions as examined by ^{151}Eu CEM and EXAFS spectra. The structure of $EuZrO_3$ was refined by Rietveld analysis and its magnetic and dielectric properties were examined and compared with those of $EuTiO_3$. The results are summarized as follows.

In chapter 1, the theoretical background of magnetism for Eu^{2+}-containing compounds was described and the progress in related studies was reviewed. Since the 4*f* electrons on Eu^{2+} ions are shielded by 5*s* and 5*p* closed shells, the mechanisms of magnetic exchange interactions between Eu^{2+} ions are different from the interactions between transition-metal ions, which have been widely studied. The mechanisms proposed previously were overviewed and their applicability and limitations were discussed. The research status of Eu^{2+}-containing compounds was reviewed with a focus on magnetic properties of EuX (X is O, S, Se, and Te) and $EuTiO_3$.

In chapter 2, amorphous europium titanate thin films with nominal compositions of *m*EuO-TiO_2 (*m*=1, 2, 4) were prepared by the PLD method and their structural and magnetic properties were investigated. The amorphous nature of the thin films was confirmed by XRD pattern, HRTEM image, and SAED pattern. The valence state of Eu in the thin films was examined by ^{151}Eu CEM spectra. The analyses of CEM and

EXAFS spectra indicate that the local structures of Eu^{2+} ions in amorphous EuO-TiO_2 and 2EuO-TiO_2 thin films are similar to that in EuO, and the coordination number of Eu^{2+} and Eu-O bond length decrease with the increase of *m* in *m*EuO-TiO_2 (*m*=1, 2, 4). All the thin films show positive Weiss temperatures and undergo a reentrant spin glass transition after a ferromagnetic transition as the temperature is decreased. The mechanism of magnetic phase transition was discussed in terms of their structures.

In chapter 3, bulk polycrystalline $EuZrO_3$ and amorphous europium zirconate thin films with nominal compositions of *m*EuO-ZrO_2 (*m*=1, 4) were prepared and their structural and magnetic properties were investigated. In section 3.1, bulk polycrystalline $EuZrO_3$ was prepared by a high-temperature solid-state reaction method. The crystal structure of $EuZrO_3$ was refined to be an orthorhombic perovskite by Rietveld analysis of XRD pattern, consistent with one of the previous reports. An antiferromagnetic transition was observed in $EuZrO_3$ with a positive Weiss temperature of 0.07 K. The magnetic structure of $EuZrO_3$ was discussed with regard to a *G*-type antiferromagnetic structure. In section 3.2, amorphous europium zirconate thin films were fabricated by the PLD method and the valence state of Eu in the thin films was examined by ^{151}Eu CEM spectra. Similarly to amorphous europium titanate thin films, amorphous europium zirconate thin films exhibit ferromagnetic and reentrant spin glass transitions with positive Weiss temperatures. Furthermore, as confirmed by these results, the fact that ferromagnetic interactions are dominant is intrinsic to Eu^{2+}-containing oxides with high Eu^{2+} concentration.

In chapter 4, the dielectric properties of bulk polycrystalline $EuZrO_3$ were measured and the magnetodielectric effect was examined based on the calculation of spin correlation under the mean-field approximation. $EuZrO_3$ does not show quantum

paraelectric behavior but a magnetodielectric coupling at low temperatures. The magnitude of the coupling constant in $EuZrO_3$ was evaluated to be a factor of 27 lower than that in $EuTiO_3$, which can be understood by the difference in the covalency between Zr-O and Ti-O bonds.

List of publications

Chapter 1

"High-quality antiferromagnetic $EuTiO_3$ epitaxial thin films on $SrTiO_3$ prepared by pulsed laser deposition and postannealing"

Koji Fujita, Naoki Wakasugi, Shunsuke Murai, Yanhua Zong, and Katsuhisa Tanaka

Appl. Phys. Lett. **94**, 062512 (2009).

Chapter 2

"Preparation and magnetic properties of amorphous $EuTiO_3$ thin films"

Yanhua Zong, Koji Fujita, Hirofumi Akamatsu, Shunsuke Murai, and Katsuhisa Tanaka

J. Non-Cryst. Solids in press (2010).

"Impact of amorphization on the magnetic properties of EuO-TiO_2 system"

Hirofumi Akamatsu, Koji Fujita, Yanhua Zong, Naohiro Takemoto, Shunsuke Murai, and Katsuhisa Tanaka

Phys. Rev. B submitted (2010).

"XAFS studies of the structure of Eu^{2+}-containing amorphous thin films"

Yanhua Zong, Koji Fujita, Hirofumi Akamatsu, Shunsuke Murai, and Katsuhisa Tanaka

J. Non-Cryst. Solids submitted (2010).

Chapter 3

"Antiferromagnetism of perovskite $EuZrO_3$"

Yanhua Zong, Koji Fujita, Hirofumi Akamatsu, Shunsuke Murai, and Katsuhisa Tanaka

J. Solid State Chem. **183**, 168 (2010).

"Ferromagnetic properties of amorphous $EuZrO_3$ thin films"

Yanhua Zong, Koji Fujita, Hirofumi Akamatsu, Shunsuke Murai, and Katsuhisa Tanaka

Phys. Stat. Sol. (c) in press (2010).

Chapter 4

"Magnetodielectric effect in $EuZrO_3$"

T. Kolodiazhnyi, K. Fujita, L. Wang, Y. Zong, K. Tanaka, Y. Sakka, and E. Takayama-Muromachi

Appl. Phys. Lett. **96**, 252901 (2010).

Acknowledgement

The present thesis has been conducted under the supervision of Professor Katsuhisa Tanaka at Graduate School of Engineering, Kyoto University.

My deepest gratitude goes first and foremost to Professor Katsuhisa Tanaka for his constant encouragement and guidance. Without his consistent instructions, this thesis could not reach the present form. I sincerely appreciate Professor Kazuyuki Hirao and Professor Toshinobu Yoko for kindly reading this thesis and giving many suggestions. I would like to express my heartfelt gratitude to Professor Koji Fujita who has walked me through every stage of designing the experiments and writing this thesis. I am also greatly indebted to Professor Shunsuke Murai for tremendous help during the past three years.

A special thank would go to Dr. Hirafumi Akamatsu who has led me to the present work and instructed me a lot in the operation of experimental equipments and writing academic articles. I owe my sincere gratitude to all the members in Tanaka laboratory espetially the members in magnetic group, Dr. Hideaki Murase, Mr. Tomohiko Matoba, Mr. Hideo Murakami, Mr. Naohito Imada, Mr. Naoki Wakasugi, Mr. Yuya Maruyama, and Mr. Yoshio Kususe, for their help in life and study. I would also like to express my heartfelt gratitude to my friends for helping me in life and working me out difficulties.

I sincerely appreciate Japanese government for financial support (MEXT scholarship No. 073331) during my doctoral course.

Last my thanks would go to my beloved family for their loving considerations and great confidence in me all through these years.

Kyoto University, 2010 Yanhua Zong